



## City Research Online

### City, University of London Institutional Repository

---

**Citation:** Lyras, T. (2024). Large Eddy Simulation of Flash Induced Spray Atomization. (Unpublished Doctoral thesis, City, University of London)

This is the accepted version of the paper.

This version of the publication may differ from the final published version.

---

**Permanent repository link:** <https://openaccess.city.ac.uk/id/eprint/33911/>

**Link to published version:**

**Copyright:** City Research Online aims to make research outputs of City, University of London available to a wider audience. Copyright and Moral Rights remain with the author(s) and/or copyright holders. URLs from City Research Online may be freely distributed and linked to.

**Reuse:** Copies of full items can be used for personal research or study, educational, or not-for-profit purposes without prior permission or charge. Provided that the authors, title and full bibliographic details are credited, a hyperlink and/or URL is given for the original metadata page and the content is not changed in any way.

# Large Eddy Simulation of Flash Induced Spray Atomization

Theodoros Lyras

*Primary Supervisor:* Prof. Manolis Gavaises

*Secondary Supervisor:* Dr. Yiannis Karathanassis



SCHOOL OF SCIENCE AND TECHNOLOGY  
DEPARTMENT OF ENGINEERING  
CITY, UNIVERSITY OF LONDON

Thesis submitted for the fulfilment of the requirements  
for the degree of *Doctor of Philosophy*

January 2024



*To my family. Without them,  
nothing could be as easy.*



## Declaration

I hereby declare that this thesis is the product of my work and it has been written by me in its entirety. All sources of information or contributions by other authors that have been used in this thesis have been duly acknowledged within the text and the references.

I confirm that the content of this thesis has not been submitted in whole or in part for consideration for any other degree or qualification in this, or any other university.

---

Theodoros Lyras  
January 2024



## Acknowledgments

This effort would not be possible without the guidance, support and understanding of Prof. Manolis Gavaises, whom I would like to thank wholeheartedly. The same goes for Dr. Yiannis Karathanassis. His insight, help and patience were truly invaluable all those years of cooperation and I am very grateful for all his support. I would also like to thank Dr. Phoevos Koukouviniis for his tremendous aid in this endeavour, and Dr. Andreas Papoutsakis and Amalia Petrova for the excellent collaboration over various aspects of my project.

For his huge support on British ground, I thank Mr. Nikolaos Chatziarsenis. I also thank Nikos Kyriazis for the great academic cooperation and along with him I thank Akis, Alvaro, Armand, Carlos, Georgia, Hesam, Homa, Kostas, Max, Milad, Mithun, Saeed, Vangelis and Yves, the amazing people in A306 that I consider friends. Finally, many thanks go to my cousin Efi.

On the Greek side, I would like to thank Dionysis and Stavros as well as Dr. Nikolopoulos for their hospitality during my secondment in CERTH. I also feel that I should thank Prof. Kyriakos Giannakoglou for creating a spark that eventually led me to pursue a PhD degree.

Of course, things feel better and more meaningful if you have people to share them with. That is why I want to express my gratitude for the support of my friends, old and new. A special thanks is dedicated to Alexandra for her understanding and, finally, I deeply thank my parents and my brother Christos, to whom this thesis is dedicated.

Finally, I would like to acknowledge the financial support that I received in the form of a PhD studentship from the European Union Horizon 2020 Research and Innovation programme, within the framework of the "HAoS" project.



# Abstract

Flashing boiling is a phase-changing process that takes place under abrupt pressure decrease and manifests when a liquid reaches a superheated state. As a phenomenon, flash boiling is present in many industrial and technical applications. Flashing can be observed in the case of nozzle, orifice and valve flows, in cooling applications of cryogenic fluids, in internal combustion engines for fuel spray atomisation purposes or upon failure and rupture of pressurised vessels or pipes that contain liquefied gases.

The present work focuses on flash boiling in aerospace and automotive applications. To study the phenomenon two different numerical approaches have been implemented. First, a compressible, transient, explicit, density-based solver, on which tabulated thermodynamic properties have been implemented, was developed within the OpenFOAM framework and has been executed for URANS simulations. Secondly, a compressible, transient, implicit, coupled, pressure-based solver, was used within the framework of ANSYS Fluent software. A mass transfer model has been developed and tested with said pressure-based solver using URANS, DES and LES turbulence modelling.

A wide range of experimental conditions that are of relevance to space applications has been investigated to study flash boiling using cryogenic liquids, namely liquid oxygen and nitrogen, and traditional fuels like iso-octane as the operating fluids. The numerical results highlight that flash boiling is a process of high uncertainty due to its inherent features, namely metastability effects and transient phenomena that may occur upon its development. Although an assumption of thermal equilibrium can not always be valid, in the case of injection under steady conditions, the results can be sufficiently accurate. The methodology presented in this work can be applied without any calibration for any range of conditions that have been tabulated, regardless of the boundary conditions or the involved geometry. Although flash boiling in aerospace and automotive applications has been the focus of this work, the proposed methods can be applied to a broad spectrum of engineering problems, ranging from gasoline direct injection (GDI) and aerospace engine optimisation to industrial cooling and nuclear safety.



## Project's Contribution

**Real fluid thermodynamic properties:** The employed methodology utilizes the Helmholtz Energy equation of state, which is applied in an extended range of conditions, to represent the properties of cryogenic fluids. The use of Helmholtz Energy EOS in the framework of cryogenic flashing has not been documented.

**Range of applicability:** The applicability of the presented methodology in an extended range of conditions without the need for adjustments or calibration is demonstrated in this work. Due to the consistent numerical flux and the tabulated properties from a high-accuracy EOS, the methodology has been applied for pressure conditions that range from supercritical down to near-vacuum.

**Phase-change model evaluation:** As part of the present work, a bubble-dynamics-based phase change model was developed implemented and evaluated for cryogenic flashing numerical investigations. The evaluation of such model in the context of cryogenic flash boiling is not documented and the results of this research produce significant insight in the field.



# Contents

<b>List of Figures</b>	xvi
<b>List of Tables</b>	xxi
<b>1 Introduction</b>	<b>1</b>
1.1 Background and motivation	1
1.2 Objectives	3
1.3 Outline	4
<b>2 Literature review</b>	<b>5</b>
2.1 Overview	5
2.2 Nucleation	5
2.3 Bubble growth	7
2.4 Flash boiling atomization	11
2.5 Cryogenic flows and experimental data	12
2.6 Numerical modelling of flashing flows	14
2.6.1 Homogeneous equilibrium models	15
2.6.2 Non-homogeneous equilibrium models	17
2.6.3 Homogeneous non-equilibrium models	18
2.6.4 Non-homogeneous non-equilibrium models	19
<b>3 Numerical methodology</b>	<b>21</b>
3.1 Conservation equations	22
3.1.1 Unsteady Reynolds-averaged Navier-Stokes	23
3.1.2 Large eddy simulation	25
3.1.3 Detached eddy simulation	25
3.2 Pressure and density based solvers	25
3.3 Equations of state	28
3.3.1 Helmholtz energy equation of state	29
3.3.2 Thermodynamic data tabulation	30
3.4 Mass transfer models	31
3.5 Examined cases, boundary conditions and fluid properties	32

---

<b>4</b>	<b>Modelling of liquid oxygen nozzle flows under subcritical and supercritical pressure conditions</b>	<b>35</b>
4.1	Introduction	36
4.2	Methodology	40
4.2.1	Thermal non-equilibrium assumption	40
4.2.2	Thermal equilibrium assumption	41
4.2.3	Turbulence closure	43
4.2.4	Domain discretisation and grid independence	44
4.2.5	Boundary and initial conditions	47
4.3	Results	48
4.3.1	Code validation	49
4.3.2	Simulations in the subcritical regime	52
4.3.3	Simulations in the supercritical regime	59
4.3.4	Comparison of expansion dynamics for the two regimes	61
4.3.5	Flow instabilities	63
4.4	Concluding remarks	67
<b>5</b>	<b>Modelling of liquid oxygen and nitrogen injection under flashing conditions</b>	<b>69</b>
5.1	Introduction	70
5.2	Methodology	74
5.2.1	Mass-transfer model	76
5.2.2	Helmholtz energy equation of state	77
5.2.3	Turbulence closure	79
5.2.4	Domain discretisation	79
5.2.5	Boundary and initial conditions	81
5.2.6	Validation and grid independence	82
5.3	Results	84
5.3.1	Liquid Oxygen flashing flow	85
5.3.2	Liquid Nitrogen flashing flow	90
5.4	Concluding remarks	97
<b>6</b>	<b>Large eddy simulation of iso-Octane under flashing injection conditions</b>	<b>99</b>
6.1	Introduction	99
6.2	Methodology	103
6.2.1	Turbulence closure	103

6.2.2	Injector geometry, boundary conditions and initialisation	104
6.3	Results	108
6.4	Concluding remarks	114
<b>7</b>	<b>Conclusions</b>	<b>115</b>
<b>A</b>	<b>Developed solvers and functions, and implementation process</b>	<b>117</b>
	<b>List of Publications</b>	<b>127</b>
	<b>Bibliography</b>	<b>128</b>

# List of Figures

2.1	Schematics of pressure-volume isotherms for a pure fluid.	6
2.2	Comparison of different models for predicting bubble growth in superheated water (based on [1]).	10
2.3	Variation of the Sauter mean diameter (SMD) with (a) superheat degree (adapted from [2]) and (b) superheat ratio (adapted from [3]).	12
2.4	Representation of a growing vapour bubble within the liquid environment under thermodynamic (a) equilibrium and (b) non-equilibrium (based on [4].)	15
2.5	Classification of available approaches for modelling flashing flows depending on the assumptions on thermal and mechanical equilibrium.	16
3.1	Overview of the models, equations of state and other approaches that have been incorporated into the pressure- and the density-based solver, which have been used for the production of the results of this work.	34
4.1	Three-dimensional phase diagrams for oxygen: (a) pressure, (b) speed of sound and (c) internal energy in terms of density and temperature.	42
4.2	Geometry of the conical converging-diverging nozzle [5]. The inflow has been expanded upstream in order to impose the stagnation conditions of the experiment.	44
4.3	Grid independence study for URANS simulations: (a) pressure and (b) vapour volume fraction distributions at the orifice symmetry axis for grids of increasing cell count.	45
4.4	Computational grid employed for (a) URANS simulations and (b) DES. Detailed views of the nozzle inlet, as well as the nozzle throat region, are presented as insets for both grids.	46
4.5	Validation of the density-based solver (OF) for the converging-diverging nozzle case: Numerical results for (a) pressure, (b) velocity magnitude, (c) Mach number (d) vapour volume-fraction distributions along the orifice symmetry line and comparison against the predictions of the 1-D solver (HLLC).	51

- 
- 4.6 Validation of the pressure-based solver using NIST-REFPROP database: Comparison of numerical predictions of the average N<sub>2</sub>-jet density distribution at the jet axis (solid line) against experimental data (symbols) [6]. The average density contour plot is depicted in the inset. 52
- 4.7 Contour plots of the (a) pressure, (b) velocity (c) gaseous volume fraction and (d) temperature field in the nozzle-throat region for case 1 of Table 4.2. It is noted that different variable ranges have been used in frame (d) to enhance clarity. Upper frames depict predictions produced using the Hertz-Knudsen ( $\lambda=0.7$ ) phase-change model (Equation 4.2), while lower frames those produced using the Helmholtz EOS (Equation 4.3). All contours represent the part of the nozzle from  $X=-0.045$  m to  $X=0.08$  m. 53
- 4.8 Distribution of (a) Pressure, (b) velocity, (c) vapour-volume fraction and (d) temperature at the orifice symmetry axis, as predicted by the two numerical approaches for case 1 of Table 4.2. 55
- 4.9 Contour plots of the (a) pressure, (b) velocity (c) vapour-volume fraction and (d) temperature fields in the nozzle throat region for case 2 of Table 4.2. It is noted that different variable ranges have been used in frame (d) to enhance clarity. The upper and lower panels depict predictions produced using the Hertz-Knudsen phase-change model (Equation 4.2) and the HEM/Helmholtz EOS (Equation 4.3), respectively. All contours represent the part of the nozzle from  $X=-0.045$  m to  $X=0.08$  m. 57
- 4.10 Distribution of (a) pressure, (b) velocity, (c) vapour volume fraction and (d) temperature at the orifice symmetry axis, as predicted by the two thermodynamic approaches for case 2 of Table 4.2. 58
- 4.11 Contour plots of the (a) pressure, (b) velocity, (c) density and (d) temperature field for supercritical injection (case 3 of Table 4.2). The upper frames of each figure depict the predictions produced using the pressure-based solver and the NIST database, while the lower frames, those produced using a density-based solver and tabulated data produced by solving the Helmholtz EOS. All contours represent the part of the nozzle from  $X=-0.045$  m to  $X=0.08$  m 60
- 4.12 Distribution of (a) pressure, (b) velocity, (c) density and (d) temperature at the orifice symmetry axis, as predicted by the two solvers adopting different thermodynamic approaches for case 3 of Table 4.2. 61

- 
- 4.13 Contour plot of the Mach number in the throat and downstream regions (thermal non-equilibrium model). (a) Case 1 of Table 4.2:  $p_{in}/p_{out} = 11.4 \text{ bar}/2.6 \text{ bar}$ , (b) case 2 of Table 4.2:  $p_{in}/p_{out} = 43.0 \text{ bar}/10.0 \text{ bar}$ , and (c) Case 3 of Table 4.2:  $p_{in}/p_{out} = 133.0 \text{ bar}/124.2 \text{ bar}$ . 62
- 4.14 Cross-flow velocity profiles for (a) subcritical case 2 ( $U_{x,max} = 86.6 \text{ m/s}$ ) and (b) supercritical case 3 ( $U_{x,max} = 111.4 \text{ m/s}$ ) of Table 4.2. 63
- 4.15 Contour plots of time-averaged field over the nozzle plane of symmetry. Results were produced using a detached eddy simulation (DES) approach. Upper frames correspond to case 1 and lower ones to case 2 of Table 4.2: (a) pressure (b) axial velocity and (c) vapour-volume fraction. The figures include the part of the nozzle from  $X=-23.5 \text{ mm}$  to  $X=98.2 \text{ mm}$ . 64
- 4.16 Velocity vectors over axial velocity contour plots in a detailed view after the nozzle throat exit ( $X=0.015 \text{ m}$ ) corresponding to characteristic time instances of DES: (a)  $t = 0.240 \text{ s}$ , (b)  $t+1.0 \text{ ms}$  and (c)  $t+2.0 \text{ ms}$ . The black iso-line signifies  $M=1$  regions, while the numbered vectors indicate regions of distinct flow features 65
- 4.17 Distribution of the pressure gradient at the nozzle symmetry axis for case 2 of Table 4.2. Time difference between the instances is  $0.08 \text{ ms}$ . 66
- 4.18 Visualisation of vortices using Q-Criterion iso-surfaces ( $Q=2 \times 10^8$ ) coloured by axial velocity values for the DES results of (a) case 1 of Table 4.2:  $p_{in}/p_{out} = 11.4 \text{ bar}/2.6 \text{ bar}$  and (b) case 2 of Table 4.2:  $p_{in}/p_{out} = 43.0 \text{ bar}/10.0 \text{ bar}$ . The figures include the part of the nozzle from  $X=-0.017 \text{ m}$  to  $X=0.11 \text{ m}$ . 67
- 5.1 Three-dimensional phase diagrams for nitrogen: (a) pressure and (b) internal energy in terms of density and temperature. 78
- 5.2 Geometry of (a) liquid oxygen injector (injector A) employed in [7] and (b) liquid nitrogen injector (injector B) employed in [8]. The panels represent the numerical domain used for the simulation. The outflow part extends downstream the injector exit to a length equal to 40 orifice diameters. 80
- 5.3 Views of the numerical grid of (a) the LOx injector and (b) the LN<sub>2</sub> injector including a focused view of the location marked with an arrow around the exit of each injector. 81
- 5.4 Grid independence analysis of the URANS numerical solution. (a) Pressure and (b) vapour volume fraction distributions on the orifice symmetry axis for three numerical grids of increasing cell number. 83

- 
- 5.5 Oxygen spray cone angle for inlet pressure of 17 bar and variable LOx injection conditions of increasing superheat degree. Conditions correspond to cases 1 to 4 of [Table 5.2](#). Spray cone angles measured at a distance equivalent to 5 nozzle diameters downstream the nozzle (see figure inset). 85
- 5.6 Contour plots of (a) Pressure, (b) Velocity magnitude, (c) Density and (d) Temperature variable distribution for cases 4 of [Table 5.2](#). Pressure based solver results are presented on the left of each subplot while density based solver results are on the right. 87
- 5.7 Distribution of (a) Pressure, (b) Axial Velocity, (c) Density and (d) Temperature along the nozzle axis of symmetry as predicted by the two approaches for case 4 of [Table 5.2](#) and as predicted by the thermal non-equilibrium model of the pressure-based solver for cases 1 to 3 of [Table 5.2](#). 88
- 5.8 Contour plots of (Column a) Pressure, (Column b) Velocity magnitude, (Column c) Temperature and (Column d) Density variable distribution for cases 1 to 4 of [Table 5.2](#). Each case is presented in a separate row. All variables are time-averaged. 89
- 5.9 Nitrogen spray cone angle for inlet pressure of 8 bar and variable LN<sub>2</sub> injection conditions of increasing superheat degree. Conditions correspond to cases 5 to 7 of [Table 5.2](#). Spray cone angles are measured at a distance equivalent to 2 nozzle diameters downstream the nozzle exit. 92
- 5.10 Time-averaged values resulting from the use of a pressure-based solver with a thermal non-equilibrium model (left) and a density-based solver utilizing a HEM (right). Distribution of (a) Pressure, (b) Axial Velocity, (c) Density and (d) Temperature along the nozzle axis of symmetry for cases 5 to 10 of [Table 5.2](#). 93
- 5.11 Velocity profiles for cases 6,7,9 and 10 of [Table 5.2](#) at  $X/D = 2$  as a function of the dimensionless radial coordinate  $Y/D$ . Inset depicts velocity contour plots in the near-nozzle region of cases 6 (upper panel) and 9 (lower panel) of [Table 5.2](#),  $R_p = 7$ . 95
- 5.12 Nitrogen injection, cases 8 to 10 of [Table 5.2](#). Comparison between shadowgraphy images as presented by Rees et. al [8] (left panel of each frame) and numerically derived results using the HEM, tabulated approach (right panel). Density gradient magnitude has been plotted using a logarithmic scale with a darker colour corresponding to higher gradients similar to the colour band of [Figure 5.13](#). 96

---

5.13	Rendering of three-dimensional spray topology by revolution of the density gradient contour (left). Density gradient contour plot (right). Numerical data correspond to case 3 of Table 5.2, $R_p = 74$ .	96
6.1	Characteristics of the Spray-G 8-hole counterbore injector.	105
6.2	Overview of the numerical domain used for the spray G investigation including enlarged details of the numerical mesh at the location of the injector hole and counterbore.	107
6.3	Contour plot over spray G hole plane of symmetry alongside the injection direction. Distribution of (a) pressure (b) velocity, (c) temperature and (d) liquid volume fraction.	109
6.4	Line plots of variable evolution along the spray G hole central axis of symmetry. Distribution of (a) pressure logarithm (b) velocity, (c) temperature and (d) density.	110
6.5	Contour plots on equidistant planes lying perpendicular to the spray G hole central axis of symmetry. Distribution of (a) pressure logarithm (b) velocity, (c) temperature and (d) liquid volume fraction.	111
6.6	Definition of (a) vectors $L_0$ to $L_3$ and (b) contour of an enlarged view of the in-nozzle variable fields. Line plots of variable evolution along the vectors $L_0$ to $L_3$ . Distribution of (c) pressure (d) velocity, (e) temperature and (f) liquid volume fraction.	112
6.7	Turbulent structures at the in- and near-nozzle area presented by a Q-criterion iso-surface of a magnitude of $1^{12}$ . Surface coloured by the magnitude of velocity.	113
A.1	Flow diagram of the implementation process of the compressible, two-phase solver “tabFoam”, for the purpose of examining the performance of HEM in the context of cryogenic flash boiling.	125

# List of Tables

3.1	Physical properties of Iso-octane, Nitrogen and Oxygen [9].	32
3.2	Antoine equation parameters of Iso-octane, Nitrogen and Oxygen [9].	33
3.3	Complete list of fluids and boundary conditions examined in this work.	33
4.1	Summary of boundary and initial conditions imposed for the numerical simulations.	48
4.2	Matrix of test cases examined. It must be noted that temperature lies in the subcritical regime for all cases.	49
4.3	Comparison between experimental and numerical results. The Hertz-Knudsen model was utilised for the flow simulations.	50
4.4	Evaluation of LOx mass-flow rate value through the orifice predicted by the two phase-change mechanisms for case 1 of Table 4.2.	56
5.1	Summary of boundary and initial conditions imposed for the numerical simulations.	82
5.2	List of examined test cases, including the operating fluid, boundary conditions and superheat $R_p = p_{sat}(T_{in})/p_{out}$ for each case.	84
5.4	Comparison between numerical predictions and experimental measurements for LN <sub>2</sub> mass flow rate in injector B.	91
6.1	Nominal dimensions and manufacturing characteristics of ECN, Spray G injector [10].	106
6.2	Boundary conditions of ECN, Spray G injector for non-flashing (Spray-G) and flashing (Spray-G2) operation [10].	106
6.3	Mass flow rate values for each injector hole during the maximum needle lift phase. Comparison of total mass flow rate with experimental values [11, 10].	108



# CHAPTER 1

## Introduction

Flash evaporation, also referred to as flash-boiling or simply flashing is a phase-changing process from liquid to vapour that takes place under the effect of abrupt pressure decrease. Flash boiling is present in many industrial and technical applications of different production sectors. Due to its “explosive” nature, the variety of conditions under which it occurs and the effect it has on the evaporating liquid, as well as the environment close to the phase change location, flash boiling is an important phenomenon to be either predicted and mitigated or exploited and enhanced. Manifestation of flash boiling can be found in flows of liquids through nozzles, orifices and valves, in the case of flash-induced instabilities in systems of natural circulation, in cooling applications of cryogenic fluids, upon failure and rupture of pressurised vessels or pipes that contain liquefied gases, in internal combustion engines for fuel spray atomisation purposes or in the event of a loss-of-coolant accident of pressurised water nuclear reactors. Furthermore, flashing is relevant to a wide range of technical applications, ranging from gas liquefaction and desalination to cryosurgery and food freezing while further investigation of flash boiling is underway for aerospace applications. The present research has been conducted under the provision of a European research program aiming to develop proper modelling tools and use them for simulating and investigating the phenomenon of flash-induced atomisation.

### 1.1 Background and motivation

The phase-change rates during flashing are very high. Due to the fast nature of the phenomenon, should it occur in an uncontrolled manner, the consequences can be destructive, leading to explosion, fire and equipment damage [12, 13, 14, 15, 16]. In the field of refrigeration, flashing during the expansion phase of cooling cycles can be the source of high noise levels [17]. Considering nuclear power-plant safety, flashing phenomena need to be taken into account since they manifest in the case of a loss of coolant accident (LOCA) [18]. On the other hand, flashing jets or spray systems

can be of use for industrial applications. NASA has developed the Compact Flash Evaporator System (CFES), an open-loop heat sink for space usage [19]. In the context of industrial waste-heat recovery, flashing has been utilized in the operating cycle of absorption heat pumps [20]. Regarding alumina production, flash evaporation is one of the key processes involved [21].

In the area of atomisation and sprays, it is evident by the supporting experimental data that, when present, flashing plays an important role in the morphology of the resulting spray. This is also acknowledged in the area of gasoline direct injection (GDI) engines, where both experimental and numerical research is extensive [22, 23]. For its effect on the morphology of the spray, flash boiling is also of great interest for space applications. Space launch vehicles use a combination of fuel and oxidiser as a means of propulsion. For modern liquid-fuelled rocket engines (LRE), liquid oxygen (LOx) is commonly used as an oxidiser while Hydrogen, Methane or highly refined kerosene (RP-1) are some of the most used fuels. First-stage rocket engines ignite and operate during lift-off in atmospheric conditions. However, the cryogenic liquids that comprise the upper-stage rocket engine propellant are injected into the combustion chamber, where near-vacuum conditions prevail prior to the ignition. The injection at low-pressure conditions results in a high superheat ratio ( $R_p$ ) of the involved fluids, thus resulting in flashing. Investigation of cryogenic flash boiling at an experimental level is important for the comprehension of such processes but is limited due to the extreme conditions of operation and storage of the fluids.

To fully understand flash boiling, experimental data are of great importance. However, experimental campaigns that focus on cryogenic liquids are scarce. The fact that most experimental data on the field have been produced by national space centres or very specialised laboratories is indicative of the high cost and difficulty of conducting cryogenic flashing experiments. The literature review included in [Chapter 2](#) presents thoroughly the experimental activity in the field, but some indicative cryogenic facilities are operated by organisations such as the German Aerospace Center (DLR), the French National Aerospace Centre (ONERA) and the American National Aeronautics and Space Administration (NASA). Research conducted within the aforementioned laboratories includes the work of Hendricks et al. [5] where two-phase flows of liquid Oxygen and Nitrogen through different orifices were investigated under a wide range of conditions, the work of Lamanna et al. [7] in which the behaviour of fully flashing liquid Oxygen and Ethanol sprays was documented and the work of Rees et al. [24] that reported on the morphology of flash boiling liquid nitrogen sprays.

It is clear from the literature research that the availability of cryogenic flashing

data is limited, thus the development of accurate and robust modelling methodologies is an important part of the research on flash-boiling and an alternative approach towards the understanding of the phenomenon. The motivation for the present work is drawn by the need to investigate, analyse and better utilise the phenomenon of flash evaporation in the context of cryogenic superheated injection and spray formation. For this investigation, the necessary numerical tools and models were developed, tested and applied in a wide range of operating conditions, providing additional insight to the experimental observation.

## **1.2 Objectives**

The main objective of this work was to propose and evaluate a universal modelling framework suitable for the prediction of the evolution of multiphase flows with a main focus on flash-boiling conditions and cryogenic fluids. The methodology was developed within the OpenFOAM open-source environment and was evaluated for in-nozzle as well as for spray-formation prediction performance. More specifically, a time-resolved, explicit, density-based solver implementing a Mach-number consistent numerical flux scheme was used. Thermodynamic properties of the operating fluids were determined by using the Helmholtz energy Equation of State (EOS) and inserted in the numerical code in tabulated form. Due to the interest in investigating conditions resembling second-stage rocket engine ignition, liquid oxygen has been selected as the operating fluid due to its extensive use as an oxidiser. Further evaluation of the developed methodology was an objective of this work. This was possible by applying the methodology to relevant experimental conditions. Experimental data from liquid nitrogen flashing spray formation were used. A secondary objective of the present work was the implementation of a kinetic-theory-based phase-change model to a coupled (pressure-based) solver. This part of the work was materialized within the ANSYS-Fluent environment. The aim was the comparative evaluation of all relevant results and to highlight the advantages and disadvantages of used approaches. The kinetic-theory-based phase-change model was also selected to be used in a Large Eddy Simulation (LES) framework for relevant flash boiling conditions to assess its performance.

### 1.3 Outline

This thesis comprises seven chapters. The previous sections of the current chapter briefly presented the research background on the topic of cryogenic flash-boiling as well as the motivation for performing the work that is included in the following chapters. In [Chapter 2](#) an overview of the mechanisms of flashing is presented. Nucleation and bubble growth concepts are discussed. Relevant experimental cryogenic campaigns are highlighted and different numerical modelling approaches for flash-boiling conditions are presented. [Chapter 3](#) describes the relevant numerical methodologies that were utilised in the present work and the complete range of boundary conditions that have been examined numerically. The chapters that follow include the specifics of all the performed numerical investigations and their results. More specifically, [Chapter 4](#) includes work on the numerical modelling of liquid Oxygen flow under sub- and super-critical conditions, [Chapter 5](#) presents the research on numerical modelling of liquid Oxygen and Nitrogen flow under flashing conditions and in [Chapter 6](#) the results of a Large eddy simulation of iso-Octane flow through a gasoline injector under flashing conditions are presented. Finally, [Chapter 7](#) sums up the conclusions drawn by the complete numerical work in this thesis.

# CHAPTER 2

## Literature review

### 2.1 Overview

Flashing manifests when a liquid reaches a superheated state, i.e. its pressure and temperature bring the liquid to a metastable condition. On a diagram of pressure ( $p$ ) and specific volume ( $v$ ), the metastable regions of either superheated liquid or supercooled vapour lie on the overlap of the areas within the saturation dome and outside the spinodal curves. As displayed in [Figure 2.1](#) there are two possible ways for a subcooled liquid, being at state “A”, to reach a metastable (superheated) state. One possible way is the isobaric heating, path A-T, and the other is the isothermal depressurisation, path A-P. For each metastable state ( $p, T$ ), the degree of superheat of the liquid is defined as  $\Delta T = T - T_{sat}(p)$ .

The degree of superheat that a liquid can reach depends on the rate at which each process takes place. The faster the process, the higher the superheat degree that a liquid can attain before it reaches the theoretical thermodynamic limit of the spinodal curve where  $(\partial p/\partial v)_T = 0$ . This limit cannot be achieved due to practical reasons, such as impurities within the liquid, pre-existing gas that is dissolved in the liquid body, wall roughness of the liquid container, and the inability to achieve high depressurisation or heating rates. Apart from the superheat degree,  $\Delta T$ , the liquid superheat is expressed in the literature using the magnitude of the “superheat ratio” or simply “superheat”,  $R_p$ , which is defined as  $R_p = p_{sat}(T_{in})/p_{amb}$ , where  $p_{sat}(T_{in})$  is the saturation pressure of the liquid at the inlet temperature and  $p_{amb}$  is the ambient pressure of the injection chamber where the initially subcooled liquid is being injected.

### 2.2 Nucleation

Within the body of a superheated liquid, the thermodynamic properties exhibit minor fluctuations that can lead to the initiation of phase transition towards a stable state. The first step of this process is nucleation, i.e. the formation of vapour bubbles within

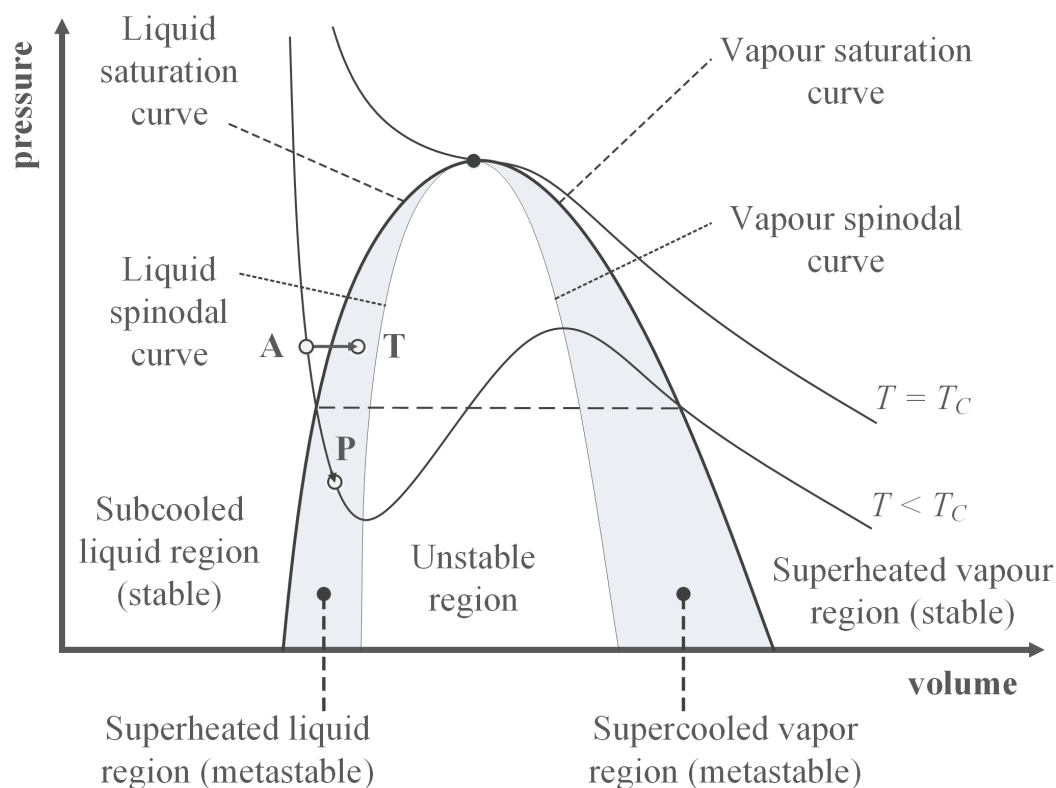


**Figure 2.1:** Schematics of pressure-volume isotherms for a pure fluid.

the liquid body. The nucleation process can manifest in two different ways depending on the superheat degree [25]. In the case of homogeneous nucleation, the forming of the vapour bubbles takes place everywhere within the liquid volume whereas in heterogeneous nucleation, the formation of bubbles initiates on the interfacial regions between the liquid and a, usually, solid boundary [26, 27, 28] or even impurities such as dissolved gas.

According to classical nucleation theory, Equation 2.1 describes the formation energy of a nucleus with radius  $r$ . The first term represents the interfacial energy between the two phases and the second term is the difference in volume free energy between the phases. If we define a large homogenous spherical droplet as a cluster, the maximum point ( $\Delta G^*$ ) of Equation 2.1 corresponds to the critical cluster size, as described by Equation 2.2.  $\Delta G^*$  represents the energy barrier that a system has to overcome in order to reach a new stable condition. A nucleation cluster that is larger than the critical nucleation cluster will, on average, grow up whereas a cluster that is smaller will, on average, collapse. For flashing conditions, the chemical potential

of the liquid phase is higher than the chemical potential of the vapour phase. This chemical potential difference ( $\Delta\mu_c$ ) is the driving force for the transformation between liquid and vapour phases [29].

$$\Delta G = 4\pi r^2 \sigma - \frac{4\pi}{3} r^3 \Delta\mu_c \quad (2.1)$$

$$\Delta G^* = \frac{16\pi}{3} \frac{v^{l^2} \sigma^3}{|\Delta\mu_c|^2} \quad (2.2)$$

For a system, a nucleation rate can be expressed as a function of the energy barrier (Equation 2.3).

$$J = J_0 \exp\left(-\frac{\Delta G^*}{k_B T}\right) \quad (2.3)$$

where  $J_0$  is a pre-exponential factor. Since the nucleation rate is clearly sensitive to the quantity within the exponential, Lamanna et al. [30] proposed the dimensionless parameter  $\chi$ , or energy barrier to nucleation (Equation 2.4), as a criterion for identifying the transition to fully flashing conditions. For values of  $\chi$  higher than 1, a cluster does not have the internal energy needed to overcome the nucleation barrier, while for values of  $\chi$  lower than 1, bubble nuclei can be formed.

$$\chi = \frac{\Delta G^*}{k_B T} \quad (2.4)$$

Another factor that can affect the nucleation inception and thus flashing is the fluctuation of pressure around an average value, due to turbulence. In the example of converging nozzles, pressure fluctuations can lead to flashing onset earlier in the nozzle than anticipated and therefore interfering with the quality of the resulting spray or jet. Finally, regarding the existence of dissolved gas, studies conclude that even a small amount results in reduced attainable superheat [31].

## 2.3 Bubble growth

After the initialization of nucleation, when the conditions are favourable e.g. within an atomization system, the bubbles that have formed are undergoing a growth stage. Bubble size is a very significant parameter, however, the bubble growth process is non-linear and analytical correlations can only be used under simplifying assumptions. For the case of a spherical bubble, Rayleigh [32] was the first to formulate a bubble growth equation (Equation 2.5). In his work, viscosity ( $\mu$ ) and surface tension ( $\sigma$ ) are not considered and the growth process is controlled by inertial forces.

$$R\ddot{R} + \frac{3}{2}\dot{R}^2 = \frac{p_v - p_\infty}{\rho_l} \quad (2.5)$$

After a nucleus is created and provided that its initial dimensions exceed a radius of  $R_i = 2\sigma/(p_v - p_\infty)$ , small fluctuations of pressure difference across the surface of the bubble can lead to either collapsing or growth. By assuming a constant growth rate, Equation 2.5 solved for  $\dot{R}$ , yields:

$$\dot{R} = \sqrt{\frac{2(p_v - p_\infty)}{\rho_l}} \quad (2.6)$$

Finally, if the effects of surface tension and viscosity are introduced in the problem formulation, Equation 2.5 results in Equation 2.7, also known as the generalized Rayleigh-Plesset equation [33]:

$$R\ddot{R} + \frac{3}{2}\dot{R}^2 = \frac{1}{\rho_l} \left( p_v - p_\infty - \frac{2\sigma}{R} - \frac{4\mu}{R}\dot{R} \right) \quad (2.7)$$

Four stages can be identified in the process of bubble growth within superheated liquid [34]. In the first stage, the bubble size is small and the growth rate is dominated by the surface tension or even restricted by it. During the second stage and for a large enough initial superheat, the growth rate reaches the value of Equation 2.6. In stage three, the liquid shell that surrounds the bubble is cooled down due to the removal of the heat needed for evaporation and at the same time, the vapour pressure decreases. At this stage, both inertia and thermal diffusion control the bubble growth rate. Finally, during stage four, the growth is controlled by thermal diffusion, i.e. by the supply of heat to the vapour-liquid interface. From Equation 2.7 becomes apparent that as the bubble increases its radius, surface tension and viscosity terms decrease and the bubble pressure,  $p_v$ , approaches the ambient pressure,  $p_\infty$ , and consequently, temperature  $T_\infty$ .

Regarding the prediction of bubble growth, different models have been proposed. In the work of Plesset and Zwick [35], an asymptotic solution for the bubble radius is presented.

$$\dot{R} = \left( \frac{3\alpha}{\pi t} \right)^{1/2} \frac{\rho_l c_l (T_\infty - T_{sat})}{L \rho_v} \quad (2.8)$$

where  $\alpha$  is the speed of sound,  $L$  is the latent heat and  $t$  is a generalized time variable. In this type of expression, bubble growth can be described as thermal diffusion controlled. In agreement with Equation 2.8 were also the solutions of Forster and Zuber [36],

Birkhoff [37] and Scriven [38].

An equation that would combine the inertia-driven bubble growth with the thermal diffusion growth was presented in the work of Mikic et al. [28]. By using the linearized Clausius-Clapeyron equation for the vapour pressure curve and by assuming thermal equilibrium in the vapour bubble (Equation 2.9), a generalized closed-form expression can be formulated (Equation 2.10) applicable for both the inertia-driven stage and the thermal diffusion stage of bubble growth. A similar approach has been presented in the work of Miyatake and Tanaka [39, 40].

$$p_v - p_\infty = \frac{\rho_v L}{T_{sat}} (T_v - T_{sat}) \quad (2.9)$$

$$R^* = \frac{2}{3} [(t^* + 1)^{3/2} - (t^*)^{3/2} - 1], \quad R^* = \frac{R}{B^2/A}, \quad t^* = \frac{t}{B^2/A^2},$$

$$A = \left[ \frac{2(T_\infty - T_{sat})L\rho_v}{3T_{sat}\rho_l} \right]^{1/2}, \quad B = \left[ \frac{12}{\pi} J_\alpha^2 \alpha \right]^{1/2}, \quad J_\alpha = \frac{\rho_l C_{pl} (T_\infty - T_{sat})}{\rho_v L} \quad (2.10)$$

Theofanous and Patel [41] used a different linearization form of the Clausius-Clapeyron equation to account for the underestimation of the bubble growth rate for higher superheat degrees. They suggested the following expression that described the experimental data of R113 more accurately:

$$p_v - p_\infty = \frac{\rho_v (T_\infty) - p_\infty}{T_\infty - T_{sat}} (T_v - T_{sat}) \quad (2.11)$$

Figure 2.2 presents in a comparative manner the predicted bubble growth in superheated water. More specifically, the dimensionless bubble radius,  $R^*$ , is plotted as a function of dimensionless time,  $t^*$ , based on proposed expressions from the literature. The factors that mostly affect the accuracy of bubble growth predictions lie predominantly in assumptions that have been made for the derivation of a bubble growth expression. The assumption of thermal equilibrium at the interphase of a vapour bubble and the surrounding liquid might not be accurate at all times. In such cases, the departure from equilibrium can be dealt with by using a proper accommodation coefficient. Further discussion on the matter of thermal equilibrium is presented in paragraph 2.6. The assumption of common velocity between a bubble and the surrounding liquid can also influence the predicted bubble growth, since, in the case of relative motion, the heat transfer can be affected. In a case where there is relative motion, assuming a spherical bubble can also lead to deviations. Finally, bubble

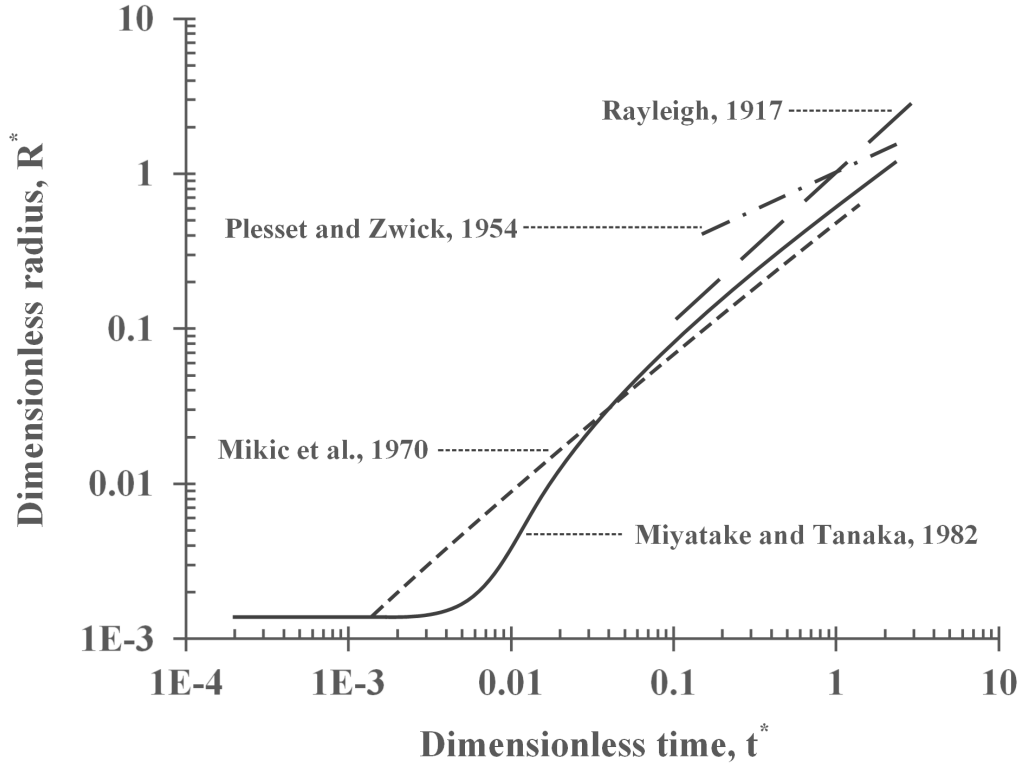


**Figure 2.2:** Comparison of different models for predicting bubble growth in superheated water (based on [1]).

growth can be limited by turbulence, as bubbles are bound to be broken by vortices of lesser size. With regard to the bubble growth assumptions, certain characteristics of a flow can be determined by non-dimensional numbers. For the following definitions, the characteristic length,  $L$ , in the case of a bubble of radius  $R$  is  $L = 2R$ .

$$\text{Reynolds number: } R_e = \frac{\rho UL}{\mu} \quad (2.12)$$

$$\text{Weber number: } W_e = \frac{\rho_l U^2 L}{\sigma} \quad (2.13)$$

$$\text{Froude number: } F_r = \frac{U}{\sqrt{gL}} \quad (2.14)$$

$$\text{Strouhal number: } S_t = \frac{fL}{U} \quad (2.15)$$

$$\text{Pradtl number: } P_r = \frac{C_p \mu}{\lambda} \quad (2.16)$$

$$\text{Mach number: } M = \frac{U}{c} \quad (2.17)$$

## 2.4 Flash boiling atomization

Flash boiling can be utilized for atomization purposes as is one of the most effective means of generating fine and narrow-dispersed sprays [31]. Flash atomization finds application in various fields, such as coatings, agriculture, combustion, turbines, sensing, desalination, energy storage, refrigeration, pharmaceutical, and even in household sprays (e.g. inkjet printers) [3]. The complex nature of the flash-atomization process, however, does not always allow for the full exploitation of the phenomenon. The sequence of processes that take place for flash atomization to occur includes intense nucleation, fast bubble growth and, eventually, liquid atomization. The quality of the resulting spray is determined by the inter-relationship between those distinctive processes.

Regarding spray quality, the pharmaceutical and automotive industries can be given as examples. Fine spray is important in pharmaceutical sprays since large droplets lead to oral thrush in about 5% of the patients, as well as cough and bronchospasm [42]. Similarly, fine spray and a shorter penetration length (that is often accompanied by wide cone angles) are crucial for fuel injection systems, where droplet wall impingement should be avoided [43], and lower injection pressure is important for safety issues [44]. Overall, the desired spray qualities that can be achieved by flash atomization are a smaller Sauter mean diameter (SMD) for lower pressure differences, more uniform distribution, wider cone angles and, finally, shorter breakup (penetration) length. Those qualities can be obtained by increasing the superheat degree (i.e. increasing the injection temperature or decreasing the ambient pressure), thus leading the breakup regime to transition from the mechanical breakup towards the fully flashing regime.

Regarding the mean diameter, [Figure 2.3](#) presents a correlation of SMD as a function of (a) superheat degree and (b) superheat ratio,  $R_p = p_{sat}(T_{inj})/p_{amb}$ , where  $p_{sat}(T_{inj})$  is the saturation pressure of the injected liquid at the initial injection temperature and  $p_{amb}$  refers to the ambient pressure at the outlet. It can be observed that since subcooled fluids will not flash, the liquid breakup will take place only due to mechanical shear and hydrodynamic instabilities. During the partial (transition) regime, the thermophysical properties of the liquid phase and its expansion are non-negligible [2]. Finally, Beyond the cutoff point, the SMD is assumed to decrease very slowly ( $\sim 0.1 \mu m/K$ ). In terms of spray cone angle, due to different radial and axial

velocities, the spray spreads in a conical formation. As the outer ligaments decelerate, the air is entrained within the ligaments and the spray is divided into concentric conical sprays [45]. In the case of flashing spray, the entrainment inherently occurs earlier, contributing to the increase in cone angle and to decrease in the breakup length.[3].

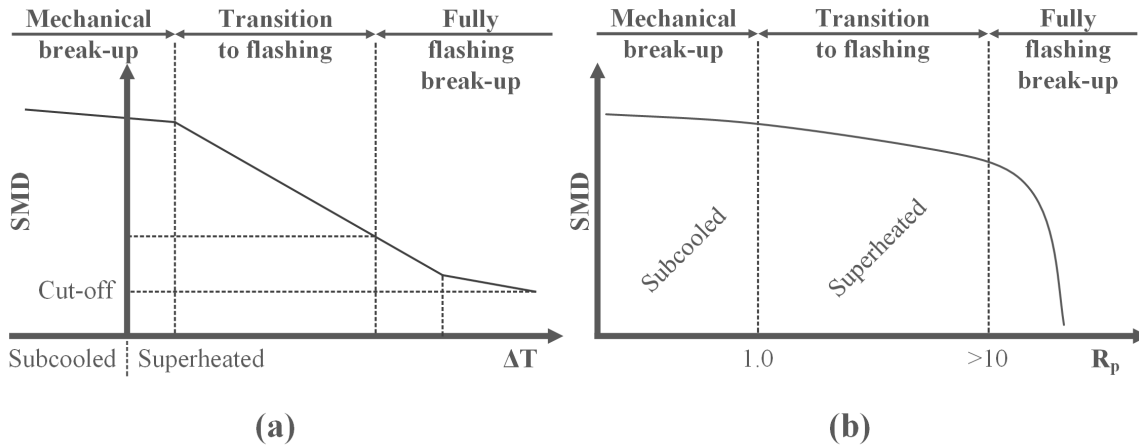


**Figure 2.3:** Variation of the Sauter mean diameter (SMD) with (a) superheat degree (adapted from [2]) and (b) superheat ratio (adapted from [3]).

## 2.5 Cryogenic flows and experimental data

Flash boiling in the context of cryogenic fluids is relevant in many technological applications, ranging from dermatological surgery to liquid rocket engine (LRE) technologies. The present work focuses on the latter, where, in the case of upper-stage rocket engines that operate in a near-vacuum pressure environment, flashing can manifest during the engine ignition of the rocket propellant. The appearance of flash-boiling has an impact on the propellant atomisation and final distribution within the area of the combustor. Understanding the process of propellant disintegration under superheated conditions is paramount for appropriate ignition system design for operation under all flight conditions. Although experimental data on the injection of cryogenic fluids under superheated conditions are needed in order to understand cryogenic flashing, the relevant available database is extremely limited, for reasons well explained in the work of Lamanna [46]. In this paragraph, relevant experimental research in the area of cryogenic fluids for a wide range of conditions is presented.

In the field of Aerospace, Hendricks et al. in the NASA technical report of 1976, experimented with two-phase flows of LOx and LN<sub>2</sub>. Two different types of converging-diverging nozzles were tested and the operating conditions ranged from

sub- to super-critical. Pressure distribution within the nozzles and mass flow rates from a wide range of conditions were reported. Data from this investigation were used in the present work for validation purposes.

In research regarding rocket fuel propellant injection, Mayer and Tamura [47] presented flow visualizations and measurements from injection, spray formation, supercritical mixing, evaporation, and combustion in a liquid rocket engine combustor at supercritical chamber pressures up to 10.0 MPa. The investigation revealed a remarkable difference between subcritical spray formation and evaporation, and the supercritical injection and mixing processes. More specifically when chamber pressure approaches supercritical values the injection can no longer be regarded as an atomization or spray formation process as, under these conditions, droplets no longer exist. In a later work of Mayer et al. [48] cryogenic fluids were injected into various gases under both cold-flow and hot-fire conditions and the results were reported by means of flashlight photography and high-speed cinematography. Both subcritical and supercritical conditions were considered. The differences between subcritical spray formation and evaporation and supercritical injection and mixing were distinct. Close to critical chamber pressure a fluid/fluid mixing process rather than spray formation can be observed. This mixing process was found to be very sensitive to small fluctuations in pressure, temperature, local mixture concentrations, and initial injection conditions.

In the area of cryogenic propellant combustion, the Mascotte test bench developed by ONERA provides data that aims to give insight into the physical and chemical aspects of the process. Habiballah et al. [49] and Vingert et al. [50] present the results produced during studies of high-pressure cryogenic flames conducted on the Mascotte facility. The measurement techniques include high-speed photography, shadowgraphy, backlighting, and Coherent Anti-Stokes Raman Scattering (CARS). The findings reveal differences of flame structure in sub-and supercritical regimes and evidence of the absence of ligaments and droplets around the LOx jet at supercritical pressure are presented. Operating conditions from those investigations were used in the present work as guidelines for the choice of specific sets of boundary conditions.

Lamanna et al. [30] present a systematic study on flashing atomisation, including storable and retrograde fluids. Their analysis indicates that bubble nucleation is the rate-controlling process for both the transition to fully flashing and for the spray lateral spreading. For very high values of initial superheat, a complex shock wave structure appears around the flashing jets. Such shock systems are observed consistently in both standard and retrograde substances. In subsequent work, Lamanna et al. [7] widened the investigation to cryogenic fluids and researched the disintegration of highly

superheated jets by means of high-speed shadowgraphy. They postulate that transition to the fully flashing regime occurs when the excess in chemical potential equals the surface energy work or, analogously, the non-dimensional expression for the energy barrier is of order 1. Data from this investigation were used in the present work to assess the predictive capability of the presented methodologies.

Luo and Haidn [29] have performed experimental characterization of flashing phenomena with cryogenic fluid under vacuum conditions. Their spray morphological study conducted that with the increase of liquid superheat, the spray undergoes a process of shifting from the mechanical atomization regime to the flashing-controlled atomization regime. The fully flashing sprays examined, featured wide bell-shaped spray angles and finely atomized droplets. Their analysis of the lateral spray propagation concluded that the superheat enhances the spray angle up to a certain threshold. Moreover, the study showed that bubble nucleation is a controlling factor for the evolution of the flashing process. Considering the non-dimensional energy barrier to nucleation,  $\chi$ , the research came to the conclusion that  $\chi$  can work as an indicator for the cryogenic flashing transition process with the onset of the fully flashing regime taking place on a  $\chi$  value of around one.

Rees et al. [24] analysed using high-speed shadowgraphy 26 superheated liquid nitrogen (LN<sub>2</sub>) sprays under varying degrees of superheat in order to investigate the morphology and typical behaviour of cryogenic flash boiling sprays. Their research confirmed that an increase in the superheat degree leads to the transition from narrow and turbulent sprays, to open-wide fine and well-atomized sprays. However, after a certain superheat level, the spray patterns remain unaltered. It was calculated that the maximum spray angle of the spray was about 170°. In their work, they also tested the effect of the injection pressure and they concluded that halving the injection pressure leads to wider sprays for lower degrees of superheat. This is justified due to the more intense nucleation within the injection orifice. Finally, shock structures like a barrel shock and a Mach disc were observed as well as the solidification of nitrogen around the envelope of the most highly superheated LN<sub>2</sub> sprays revealing temperatures below the triple point. Data from this investigation were used in the present work to assess the predictive capability of the presented methodologies.

## 2.6 Numerical modelling of flashing flows

Many models and numerical approaches have been proposed with the purpose of simulating a variety of flashing conditions. Those endeavours range from one-dimensional

simulations and simple empirical models to three-dimensional simulations utilising more complex models. According to the categorisation of Liao and Lucas [18] the modelling approaches can be divided into four main groups. The groups are formed by considering the approach of each model in terms of homogeneity, i.e. all involved phases assume the same velocity, and thermodynamic equilibrium, i.e. the assumption that the temperature is equal for the liquid and the vapour phase on the interphase. **Figure 2.4** represents a vapour bubble within a liquid environment. The temperature variation of the vapour,  $T_v$ , and the liquid,  $T_l$ , are presented for the cases of thermal equilibrium and thermal non-equilibrium.

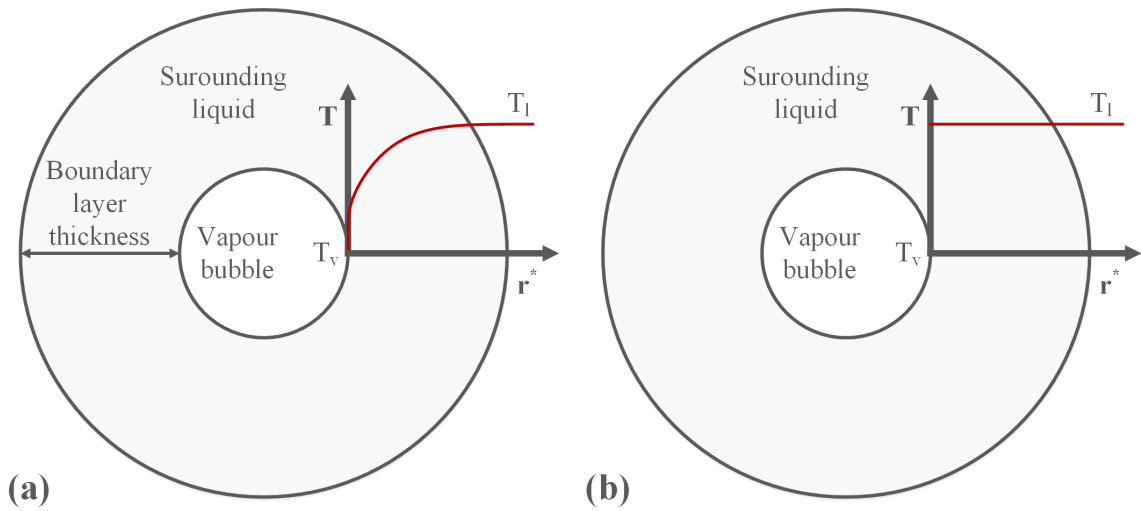


**Figure 2.4:** Representation of a growing vapour bubble within the liquid environment under thermodynamic (a) equilibrium and (b) non-equilibrium (based on [4].)

Based on their assumptions, flashing models can be categorised as (a) homogeneous equilibrium, (b) non-homogeneous equilibrium, (c) homogeneous non-equilibrium and (d) non-homogeneous non-equilibrium models. **Figure 2.5** presents a visual classification of available modelling approaches and indicative research under each category, while a detailed review of the modelling work under each category is presented in the next paragraphs.

### 2.6.1 Homogeneous equilibrium models

Homogeneous Equilibrium Models (HEM) are the most simplistic of the models in the four categories. Those models represent the two-phase flashing flow as an equivalent single-phase flow with assumptions of homogeneous velocity, i.e. common velocity at the interface of liquid and vapour areas, and thermal equilibrium, i.e. the shared

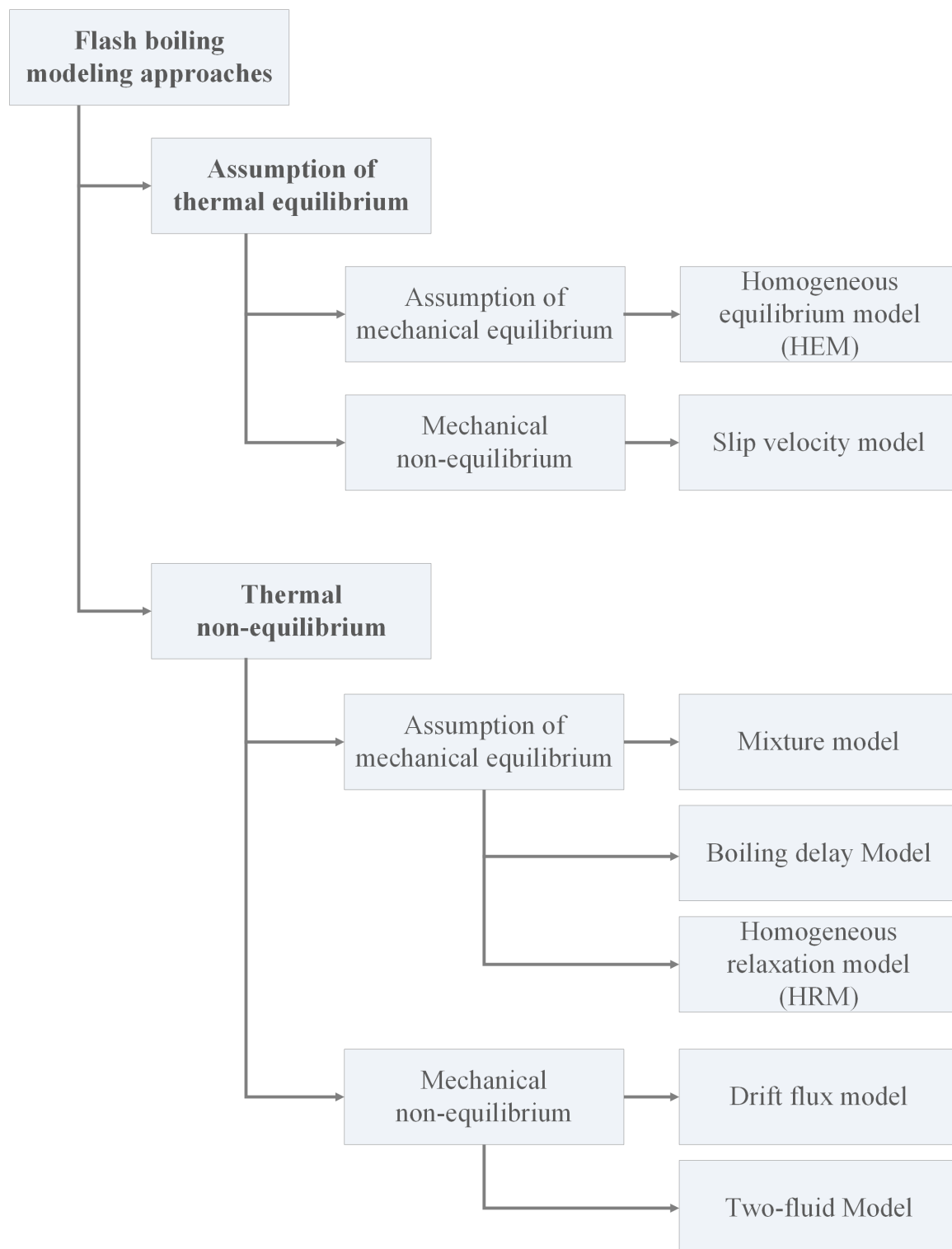


**Figure 2.5:** Classification of available approaches for modelling flashing flows depending on the assumptions on thermal and mechanical equilibrium.

temperature at the aforementioned interface. Most HEM applications evaluate the thermal properties of the flow with the use of interpolation between the liquid and vapour property values based on the equilibrium quality. Such HEM applications have been used for nuclear reactor safety analysis on the possibility of Loss-Of-Coolant-Accident (LOCA). Work on critical flow has been made by Leung [51], who established that the model works well for long pipes, where the time is sufficient for equilibration between the phases. Regarding critical flow rates for short pipes, flow rates predicted by the HEM are considerably less than those obtained experimentally [52, 53, 54, 55]. On the matter of flow instability, Hu et al. [56] and Podowski [57] report that the predictions of HEM are conservative in comparison to slip and two-fluid models, due to the fact that the HEM void fraction is higher. Finally, Richter [58] reaches the conclusion that during the inception of steady-state flashing, the assumption momentum equilibrium is applicable.

### 2.6.2 Non-homogeneous equilibrium models

The Non-Homogeneous Equilibrium Models (NHEM) also follow the assumption of thermal equilibrium, but contrary to the assumption of the homogeneous models of complete momentum transfer between the two phases, they theorise that the two phases do not share a common velocity. Early implementations of such models that investigate critical flow through long tubes [59, 60, 52, 61], assume thermodynamic equilibrium but relax the requirement of equal phase velocities by introducing a velocity slip ratio. In a comparative study by Attou et al. [62] an extreme case of NHEM, was compared to a HEM. Due to the fact that momentum is completely transferred in HEM, the liquid that is injected within a gas environment, is found to numerically decelerate faster than the experimental measurements. On the other hand, the use of NHEM causes the liquid to decelerate slower. A more complex approach is the use of the drift-flux model where void distribution and vapour drift velocity are evaluated empirically. It is simpler than the two-fluid model, however, it requires some drastic constitutive assumptions causing some of the important characteristics of two-phase flow to be lost. In the work of Hu et al. [63] it was found that the steady-state prediction of natural circulation flow rates was larger than those of a two-fluid model at both low and high pressure. The stability analysis of a boiling natural circulation loop undertaken by Inada et al. [64] resulted in an overprediction of velocity and flow rates.

### 2.6.3 Homogeneous non-equilibrium models

Thermal non-equilibrium is considered an important feature of flashing flows. It is caused by the nucleation delay and limited rates of vapour generation. The methods to describe thermal non-equilibrium can be categorized into four types of models: (a) empirical models, (b) relaxation models, (c) delayed equilibrium models and (d) physically based models. Empirical models are mostly based on HEM on which an empirical factor is introduced and adjusted accordingly in order to express the thermal non-equilibrium effects. In the work of Henry and Fauke [60] a correction factor was introduced. This empirical factor was defined based on the deviation of the experimental flow rates and the HEM predictions and it practically adjusted the vapour generation rate to a fraction of the equilibrium driven value. Simpson and Silver [65] and Edwards [66] introduced a homogeneous model that employs two empirical coefficients to account for the non-equilibrium nucleation process. One is the time delay for bubble nucleation, and the other is the number concentration of bubble nuclei. Finally, empirical models taking into consideration the pressure undershoot have also been proposed. Such is the work of Lackme [67] who used the assumption that evaporation starts for pressure values 5% below the saturation pressure corresponding to the initial liquid temperature.

Relaxation models are based on the idea that the actual value of quality,  $x$ , is initially lower than the equilibrium value,  $x_e$ , but eventually relaxes and gradually approaches equilibrium. The homogeneous relaxation model (HRM) was proposed by Bilicki and Kestin [68]. The model comprised the HEM equations and an additional equation that describes the rate of  $x$  approaching the local equilibrium value. The HRM introduces a coefficient called relaxation time that is a function of pressure, enthalpy and current  $x$  value. Regarding HRM, relaxation time functions can be derived from different variables and may vary. Downar-Zapolski et al. [69] derived a correlation for the relaxation time for the “Super Moby Dick” geometry under critical flow rates [70]. Mohammadein [71] derived a formula for the thermal relaxation time by analytically solving energy and relaxation equations. It is important to note that all derived relaxation time correlations include empirical coefficients that are undeniably the main factors affecting the resulting vapour production and distribution. Moreover, HRM is found to predict non-physically large relaxation time scales in some cases, e.g. low temperatures [72].

The concept of the Delayed Equilibrium model (DEM) is not as widespread as the previously presented non-equilibrium model types. It is based on the assumption that the flashing flow is a mixture composed of three phases: saturated liquid, saturated

vapour and metastable liquid [73]. The mixture is at equilibrium with regard to pressure and phase velocities, but the metastable liquid is in thermal non-equilibrium with the saturated phases and is assumed to expand in an isentropic manner. An extra mass balance equation for the metastable liquid is added to the system. In the work of De Lorenzo et al. [74] the DEM is presented in comparison to HEM, the Moody non-homogeneous model and the Henry-Fauske non-equilibrium model. More than 450 experimental data sets were used to assess the accuracy of the tested models. The writers found that HEM produces good results in evaluating the critical mass flow rates for long tubes but seems to fail to predict the pressure undershoot. Moody's model was found unsuitable under two-phase stagnation conditions. The Henry-Fauske model produced good predictions for the discharge of saturated vapour or two-phase mixtures from nozzles and orifices but overestimated the critical mass flow in long tubes while underestimating it in the case of subcooled or saturated water through short pipes and nozzles ( $L/D < 5$ ) [75]. Finally, DEM exhibited reliable results for a range of tube lengths in terms of both critical pressure and critical mass flux.

Due to the incomplete comprehension of the flashing process, an exact definition of the non-equilibrium effects is not available and therefore the accuracy level of the results of a model is not necessarily proportional to its complexity. Physically based models focus predominantly on the nucleation and heat transfer between involved phases. An example of such models is the model of Wolfert et al. [76] that combined cumulatively the heat diffusion model of Plesset and Zwick [35] and the convection model of Ruckenstein [77] and demonstrated good applicability in a variety of experimental conditions.

#### 2.6.4 Non-homogeneous non-equilibrium models

In addition to taking into account the non-equilibrium effects related to the nucleation and heat transfer, the non-homogeneous non-equilibrium models take into consideration the difference in the velocity between the gas and liquid phases with the use of the drift-flux model or by adopting a two-fluid model approach.

A drift-flux model has been applied by Kroeger [78] to describe pipe blowdown conditions reported by Edwards and Q'Brien [66]. The non-equilibrium effect was taken into account using a relaxation-type model. The author concludes that non-equilibrium effects were not clear, and agreement with the experimental results could be reached with the use of either a homogeneous or relaxation model. Elias and Chambé [79] presented a non-equilibrium drift-flux model that assumes that the evaporation rate is

dictated by the heat transfer between the two phases. The simulations showed that neglecting the delay on nucleation inception in the case when the phase change has not initiated at the inlet, results in a systematic under-prediction of the critical flow rate. In the case when the fluid at the inlet comprises two phases, this behaviour was not observed. Moreover, the authors mention the inherent limitations of the drift-flux model in the case of non-equilibrium flow configurations. Saha et al. [80] developed a non-equilibrium model with different interphase heat transfer considerations. The root mean square of conduction and convection heat transfer coefficients was used in the calculations and the bubble number density needed to estimate the interfacial area density was determined by fitting the model to experimental data. Good agreement was achieved for bubbly flows but in the case of bubbly-slug flows, the results were found to deviate. An improvement to the drift-flux model came from Riznic et al. [81]. The authors, instead of assuming a constant bubble density, introduced a bubble number transport equation. Moreover, with regard to the effects of variable pressure on the conduction bubble growth model, they concluded that bubble radius will increase by a factor of  $t^{n+1/2}$ , where  $t$  is the time variable, instead of  $t^{1/2}$  that would be the growth expected based on the initial superheat.

Overall, the drift-flux model has exhibited limitations in the case of acoustic wave propagations, choking phenomena and high-frequency instabilities [82, 83]. On the other hand, the two-fluid model is found to be more accurate in calculating the relative velocity between gas and liquid phases [80] but it is important for the momentum transfer to be modelled accurately. The two-fluid model has been used in the work of Rivard and Travis [84] where the flow rate and pressure results showed good agreement for various nozzle geometries. Richter [58] implemented the two-fluid model to investigate steam-water mixtures through various nozzles and calculate the critical flow rate. He hypothesized that convection was the main mechanism of heat transfer between the two phases and considered different flow regimes. The research concluded that thermal non-equilibrium was a significant factor for bubbly flow regimes while hydrodynamic non-homogeneity had an influence on the churn-turbulent flow regime results. For analysing flashing flows through pipes and nozzles, Wein [85] developed a two-fluid model consisting of six conservation equations of mass and momentum, liquid thermal energy and bubble number transport and considering nucleation both on the wall and in the bulk fluid. The results supported the hypothesis that non-equilibrium effects become more important as the vapour volume fraction increases.

# CHAPTER 3

## Numerical methodology

This chapter describes all the numerical methodologies that have been utilised for proceeding with the simulation research that is presented in chapters 4, 5, and 6. All the performed research work involves numerical investigation of two-phase flows for a range of operating conditions. The conservation equations that describe the fluid movement are initially presented in [Section 3.1](#). The treatment of the turbulence closure problem leads to the formulation of the unsteady Reynolds-averaged Navier-Stokes (URANS) framework, the Detached Eddy Simulation (DES) framework and the Large Eddy Simulation (LES) framework, all of which, have been used in this work. An important objective of this work is to evaluate and compare the effectiveness of phase-change models that are based on different assumptions, i.e. thermal non-equilibrium and thermal equilibrium. The non-equilibrium phase-change model was implemented with the use of a pressure-based solver, whereas the homogeneous equilibrium phase-change model (HEM) was implemented with the use of a density-based solver. Information regarding the use of those types of solvers and their interaction with the phase-change models is included in [Section 3.2](#). The equations of state (EOS) that have been utilized are presented in [Section 3.3](#). The derivation of thermodynamic properties from Helmholtz energy EOS and the process of tabulation of those properties is also described. As flash boiling is an intense phase-change process, all the numerical research that has been conducted focuses on two-phase flows and the underlying phase-change mechanisms. The phase-change models that have been used are described in [Section 3.4](#). Regarding the thermodynamic properties of the working fluids, namely oxygen, nitrogen and iso-octane, basic fluid information, constants and the selected equations of state and their characteristics are presented in [Section 3.5](#). Finally, the complete list of examined conditions is presented.

### 3.1 Conservation equations

The work that is presented here, considers unsteady, turbulent, compressible, multi-phase flows of viscous Newtonian fluids. The behaviour of such flows can be described by employing a set of conservation equations in terms of mass (Equation 3.1), momentum (Equation 3.2), also referred to as the Navier-Stokes equations, and energy (Equation 3.3).

$$\frac{\partial \rho}{\partial t} + \nabla \cdot (\rho \vec{v}) = S_m \quad (3.1)$$

$$\frac{\partial}{\partial t} (\rho \vec{v}) + \nabla \cdot (\rho \vec{v} \vec{v}) = -\nabla p + \nabla \cdot (\bar{\tau}) + S_f \quad (3.2)$$

$$\frac{\partial}{\partial t} (\rho E) + \nabla \cdot (\rho E \vec{v}) = -\nabla p \vec{v} - \nabla q + \nabla \cdot (\bar{\tau} \vec{v}) + S_h \quad (3.3)$$

where  $\rho$  is the density of the fluid or mixture,

$\vec{v}$  is the fluid velocity vector,

$t$  is time,

$p$  is the static pressure,

$\bar{\tau}$  is the stress tensor,

$E$  is the total energy and

$S_m, S_f$  and  $S_h$  are the sum of all mass, momentum and energy sources applied.

The stress tensor,  $\bar{\tau}$ , is calculated by equation Equation 3.4.

$$\bar{\tau} = \mu \left[ (\nabla \vec{v} + \nabla \vec{v}^T) - \frac{2}{3} \nabla \cdot \vec{v} I \right] \quad (3.4)$$

where  $\mu$  is the molecular viscosity of the fluid and  $I$  is the unit tensor.

It can be mentioned that in many fluids, viscosity depends only on temperature and not on pressure. The fluids that satisfy Equation 3.4 are called Newtonian fluids. Air and water are some very common examples of Newtonian fluids. Other examples are the cryogenic fluids, namely nitrogen and oxygen that were investigated in the present work. Non-Newtonian fluid examples are polymers and blood.

The set of Navier-Stokes and energy conservation equations are non-linear, partial, second-order differential equations that describe accurately the motion of bodies of fluid. For turbulent flows, the direct numerical resolution of the Navier-Stokes equations is extremely computationally demanding as the spatial and temporal discretization requirements are high. The computational cost for direct numerical simulations

(DNS) is increasing proportionally to the cube of the turbulent Reynolds number of the flow ( $\propto Re_t^3$ ) rendering this approach viable only for small-scale research purposes and practically impossible for industrial scale engineering applications. Lower computational cost alternatives to DNS, are the unsteady Reynolds-averaged Navier-Stokes (URANS) framework, the large eddy simulations (LES), as well as combinations or variations of those two approaches like the detached eddy simulations (DES), all of which are presented in this chapter.

### 3.1.1 Unsteady Reynolds-averaged Navier-Stokes

For practical engineering applications, in order to keep the computer processing and memory needs at an acceptable level, turbulent flows are very often modelled by the URANS equations. Those equations are based on the Reynolds decomposition where a quantity  $A(\vec{x}, t)$  can be decomposed into a mean value  $\bar{A}$ , that is called Reynolds average, and a fluctuation  $A'$ . Reynolds decomposition is described in equations [Equation 3.5](#) and [Equation 3.6](#) [86].

$$A = \bar{A} + A' \quad (3.5)$$

$$\bar{A}(\vec{x}, t) = \frac{1}{T} \int_{-T/2}^{T/2} A(\vec{x}, t + \tau) d\tau \quad (3.6)$$

where  $T$  is an amount of time larger than the time scale of the turbulent fluctuations, but smaller than the time scales of other flow features. Except for the use of Reynolds average,  $\bar{A}$ , the density-weighted mean or Favre average,  $\tilde{A}$ , is also used in order to avoid products of fluctuations of density and other quantities and is presented in [Equation 3.7](#).

$$\tilde{A} = \overline{\rho A} / \bar{\rho} \quad (3.7)$$

The fluctuation of the Favre average is presented in [Equation 3.8](#).

$$A'' = A - \tilde{A} \quad (3.8)$$

Applying the Reynolds and Favre average in equations [3.1](#) and [3.2](#) the mean of the mass conservation equation gives [Equation 3.9](#).

$$\frac{\partial \bar{\rho}}{\partial t} + \nabla \cdot (\bar{\rho} \vec{v}) = S_m \quad (3.9)$$

The momentum conservation equation gives [Equation 3.10](#).

$$\frac{\partial}{\partial t} (\bar{\rho} \vec{v}) + \nabla \cdot (\bar{\rho} \vec{v} \vec{v}) = -\nabla p + \bar{\sigma}^v + \bar{\sigma}^r + S_f \quad (3.10)$$

where  $\bar{\sigma}^v$  is the viscous stress, ([Equation 3.11](#)),

$$\bar{\sigma}^v = 2(\overline{\mu \bar{s}} - \frac{1}{3} \overline{\mu (\nabla \cdot \vec{v})}) I \quad (3.11)$$

and  $\bar{\sigma}^r$  is the Reynolds stress, ([Equation 3.12](#)),

$$\bar{\sigma}^r = -\overline{\rho \vec{v}'' \vec{v}''} \quad (3.12)$$

Reynolds stress is usually much larger than the value of viscous stress and it can be related to the mean velocity field with [Equation 3.13](#) that is called the Boussinesq hypothesis or the Boussinesq eddy viscosity assumption since it assumes that momentum transfer caused by turbulent eddies can be modelled with the introduction of eddy viscosity,  $\mu_t$ .

$$\bar{\sigma}^r = -\mu_t (\nabla \tilde{v} + (\nabla \tilde{v}^T)) + \frac{1}{3} \overline{\rho \vec{v} \vec{v}} I \quad (3.13)$$

In order to be able to use the URANS equations, turbulent viscosity must be modelled and the Reynolds stress,  $\bar{\sigma}^r$ , must be expressed in terms of known mean quantities. The correlations needed to complete the system of equations are provided by turbulence models. In the broadly adopted one- and two-equations models, eddy viscosity is calculated based on turbulence kinetic energy,  $k$ , and either the turbulent dissipation,  $\epsilon$ , or the specific dissipation,  $\omega$ . In the present work, in the context of URANS simulations, the  $k - \omega$  Shear Stress Transport (SST) model has been utilized. The specific turbulence model is found to perform well in highly turbulent wall-bounded flows. More specifically, the SST formulation exhibits a  $k - \epsilon$  behaviour in the free-stream without excessive turbulence production in regions of recirculation [\[87\]](#) and is suitable for adverse pressure gradients [\[88\]](#) that are found in the cases on interest.

### 3.1.2 Large eddy simulation

Since turbulent flows are characterized by eddies of a wide range of length and time scales, the basic idea of Large Eddy Simulation (LES) lies in decomposing the quantities which describe the flow, i.e. velocity, pressure, body forces etc., into two parts. One part includes the larger flow structures, characterised by larger sizes and lower frequencies and the other part includes the remaining smaller scales of higher frequency. The definition between “large” and “small” scales is implemented with the use of appropriate filter functions with filter width  $\delta$ . Based on the filter width,  $\delta$ , the larger flow structures (large eddies), which can be comparable in size to the characteristic length of the mean flow, are resolved directly, while smaller scales, which contribute to the dissipation of turbulence kinetic energy are modelled. Therefore, in terms of the fraction of the scales that are being resolved, LES lies between DNS and URANS.

### 3.1.3 Detached eddy simulation

The detached eddy simulation (DES) models are hybrid models that combine the URANS simulations and the LES approach with the purpose of keeping the computational cost lower than that of LES, but higher than URANS simulations. In this approach, there is a differentiation of the flow treatment depending on the geometry. Near the walls, at the boundary layer region, the URANS models are employed and turbulence is resolved with the use of respective turbulence models. Further away from wall locations, where large turbulent formations are prevailing, the LES employed and the appropriate subgrid-scale models are used.

## 3.2 Pressure and density based solvers

In the context of flow solvers, pressure-based solvers were developed initially for the solution of incompressible, low-mach-number flows [89]. They were later developed further and, by manipulating the pressure equation from an elliptic form to a hyperbolic form [90, 91, 92], pressure-based solvers were able to solve compressible flows extending from subsonic to transonic and supersonic regimes [93, 94]. Density-based solvers were initially developed to cover the needs of the aeronautics industry for the solution of compressible flows [95, 96, 97, 98]. With further development and with the application of various pre-conditioning techniques, density-based methods can be used for solving a wide range of flow conditions including low Mach number and incompressible flows

[99]. In both pressure- and density-based methods the velocity field is computed from the momentum equations. In density-based solvers, the density field is computed from the continuity equation and then the pressure field is determined from the equation of state. In pressure-based solvers, the pressure field is computed by solving a pressure or pressure correction equation that is derived from the combination of the continuity and momentum equations. The density field is then determined from the equation of state [100]. A difference between the two methods can be found in the numerical approach used for the time linearization of the conservation equations [101, 102, 103] but both pressure- and density-based solvers can be used for flows exhibiting a wide range of Mach numbers [104].

To perform the numerical calculations presented in this work, two types of numerical solvers have been utilized. The first solver type is a coupled pressure-based solver. The solver was used within the framework of ANSYS Fluent software. For the pressure-based solver, a two-phase mixture approach was implemented. Mechanical equilibrium, i.e. a common velocity field, was assumed for the two phases. Apart from the mass, momentum and energy conservation equations, an additional transport equation for the vapour volume fraction was solved. The mass transfer model that was implemented is described in paragraph 3.4. Second-order accurate numerical schemes were employed for the discretisation of the governing equations. More specifically, the QUICK scheme was employed for the discretisation of the vapour-fraction equation, a second-order upwind scheme was used for density interpolation, as well as for the discretisation of the momentum and turbulence transport equations and an implicit second-order backward differencing technique was used for time integration.

The second type of solver that has been used in the present work, is an explicit density-based solver. The density-based solver was used within the framework of OpenFOAM open-source software and was based on the explicit density-based solver which is called rhoCentralFoam. RhoCentralFoam is a transient, compressible, single-fluid solver based on the central-upwind flux schemes of Kurganov and Tadmor. Based on previous work by Kyriazis et al. [105], the development of the code for the implementation of the homogeneous equilibrium model to cryogenic flows was part of the work that took place for this thesis. Regarding phase-change, in essence, an infinite phase-change rate was assumed at the bubble interface, i.e. thermodynamic equilibrium was considered and the interphase temperature was taken as equal to the local cell temperature, as calculated by the solution of the energy equation. In this approach, the 3-D URANS equations in conservative form with the addition of mass fraction transport equation are solved (Equation 3.14).

$$\frac{\partial \vec{U}}{\partial t} + \frac{\partial \bar{F}_k(U)}{\partial x_k} = \frac{\partial \bar{F}_k^V(U, \nabla U)}{\partial x_k}, k = 1, 2, 3 \quad (3.14)$$

where  $\vec{U} = [\rho \ \rho Y_g \ \rho v_1 \ \rho v_2 \ \rho v_3 \ \rho E]^T$  is the conservative variables solution vector,  $\rho$  is the density of the mixture,  $\rho Y_g$  is the mass fraction of the gas phase and  $\rho U$  is the momentum of the mixture. The convective flux tensor  $\bar{F}_k = [F_1 \ F_2 \ F_3]$  is presented in [Equation 3.15](#).

$$F_1 = \begin{bmatrix} \rho v_1 \\ \rho Y_g v_1 \\ \rho v_1^2 + p \\ \rho v_1 v_2 \\ \rho v_1 v_3 \\ (\rho E + p) v_1 \end{bmatrix}, \quad F_2 = \begin{bmatrix} \rho v_2 \\ \rho Y_g v_2 \\ \rho v_2 v_1 \\ \rho v_2^2 + p \\ \rho v_2 v_3 \\ (\rho E + p) v_2 \end{bmatrix}, \quad F_3 = \begin{bmatrix} \rho v_3 \\ \rho Y_g v_3 \\ \rho v_3 v_1 \\ \rho v_3 v_2 \\ \rho v_3^2 + p \\ (\rho E + p) v_3 \end{bmatrix} \quad (3.15)$$

The viscous flux tensor  $\bar{F}_k^V = [F_1^V \ F_2^V \ F_3^V]$  is described by [Equation 3.16](#).

$$F_1^V = \begin{bmatrix} 0 \\ 0 \\ \tau_{11} \\ \tau_{12} \\ \tau_{13} \\ v_k \tau_{1k} + q_1 \end{bmatrix}, \quad F_2^V = \begin{bmatrix} 0 \\ 0 \\ \tau_{21} \\ \tau_{22} \\ \tau_{23} \\ v_k \tau_{2k} + q_2 \end{bmatrix}, \quad F_3^V = \begin{bmatrix} 0 \\ 0 \\ \tau_{31} \\ \tau_{32} \\ \tau_{33} \\ v_k \tau_{3k} + q_3 \end{bmatrix}, \quad k = 1, 2, 3 \quad (3.16)$$

where the viscous stress tensor is given by [Equation 3.17](#).

$$\bar{\tau} = 2\mu \left[ \bar{s} - \frac{1}{3} \nabla \cdot \vec{v} I \right] \quad (3.17)$$

Due to the fact that the resulting Mach number values for the conditions of interest for the present work are expected to vary by up to four orders of magnitude, a Mach-

number consistent numerical flux scheme was implemented. The flux scheme followed the work of Schmidt et al. [106] and the proposed Mach-consistent numerical flux, based on the HLLC and the AUSM fluxes [107]. Regarding time discretization, a low storage, four-stage Runge-Kutta method, of 4th order of accuracy in time has been selected [108]. For a solution vector,  $U$ , that is a function of  $\vec{R}$ , which is a function of time,  $t$ , and for which Equation 3.18 is true, the time advancement from a time step (n) to the next (n+1), is described in Equation 3.19.

$$\frac{\partial \vec{U}}{\partial t} = \vec{R}(t, \vec{U}), \quad \vec{U}(t_0) = \vec{U}_0 \quad (3.18)$$

$$\vec{U}^{n+1} = \vec{U}^n + \Delta t \left[ \frac{\vec{k}_1}{6} + \frac{\vec{k}_2}{3} + \frac{\vec{k}_3}{3} + \frac{\vec{k}_4}{6} \right] \quad (3.19)$$

where  $\vec{k}_1$  to  $\vec{k}_4$  are the solutions of the four intermediate stages that need to be stored and are presented in equations 3.20 to 3.23.

$$\vec{k}_1 = \vec{R}(t^n, \vec{U}^n), \quad (3.20)$$

$$\vec{k}_2 = \vec{R}\left(t^n + \frac{\Delta t}{2}, \vec{U}^n + \frac{\Delta t}{2} \vec{k}_1\right), \quad (3.21)$$

$$\vec{k}_3 = \vec{R}\left(t^n + \frac{\Delta t}{2}, \vec{U}^n + \frac{\Delta t}{2} \vec{k}_2\right), \quad (3.22)$$

$$\vec{k}_4 = \vec{R}(t^n + \Delta t, \vec{U}^n + \Delta t \vec{k}_3) \quad (3.23)$$

### 3.3 Equations of state

For the system of differential equations described in Paragraph 3.1 to be complete, an equation or a set of data e.g. a thermodynamic table, describing the relationship between the density of the fluid and the basic flow variables, namely pressure and temperature, must be provided. For flows of Mach number  $M < 0.1$ , compressibility effects can be ignored and the assumption of incompressible fluid can be valid. Density can then be described as constant or solely as a function of temperature. In the present work where e.g. cases of two-phase expansion are investigated, compressibility effects cannot be ignored as the flow can reach supersonic velocities  $M > 1$  and therefore the appropriate equations of state have been used.

One of the equations of state utilized to describe the density of the gas phase is that of the compressible ideal gas. It is based on the ideal gas law and can provide

accurate results depending on operating conditions. The density can be calculated as described by Equation 3.24.

$$\rho = \frac{p}{R_g T} \quad (3.24)$$

where  $R_g$  is the gas constant of the operating fluid.

Regarding the compressibility treatment of the liquid phase, one of the used approaches is the Tait equation of state. The relationship between density and pressure under constant temperature is non-linear and can be expressed as:

$$\left(\frac{\rho}{\rho_0}\right)^n = \frac{K}{K_0} \quad (3.25)$$

where  $K = K_0 + n\Delta p$ ,

$\Delta p = p - p_0$ ,

$\rho_{r,min} < \frac{\rho}{\rho_0} < \rho_{r,max}$ ,

$p_0$  is the reference value of absolute pressure of the liquid,

$\rho_0$  is the density value of the liquid at reference pressure  $p_0$ ,

$K_0$  is the bulk modulus of the liquid at reference pressure  $p_0$ ,

$n$  is the density exponent,

$p$  is the absolute pressure of the liquid phase,

$\rho$  is the density of the liquid phase at pressure  $p$ ,

$K$  is the bulk modulus at pressure  $p$ ,

$\rho_{r,min}$  is the minimum density ratio limit for  $p < p_0$ ,

$\rho_{r,max}$  is the maximum density ratio limit for  $p > p_0$  and

$c = \sqrt{(K/\rho)}$  is the speed of sound in the liquid.

### 3.3.1 Helmholtz energy equation of state

Equations of state based on the dimensionless Helmholtz energy,  $\alpha = A/RT$ , can be used to describe the thermodynamic properties of pure fluids for a wide range of temperatures and pressures. With accurate experimental measurements, precise equations of state can be deduced and all thermodynamic properties of a pure fluid or a mixture can be calculated over the entire thermodynamic space.

For pure fluids, the structure of the dimensionless Helmholtz energy equation of state is described by [Equation 3.26](#).

$$\frac{A}{RT} = \alpha(\tau, \delta) = \alpha^0(\tau, \delta) + \alpha^r(\tau, \delta) \quad (3.26)$$

where  $A$  is the molar Helmholtz energy and  $R$  is the universal gas constant. The dimensionless Helmholtz energy,  $\alpha$ , is expressed as a function of two variables, the dimensionless temperature  $\tau = T_n/T$  and the dimensionless density  $\delta = \rho/\rho_n = V_n/V$ . For the reducing parameters  $T_n$  and  $V_n$  it is common to use the measured critical properties of the pure fluid. [Equation 3.26](#) has been split into two parts that contribute to the sum. The ideal part,  $\alpha^0$ , and the residual part  $\alpha^r$ . Each part's contribution is described in [Equation 3.27](#) and [Equation 3.28](#) respectively.

$$\alpha^0(\tau, \delta) = \ln \delta + c_1 \ln \tau + \sum_{k=2}^{k_1} c_k \tau^{m_k} + \sum_{k=k_1+1}^{k_2} c_k \ln [1 - \exp(-\alpha_k \tau)] \quad (3.27)$$

$$\alpha^r(\tau, \delta) = \sum_{k=k_2+1}^{k_3} c_k \delta^{n_k} \tau^{m_k} + \sum_{k=k_3+1}^{k_4} c_k \delta^{n_k} \tau^{m_k} \exp(-\delta^{e_k}) \quad (3.28)$$

By defining the coefficients  $c_k$  for pure fluids, all needed thermodynamic properties can then be calculated as described in the work of Setzmann and Wagner [109]. For mixtures of pure fluids the process is extended and resulting to a complete model that can be used to calculate all the mixture's thermodynamic properties needed for numerical calculations, namely the real gas compressibility factor,  $Z$ , the component's  $i$  fugacity,  $f_i$ , internal energy,  $E$ , enthalpy,  $H$ , entropy,  $S$ , isochoric heat capacity,  $C_v$ , isobaric heat capacity,  $C_p$ , and the speed of sound of the mixture,  $c$  [110]. Saturation conditions are identified by using the Maxwell criterion.

### 3.3.2 Thermodynamic data tabulation

To implement the Helmholtz equation of state to a density-based numerical solver, all the needed thermodynamic properties must be calculated at each time step and for each cell. Those properties are expressed by the EOS as functions of temperature,  $T$ , and density,  $\rho$ . Since the developed density-based flow solver operates with the conservative variables  $\rho$  and  $\rho E$  a variable transformation would be needed that would call for the use of a numerical root-finding method. This step would result in an extremely high computational load. To override this load, the creation of a complete

thermodynamic table of properties of the fluid of interest and for the needed range of density and temperature conditions is proposed. The proposed table is the result of the calculation of dimensionless Helmholtz energy for a specific fluid and for a specific, but wide, range of conditions. The table is then organized with constant pressure and temperature increments. The thermodynamic table includes all the numerically needed thermodynamic properties. The process of tabulating the thermodynamic tables for Oxygen and Nitrogen was part of the work that took place during this thesis. More specifically, the created tables are expressed as a rectangular structured  $\rho - e$  mesh format, at fixed intervals of density (or density logarithm) and internal energy. The columns of the table are included the needed thermodynamic properties, namely density logarithm,  $\log_{10}(\rho)$ , density,  $\rho$ , internal energy,  $e$ , pressure,  $p$ , temperature,  $T$ , enthalpy,  $h$ , entropy,  $s$ , isobaric heat capacity,  $C_p$ , speed of sound,  $c$ , thermal conductivity,  $k$ , dynamic viscosity,  $\mu$ , and vapour volume fraction,  $v_f$ , all expressed in SI.

### 3.4 Mass transfer models

Within the work frame of the coupled, pressure-based solver, in order to account for the flash-boiling phase-change phenomenon, a two-phase mixture model was employed. The set of governing conservation equations for the mixture was complemented by an advection equation for the conservation of the vapour phase volume fraction (Equation 3.29).

$$\frac{\partial (\alpha_v \rho_v)}{\partial t} + \nabla (\alpha_v \rho_v \vec{v}) = \dot{R} \quad (3.29)$$

where  $\dot{R}$  corresponds to flash vaporization phase-change rate. For all numerical calculations conducted in this study, using a pressure-based solver, the evaporation rate was calculated from the Hertz-Knudsen equation derived from the kinetic theory of gases [52] and is presented in Equation 3.30. The development of the code for the implementation of the Hertz-Knudsen model was part of the work that took place for this thesis.

$$\dot{R} = \frac{\lambda A_{int} (p_{sat} - p)}{\sqrt{2\pi R_g T_{int}}}, \quad A_{int} = n * 4\pi r^2 \quad (3.30)$$

where  $R_g$  and  $T_{int}$  are the ideal-gas constant and the bubble-interphase temperature respectively.  $A_{int}$  is the overall vapour interface surface area, which is calculated assuming a nucleation-site density  $n$  (sites/m<sup>3</sup>) and a bubble radius of  $r = 10^{-6}m$ , a

value that has been deemed as representative of flashing-flows in different benchmark geometries. The nucleation site density was calibrated for each set of boundary conditions. Since a mixture model is employed, the interphase temperature is taken as equal to the local grid cell temperature provided by the solution of the energy equation. The value of the accommodation coefficient  $\lambda$  reflects the degree of deviation from thermodynamic equilibrium. Values approaching unity correspond to conditions approaching thermodynamic equilibrium while values closer to zero suggest deviation from equilibrium. The capability of the Knudsen-based mass-transfer model to capture the phase-change rate in flashing flows has been demonstrated in [4] and has also been implemented in CFD software [111] in order to investigate flash boiling in gasoline fuel injector nozzles. Finally, thermal non-equilibrium modelling has been implemented with multicomponent fuel droplets with good results [112].

### 3.5 Examined cases, boundary conditions and fluid properties

The physical properties of the fluids Iso-octane, Nitrogen and Oxygen that have been simulated in the present work are presented in Table 3.1.

**Table 3.1:** Physical properties of Iso-octane, Nitrogen and Oxygen [9].

Physical property	Iso-Octane	Nitrogen	Oxygen
Molecular mass [ $gmol^{-1}$ ]	114.2285	28.0134	31.9988
Critical temperature [ $K$ ]	543.9	126.19	154.58
Critical pressure [ $bar$ ]	25.7	33.978	50.43
Critical density [ $mol liter^{-1}$ ]	2.14	11.18	13.60
Triple point temperature [ $K$ ]	165.3	63.14	54.33
Normal boiling point [ $K$ ]	372.4	77.34	90.20

For evaluating the saturation pressure of examined fluids as a function of temperature, the Antoine equation, Equation 3.31 has been utilised.

$$\log_{10}(p) = A - \left( \frac{B}{T + C} \right) \quad (3.31)$$

where  $p$  is the vapour pressure expressed in  $bar$  and  $T$  is the temperature expressed in  $Kelvin$ . Parameters  $A, B$  and  $C$  for all fluids of interest are presented in Table 3.2.

**Table 3.2:** Antoine equation parameters of Iso-octane, Nitrogen and Oxygen [9].

Fluid	Temperature validity range [K]	A	B	C
Iso-octane	194.64 - 298.44	3.94736	1282.332	-48.444
Nitrogen	63.14 - 126.	3.7362	264.651	-6.788
Oxygen	54.36 - 154.33	3.9523	340.024	-4.144

The various cases that have been numerically examined, are presented in [Table 3.3](#) along with the basic boundary conditions information. Cases 1 to 3 are presented in [Chapter 4](#), Cases 4 to 13 are presented in [Chapter 5](#) and Case 14 is presented in [Chapter 6](#).

**Table 3.3:** Complete list of fluids and boundary conditions examined in this work.

Case	Fluid	$p_{in} \cdot 10^5$ [Pa]	$p_{out}$ [Pa]	$T_{in}$ [K]	Superheat $R_p$ [-]
1		11.4	2.6	115.3	-
2	LOx	43.0	10.0	93.6	-
3		133.0	124.2	93.6	-
4		17	20600	113.0	33
5	LOx	17	14140	113.0	48
6		17	9100	113.0	74
7		17	2750	113.0	245
8		8	58020	82.5	3
9		8	24870	82.5	7
10	LN <sub>2</sub>	8	6130	82.5	28.4
11		4	58020	82.5	3
12		4	24870	82.5	7
13		4	3330	82.5	52.3
14	Iso-octane	200	0.5	333	1.158

All test cases presented in [Table 3.3](#) have been simulated using the two solvers described in [Section 3.2](#). However, the main purpose of the comparative evaluation of the produced results is not the comparison of the solvers but the comparison of the different phase change mechanisms that each solver uses. Nevertheless, each of the used

solvers incorporates unique features that are not common for both. Thus, in numerous cases in the next chapters, when appropriate, the distinction between the origin of the results is made using the solver type, instead of the phase change mechanism. An overview of the models, equations of state and approaches incorporated into each solver are presented in [Figure 3.1](#).

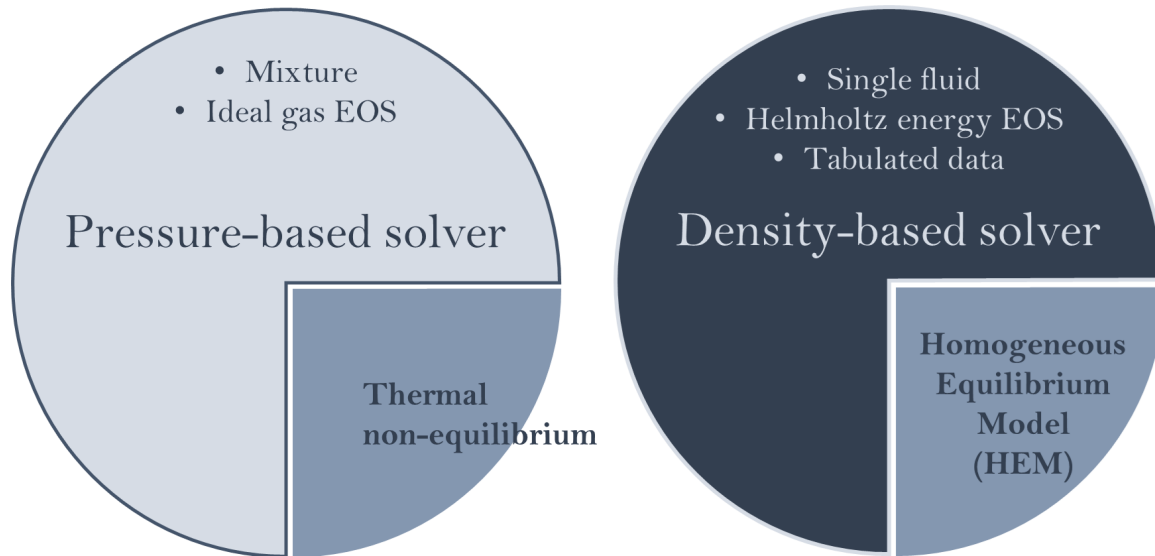


**Figure 3.1:** Overview of the models, equations of state and other approaches that have been incorporated into the pressure- and the density-based solver, which have been used for the production of the results of this work.

# CHAPTER 4

## Modelling of liquid oxygen nozzle flows under subcritical and supercritical pressure conditions

The two-phase flow of liquid oxygen in a converging-diverging nozzle has been numerically predicted at conditions resembling those that prevail in the lower-stage boosters of rocket engines realising lift-off, as well as in the respective upper stages operating in sub-atmospheric pressure conditions. A comparative evaluation of two phase-change approaches has been performed. A model that assumes thermal non-equilibrium was implemented with the use of a pressure-based solver, whereas a homogeneous equilibrium phase-change model (HEM) was implemented with the use of a density-based solver. The departure from thermodynamic equilibrium during phase change has been taken into account via the implementation of a bubble-dynamics model employing the Hertz-Knudsen equation in the pressure-based solver, whereas thermodynamic equilibrium is adopted in the density-based solver. Tabulated data for the variation of the fluid thermodynamic properties have been derived by the Helmholtz Equation of State (EOS) in a modelling approach universal for both the sub- and supercritical states. This approach has been comparatively assessed in the sub-critical regime against the bubble-dynamics-based model including different EOS for the liquid/vapour phases and against a different tabulated approach based on the NIST dataset for supercritical injection. In terms of flow physics, more severe flow expansion in the diverging part of the nozzle has been detected for subcritical pressures, leading to supersonic flow velocities and significant cooling of the fluid mixture. Complementary Detached Eddy Simulations (DES) have provided detailed insight into the complex expansion phenomena and flow instabilities manifesting on the divergent part of the nozzle for subcritical injection conditions. The comparison of the numerical predictions against available experimental data and analytical solutions demonstrates the suitability of the employed methodologies in describing the evolution of the cryogenic oxygen flow expansion and phase change.

## 4.1 Introduction

Liquid oxygen (LOx) constitutes a widely used propellant in multistage rockets for space launch vehicles. It is characterised as a cryogenic liquid as it remains in this state at temperatures below 90K. The combination of liquid hydrogen/oxygen, as the fuel/oxidiser propellant mixture, has been employed in various launch vehicles developed from the 1960s up to now [113]. For instance, LOx/LH<sub>2</sub> propellants were burned in the main engines of the NASA Space Shuttle, the upper stages of the Ares I crew-launch vehicle, as well as the upper rocket stage (Centaur) of Atlas [114]. The same combination of propellants is also used by ESA in the upper stages of the Ariane 5 launch vehicles [115]. They have also been employed in the 2nd and 3rd stages of Saturn V, the 1st and 2nd stage and the upper stage of the family of Japanese H-II and Indian GSLV satellite-launch rockets, respectively. Modern commercial rockets such as the Falcon and BE-4 currently developed by SpaceX and Blue Origin, respectively, have adopted the use of LOx/LCH<sub>4</sub> as propellants. For lower-stage boosters realising lift-off and thus operating at atmospheric conditions, LOx is usually mixed with kerosene (RP-1), e.g. in the cases of Saturn V, Atlas V, the Russian Soyuz, and SpaceX Falcon rockets.

It is essential to mention that the upper stages of rocket launch vehicles are designed to operate at high altitudes, where near-vacuum conditions ensue. As a general practice, these stages incorporate combustion chambers operating at lower pressures compared to their lower-stage counterparts [116]. Hence, depending on the specific rocket-engine design and its location at the tandem-stage configuration, the delivery of LOx to mix with the main fuel could be realised at either supercritical (lower stages) or subcritical (upper stages) pressure conditions. For reference, the critical point for oxygen corresponds to 50.4 bar/154.6 K [117]. LOx phase change due to rapid pressure drop is expected to occur in the oxidiser-delivery nozzle, especially during engine start-up, where vacuum conditions may exist. The topology and dynamics of the compressible flow will be designated to a great extent by the steepness of the density gradient. In the case that the process evolves at subcritical pressures, the fluid density exhibits an abrupt change, as an interphase sets in between the liquid and vapour phases, i.e. bubbles form. The rapid bubble nucleation within the entire bulk of the liquid due to rapid depressurisation is characterised as flash boiling, a flow phenomenon that is possible to be encountered in cryogenic fluids [118], refrigerants [17] and light hydrocarbons [119]. On the contrary, for supercritical conditions, no interface emerges and the fluid density exhibits a smooth variation with pressure.

Experimental studies focusing on nozzle and spray flows of cryogenic oxygen for

a wide range of flow conditions are relatively limited in the open literature due to the technical difficulties associated with the handling and storage of the substance at cryogenic temperatures and the extreme conditions that the experimental hardware must withstand, especially at supercritical pressures/temperatures [49]. The technical note of Hendricks et al. [5] is one of the early studies made available by NASA reporting measurements of the pressure distribution of two-phase LOx flow within a Venturi nozzle at subcritical pressures. Early studies by Mayer and co-workers [47, 48] utilised different optical methods to pinpoint the differences in the topology of cryogenic-liquid jets being expelled at an environment of either sub- (of the order of 15 bar) or supercritical-pressure conditions (100 bar). The topology and degree of atomization of LOx spray at 10 bars have also been investigated at the Mascotte test bench of ONERA [50]. Cherhoudi et al. [120] conducted backlit-illumination visualisation to illustrate the topology of LOx and LN<sub>2</sub> jets injected into a gaseous environment at conditions ranging from sub- to supercritical pressures and supercritical temperatures. Quantitative data regarding the jet cone angle were obtained and it was verified that the jet growth rate measurements were in agreement with the theoretical predictions for gaseous jets of variable density. More recently, the shadowgraphy visualisation conducted by Lamanna et al. [7] considering subcritical LOx and ethanol sprays at injection pressures up to 17 bar demonstrated that a higher degree of superheat is required for the inception of flash boiling in cryogenic compared to storable propellants. According to the nucleation theory proposed by the same authors in [30], this is due to the higher surface energy work at low temperatures, which must be surpassed by the fluid chemical potential, in order for vapour bubbles to form.

It can be therefore deduced that, due to the complexities associated with experimental campaigns, accurate numerical modelling is crucial for cryogenic-propellant flow applications. At supercritical pressures, the suitability of the modelling approach is highly dependent on the selection of an Equation of State capable of capturing the thermodynamic properties of the fluid at very high pressures and temperatures. A number of studies available in the literature refer to supercritical injection or expanding-nozzle flow of refrigerants like liquid CO<sub>2</sub>. Thermodynamic closure is commonly accomplished through the use of cubic equations of state [121, 122, 123, 124]. It has been verified that the selection of EOS (i.e. Peng-Robinson (PR), Benedict-Webb-Rubin, Span-Wagner) has a considerable impact on the numerical prediction of supersonic CO<sub>2</sub> accelerating flows, as it affects the location and intensity of emerging shockwave patterns [125].

With reference to cryogenic fluids, research on supercritical injection is mainly focused on liquid nitrogen or oxygen as working media. Different subgrid scale (SGS)

models for LES along with volume translation methods for the PR were comparatively evaluated by Müller et al. [126] with regards to liquid nitrogen injection. It was found that the effect of thermodynamics modelling was more profound for the case of transcritical compared to supercritical injection, while the selection of SGS model only had a minor influence on the temporal evolution of the jet mean density. Poormahmoud et al. [127] investigated the dispersion dynamics of LN<sub>2</sub> inside and downstream the outlet of a single-orifice swirl atomiser. The SST  $k$ - $\omega$  and the SRK EOS were employed for turbulence and thermodynamic closure, respectively. The pattern of vortical structures emerging at the diverging part of the flow layout was illustrated along with their transient features. Kang et al. [128] conducted a similar study using the same EOS in an LES framework. Apart from hydrodynamic instabilities, the study also highlighted the acoustic instabilities affecting the flow field. Likewise, supercritical LOx injection has been mainly investigated numerically with reference to swirl atomisers suitable for rocket engines. Zong et al. [129] performed an LES study referring to a LOx swirl injector using the Soave-Redlich-Kwong (SRK) and Benedict-Webb-Robin equations of state for the calculation of the fluid thermodynamic and transport properties, respectively. Kelvin-Helmholtz instabilities were demonstrated to be the primary cause leading to supercritical mixing. Wang et al. [130] employed the modified SRK EOS to describe the thermodynamic properties of LOx during supercritical injection, while in a subsequent study [131] the same approach was followed to illustrate the LOx/kerosene mixing characteristics. Both studies focused on the influence of hydrodynamic instabilities on the propellant dispersion in the expanding geometry downstream of the injector outlet.

Concerning subcritical conditions, jet atomization and the formation of a two-phase spray is the process governing the combustion behaviour of the oxidizer/fuel mixture. In the case that flash-boiling conditions are met, the oxidiser's rapid vaporisation within the injector orifice has a tremendous influence on the characteristics of the expelled spray. Studies on water, refrigerants and light hydrocarbons have demonstrated that in-nozzle flash-boiling leads to the production of finer sprays with higher cone angles and reduced penetration lengths compared to nozzle flows with inertia-driven phase change (i.e. cavitation) [31]. Nevertheless, few numerical studies have been found in the open literature illustrating the distinct features of cryogenic liquid. Travis et al. [132] developed a theoretical two-phase model based on the Helmholtz energy EOS capable of predicting the critical flow rate for choked flows of cryogenic fluids. A correction on the homogeneous equilibrium model was implemented to take into account non-equilibrium effects. The theoretical predictions for different cryogenic

liquids were found to be in good agreement with experimental results for the critical flow rate. Lyras et al. [133] employed the Homogeneous Relaxation Model coupled to the volume-of-fluid method to predict the flashing phase-change in a throttle nozzle and subsequent spray expansion of liquid nitrogen. Schmehl and Steelant [134] used an Eulerian-Lagrangian frame to simulate the pre-flow of di-nitrogen tetroxide (N<sub>2</sub>O<sub>4</sub>) oxidiser in a co-axial flow injector considering a dilute mixture of liquid droplets and vapour. Droplet flash vaporisation was described through an empirical model based on pre-existing measurements. A similar numerical approach was adopted by Ramcke et al. [135] to simulate the spray dynamics of LOx pre-flow and the mixing behaviour of the oxidiser with gaseous methane. Both studies concur that cryogenic flashing sprays exhibit the same distinct features as those of storable liquids, namely enhanced droplet atomisation, increased cone angle and acceleration of the compressible mixture. Gaillard et al. [136] employed two coupled-flow solvers to perform LES of LOx spray atomisation with relevance to the experiments performed at ONERA [50]. The gaseous and dispersed phases were treated in an Eulerian framework, while the Abramzon-Sirignano [137] model was used for evaporation and heat transfer.

The outlined literature overview makes clear that different modelling approaches have been implemented to predict cryogenic-liquid injection in an ad-hoc manner, primarily depending on the thermodynamic regime and specific flow features, e.g. swirling flows. To the authors' knowledge, this is the first work in the open literature to propose and evaluate a modelling framework suitable for the prediction of multiphase, cryogenic wall-bounded flows for a wide range of pressure conditions and capable of reproducing distinct features such as flash vaporisation, supersonic expansion and transition to a supercritical state. The present study constitutes a comparative investigation of the predictive accuracy of different methods regarding in-nozzle phase change in both sub- and supercritical regimes. Furthermore, a universal methodology based on tabulated thermodynamics applicable to both regimes is demonstrated. Previous works of the authors' group ([138, 139]) have demonstrated the robustness of the technique in modelling phase change and spray mixing in fuel-injection applications. The tabulation technique has been extended to cryogenic oxygen in this work, based on the Helmholtz energy EOS for the calculation of thermodynamic properties. Unlike the majority of available studies, the present work focuses mainly on the in-nozzle, compressibility related, flow phenomena and highlights their influence on the spray expansion and dynamics. Further to the Ussimulations performed, hydrodynamic-instability effects have been assessed through DES.

## 4.2 Methodology

Two flow solvers, an implicit coupled pressure/velocity and an explicit density-based, have been employed in the present investigation. The basic set of governing equations solved in both cases comprised the continuity, momentum and energy conservation equations. The complete formulations of the adopted numerical methodologies, along with the sets of equations solved are described in detail by Karathanassis et al. [4] and Kyriazis et al. [105, 140] respectively, with reference to the pressure- and density-based solvers discussed in the following sections.

### 4.2.1 Thermal non-equilibrium assumption

Referring to the subcritical regime, a two-phase mixture approach was implemented in the coupled solver including an additional equation for the vapour transport. On the contrary, a single-fluid approach was adopted for the simulations in the supercritical regime, where the fluid properties for each computational cell were provided by the REFPROP dataset. Numerical schemes with second-order accuracy were employed for the discretisation of the governing equations. The QUICK scheme was employed for the discretisation of the vapour-fraction equation, while a second-order upwind scheme was used for density interpolation, as well as for the discretisation of the momentum and turbulence transport equations. An implicit, second-order backward differencing technique was used for time integration with a time step value of  $10^{-6}$  s, resulting in a CFL criterion value less than 1 in the entire domain for the DES cases examined.

A bubble-dynamics-based model was employed in the coupled solver to capture the phase-change process under subcritical conditions. Mechanical equilibrium, i.e. a common velocity field, was also assumed for the two phases. Liquid LOx compressibility was imposed through the Tait EOS, while the respective vapour phase was treated as an ideal gas. The set of governing equations for the mixture was complemented by an advection equation for the conservation of the vapour phase volume fraction as follows:

$$\frac{\partial(\alpha_v \rho_v)}{\partial t} + \nabla(\alpha_v \rho_v \vec{u}) = \dot{R} \quad (4.1)$$

where the phase-change rate  $\dot{R}$  corresponds to that of flash vaporisation. For the simulations of this study, the rate was calculated from the Hertz-Knudsen equation derived from kinetic theory of gases [141]:

$$\dot{R} = \frac{\lambda A_{int}(p_{sat} - p)}{\sqrt{2\pi R_g T_{int}}} \quad (4.2)$$

where  $R_g$  and  $T_{int}$  are the ideal-gas constant and the bubble-interphase temperature respectively, while  $A_{int}$  is the overall vapour interface surface area, calculated as in [4]. Since a mixture model is employed, the interphase temperature is taken as equal to the local grid cell temperature provided by the solution of the energy equation. The degree of deviation from thermodynamic equilibrium is reflected in the value of the accommodation coefficient  $\lambda$ . Values of either 1.0 or 0.1 correspond to conditions similar to thermodynamic equilibrium and strongly deviating from it, respectively [33]. The capability of the Hertz-Knudsen model in capturing the phase-change rate with reference to flashing flows has been demonstrated in [4]. The model has also been utilised to describe phase-change in both fundamental bubble-dynamics studies [141] and more applied simulations with reference to gasoline fuel injectors [111]. This work demonstrates its applicability with reference to in-nozzle cryogenic flows.

The refrigerants and refrigerant-mixtures database (REFPROP v.9.1) of the National Institute of Standards and Technology (NIST) contains thermodynamic and transport properties for oxygen; the properties provided by REFPROP have been derived using the Helmholtz energy EOS, as described by Schmidt and Wagner in [142]. Further details on the EOS used for the derivation of the fluid's properties can be found in [143, 144]. For test cases corresponding to supercritical pressures, the REFPROP library is dynamically loaded into the coupled solver in the form of a pre-formulated look-up (structured) matrix. Material properties are stored in the matrix as a function of local pressure and temperature. For the present simulations, a  $201 \times 201$  matrix has been formulated with pressure and temperature lying within the ranges  $500.0 \text{ kPa} \leq p \leq 15.5 \text{ MPa}$  and  $56.0 \text{ K} \leq T \leq 156.0 \text{ K}$ , respectively.

### 4.2.2 Thermal equilibrium assumption

The 3-D URANS equations in conservative form were considered in the density-based solver, where a single-fluid modelling approach has been formulated in both the sub- and supercritical regimes. In essence, referring to the subcritical regime, an infinite phase-change rate was assumed at the bubble interface, i.e. establishment of thermodynamic equilibrium, and the entire process was replicated by an appropriate EOS. Since the Mach number is plausible to obtain a wide range of values in the simulated cases, owing to the fluid phase transitions (pure liquid, vapour, two-phase mixture or supercritical fluid), a Mach-number consistent numerical flux has been implemented based on the HLLC and the AUSM fluxes [106, 107]. Conservative variables at cell interfaces, required for the calculation of the fluxes, were determined using the MUSCL-Hancock reconstruction [108], second-order accurate in space. A

fourth-order accurate, four-stage Runge-Kutta method has been selected for time integration, with a CFL criterion of 0.8 imposed for all the simulations performed.

LOx thermodynamic properties required by the density-based solver are derived from the Helmholtz energy EOS, which is calibrated within the temperature range  $54.4 \text{ K} \leq T \leq 2000.0 \text{ K}$ , for maximum pressure and density of  $p_{max}=82.0 \text{ MPa}$  and  $\rho_{max}=1387.1 \text{ kg/m}^3$ , respectively. The properties are organised into a thermodynamic table that may include a narrower range of values, depending on the application. The dimensionless form of the aforementioned EOS for the Helmholtz energy "a", having as independent variables the density and the temperature [110] is:

$$\frac{a(r, T)}{RT} = \alpha(\delta, t) = \alpha^0(\delta, \tau) + \alpha^r(\delta, \tau) \quad (4.3)$$

where  $\delta = \rho/\rho_c$ ,  $\tau = T_c/T$ . From the expanded form of Equation 4.3, where the dimensionless Helmholtz energy of the ideal gas  $\alpha^0$  and the residual Helmholtz energy  $\alpha^r$  can be calculated using the correlations reported by Kyriazis et al. in [105], all the necessary thermodynamic properties (pressure, internal energy, enthalpy and speed of sound) can be obtained, as a function of density and temperature. Saturation conditions are identified by the Maxwell criterion, i.e. the pressure for which the Gibbs free energy of the liquid and vapour phases are equal for a given temperature. The fluid properties within the saturation dome are calculated by the mixture assumption, whereas the mixture speed of sound is determined from the Wallis speed-of-sound formula [142]. Figure 4.1 presents the variation of oxygen pressure (Figure 4.1.a), speed of sound (Figure 4.1.b) and internal energy (Figure 4.1.c) derived with density and temperature, as calculated employing the procedure in mention. The saturation curve in each plot is represented as a black dashed line.

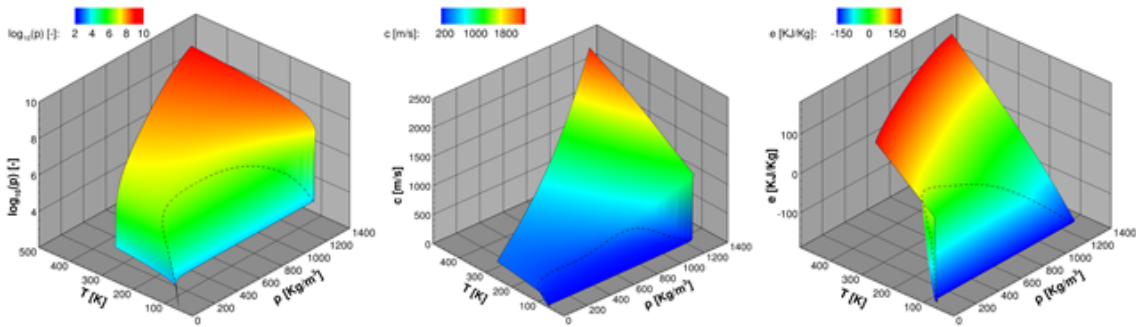


**Figure 4.1:** Three-dimensional phase diagrams for oxygen: (a) pressure, (b) speed of sound and (c) internal energy in terms of density and temperature.

Solving the Helmholtz EOS at each time step would incur considerable computa-

tional cost, as it requires root finding of non-linear equations. Hence, a tabulated-data technique, similar to that proposed in [145] has been implemented. A structured thermodynamic grid of 100,400 elements has been created, containing information for all the thermodynamic properties on each node defined by a density and internal energy value. The density range of the grid is  $0.125 \leq \rho \leq 1263.8 \text{ Kg/m}^3$  divided into 251 points of fixed  $\Delta\rho = 5.055 \text{ kg/m}^3$ , while the internal energy range of the grid is  $-171.14 \leq e \leq 165.51 \text{ kJ/kg}$  divided into 400 points of fixed  $\Delta e = 0.84161 \text{ kJ/kg}$ . Once density and internal energy are calculated by the URANS equations, the corresponding element of the thermodynamic table is identified through numerical inversion from the above quantities. Any thermodynamic property  $\phi$  of the table is then approximated by a finite element bilinear interpolation:

$$\phi(\rho, e) = \sum_n^{\text{nodes}} N_n(\rho, e) b_n \quad (4.4)$$

where  $\phi$  corresponds to pressure, temperature or speed of sound, required for the calculation of the fluxes in the density-based solver. Full details on the shape functions,  $N$ , employed and the calculations of unknowns,  $b$ , on each node  $n$  are reported in [105].

### 4.2.3 Turbulence closure

The Reynolds number characterising the flow has been found to be well within the turbulent regime for all the cases examined, ranging from 0.6 to 2.2m. The nozzle diameter was used as the characteristic length scale for the estimation of the Reynolds number, while an approximation of the velocity was made based on experimental values of the mass flow rate and the properties of the liquid phase at the saturation pressure corresponding to the injection temperature. The  $k-\omega$  Shear Stress Transport (SST) turbulence model was therefore employed to account for contributions on fluid (or mixture) viscosity  $\mu$  and thermal conductivity  $k$  due to turbulence effects. The specific turbulence model has been demonstrated to perform well in both moderately and highly turbulent wall-bounded flows, where secondary flow is also possible to arise [87].

With reference to the DES approach, the delayed detached eddy simulation model (DDES) was incorporated [146], which is formulated to switch between a URANS ( $k-\omega$  SST) and a Large Eddy Simulation (LES) Model, depending on the grid resolution and the local turbulence length scale. Hence, the computational cost can be reduced in regions where the influence of turbulence in the flow field is expected to be minor. On the contrary, the model switches to a Smagorinsky-like subgrid model capable of

resolving turbulent structures in high grid-density regions. It is important to highlight that the DDES formulation prevents grid-induced separation from occurring at regions of grid refinement inside attached boundary layers [147].

#### 4.2.4 Domain discretisation and grid independence

A typical converging-diverging nozzle was selected as the computational domain since experimental data with reference to cryogenic liquids are available in the literature for the specific layout. Since the orifice is axisymmetric, the domain was reduced to a wedge produced by rotating the nozzle layout, depicted in Figure 4.2, around the symmetry axis by 5 degrees. A full 3-D domain representing the entire orifice volume (rotation of 360 degrees) was selected for DES, as the use of truncated domains and the imposition of a symmetry boundary condition was found to induce Coanda-like pseudo-instabilities [148] leading to an asymmetrical flow field at the diverging nozzle part. As also depicted in Figure 4.2, the inflow section has been expanded upstream in both domains to impose the stagnation conditions of the experiment.

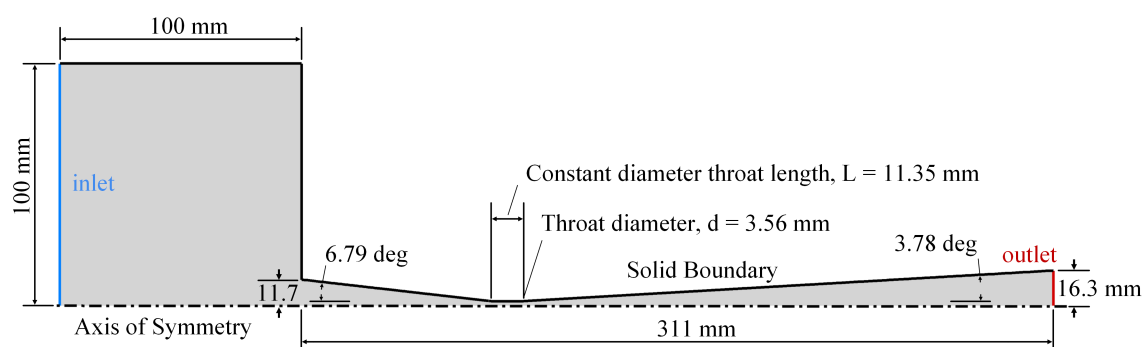


**Figure 4.2:** Geometry of the conical converging-diverging nozzle [5]. The inflow has been expanded upstream in order to impose the stagnation conditions of the experiment.

A test case where severe jet expansion is expected to occur (refer to case 2 of Table 4.2) has been selected to evaluate the effect of grid density on the produced numerical results regarding the URANS simulations with the pressure-based solver being selected to conduct the grid independence study. Figure 4.3 presents the pressure (Figure 4.3.a) and volume vapour fraction (Figure 4.3.b) distributions, at the orifice symmetry axis, as produced by three numerical grids consisting approximately of 37, 60 and  $100 \times 10^3$  cells, respectively. It is evident all three grids can capture the overall flow behaviour. It has been verified that the average discrepancy in the pressure values downstream the throat region between the intermediate and fine grids is of the order of 1.92 %, while the deviations in the vapour fraction values are approximately 0.12

%. Hence, the intermediate grid, the topology of which is depicted in Figure 4.4.a has been considered sufficient and it has been utilised by both solvers.

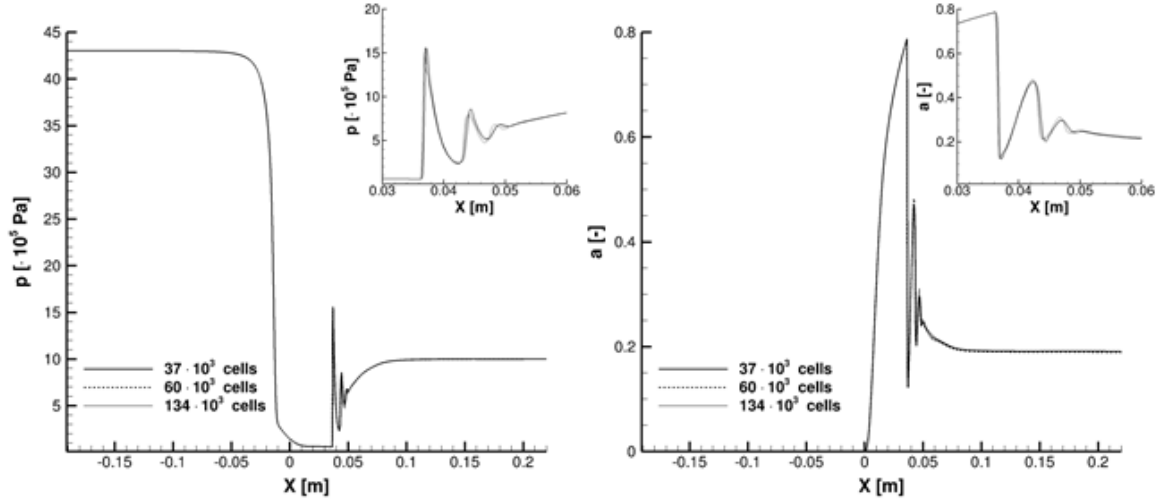


**Figure 4.3:** Grid independence study for URANS simulations: (a) pressure and (b) vapour volume fraction distributions at the orifice symmetry axis for grids of increasing cell count.

As shown in the detailed view of Figure 4.4.a, grid refinement layers were placed in the vicinity of the orifice wall resulting in a maximum  $y^+$  distance of the order of 1.0 in the throat region. A much finer grid compared to the URANS simulations has been utilised for DES. The grid density was designated by the Taylor length scale:

$$\lambda_g = \sqrt{10} Re^{-0.5} L \quad (4.5)$$

where  $L$  is a characteristic length scale, selected as the nozzle throat diameter ( $d_t=3.55$  mm) in the specific case. Inertial turbulent structures larger than the Taylor length scale are resolved through LES, while smaller viscous isotropic scales are modelled. The Taylor length scale for the cases examined lies in the range 50-120  $\mu\text{m}$ .

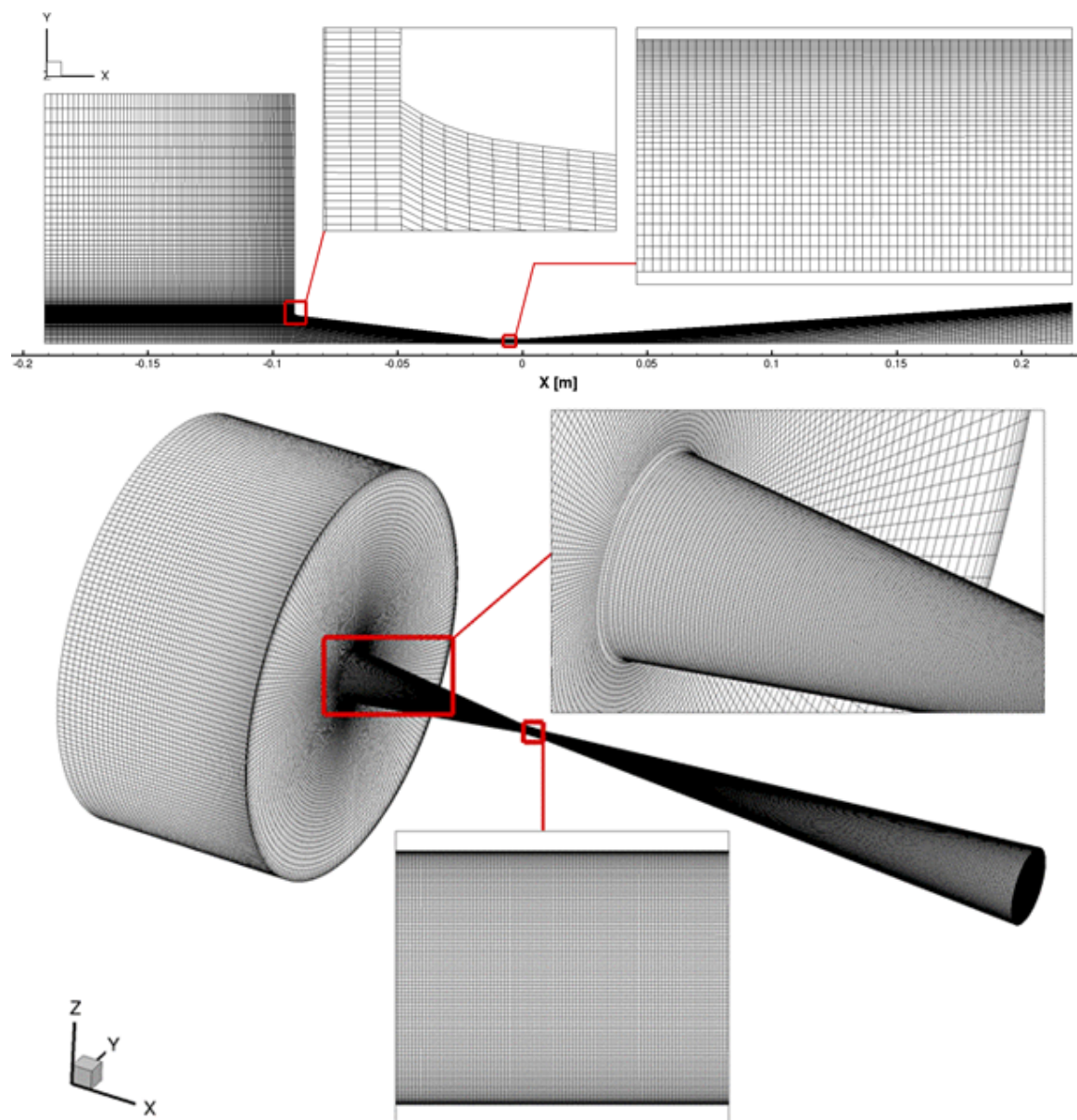


**Figure 4.4:** Computational grid employed for (a) URANS simulations and (b) DES. Detailed views of the nozzle inlet, as well as the nozzle throat region, are presented as insets for both grids.

As depicted in [Figure 4.4.b](#), a structured mesh with gradual refinement at the throat region has been generated for the DES investigation. More specifically, the base resolution level at the upstream and downstream nozzle parts was progressively refined to the lowest value of the Taylor length scale at the throat region. Near-wall refinement was also applied leading to  $y^+$  values of the order of 0.15 in the throat region. The overall cell count of the grid developed for the discretisation of the full  $360^\circ$  domain was approximately equal to  $9.48 \times 10^6$  cells.

### 4.2.5 Boundary and initial conditions

Suitable boundary conditions complemented the governing equations, in order to replicate the physical conditions prevailing during the actual LOx-injection process. Dirichlet-type boundary conditions, i.e. constant static pressure values corresponding to the actual operating conditions were imposed at the domain inlet and outlet for all the cases examined. Furthermore, zero-gradient value was imposed for the boundary-normal velocity component at the inlet, while the rest of the velocity components were set to zero. A no-slip condition was imposed at the nozzle wall. Referring to the energy-conservation equation, constant temperature or internal-energy values were imposed at the domain inlet and outlet for the pressure- and density-based solvers, respectively, owing to the different equation formulations implemented in each solver. The orifice wall was treated as adiabatic. At the outlet boundary, zero-gradient boundary conditions were set to all velocity components and transported quantities. The types of boundary conditions set for the examined cases are summarised in [Table 5.1](#). The specific boundary-condition values of each variable and for each of the examined cases are presented in [Table 4.2](#) of [Section 4.3](#).

The URANS simulations were initialised assuming pure liquid (vapour fraction  $\alpha=0$ ) in the entire domain, while the domain initial pressure and temperature were set equal to the respective inlet values. Quiescent fluid ( $\vec{u}=0$ ) was assumed at the initial time instance. DES cases were initialised using the flow and temperature fields obtained from preliminary runs for the same conditions considering laminar flow of the liquid phase only, so as to provide the perturbations necessary for turbulence structures to develop. The initial conditions set are also summarised in [Table 5.1](#).

**Table 4.1:** Summary of boundary and initial conditions imposed for the numerical simulations.

	Inlet	Outlet	Wall
Pressure-based	$p=p_{in}$ $T=T_{in}$	$p=p_{out}$ $T=T_{out}$	$\vec{u} = 0$ $\partial T/\partial n = 0$
Density-based	$p=p_{in}$ $e=e_{in}$	$p=p_{out}$ $e=e_{out}$	$\vec{u} = 0$ $\partial T/\partial n = 0$
Initialization			
URANS	$\vec{u} = 0$	$T = T_{in}$	$\alpha = 0$
DES	Initialization with single-phase laminar flow		

### 4.3 Results

The test cases examined in this study are summarised in [Table 4.2](#). As can be seen, both sub- and supercritical injection pressures have been considered. More specifically, the pressure and temperature conditions of case 1 were obtained from the experimental campaign of Hendricks et al. [5] for which data regarding the pressure distribution along the orifice are available. The set of boundary conditions of case 2 was chosen as representative of a second-stage engine. Rocket-engine tests with the same outlet/chamber pressure have also been conducted on the Mascotte test bench of ONERA [50]. Finally, the conditions of case 3 were selected to be within the range of operation of the LOx turbopump of the Vulcain-2 engine of Ariane 5 heavy-lift space launch vehicle [149, 150] and higher than the combustion chamber pressure [115], while maintaining the same pressure difference as in case 1.

The rationale for deciding on the specific test cases was to pinpoint the significant variation in expansion dynamics between sub- and supercritical pressure injection despite the similarity in macroscopic flow parameters. Simulations for all cases were performed with the use of transient solvers, yet it was confirmed that the respective flow and temperature fields reached steady-state solutions in most cases.

**Table 4.2:** Matrix of test cases examined. It must be noted that temperature lies in the subcritical regime for all cases.

Case	$p_{in} \times 10^5 [Pa]$	$p_{out} \times 10^5 [Pa]$	$T_{in} [K]$	$e_{in} \times 10^3 [m^2 kg s^{-2}]$	Pressure regime	Phase-change model
1	11.4	2.6	115.3	-361.01	Subcritical	Helmholtz EOS / Hertz- Knudsen
2	43.0	10.0	93.6	-400.44	Subcritical	Helmholtz EOS / Hertz- Knudsen
3	133.0	124.2	93.6	-403.29	Supercritical	Helmholtz EOS / NIST

### 4.3.1 Code validation

The pressure-based solver employing the Hertz-Knudsen phase-change model has been extensively validated with reference to internally and externally flashing flows considering water as the working medium in a previous work of the authors' group [4]. More specifically, the model has been demonstrated to accurately capture phase-change in a converging-diverging nozzle similar to the one of the present study, a (throttle) nozzle with an abrupt contraction and a rapidly depressurising duct (pipe blow-down). To further demonstrate the accuracy of the Hertz-Knudsen model, additional simulations have been performed for the geometry described in Figure 4.2 and the numerical predictions for LOx mass flow rate are compared in Table 4.3 against experimental data available from [5]. As can be seen, good agreement between the numerical and experimental data is achieved for a wide range of conditions in the subcritical regime.

Furthermore, the density-based algorithm has been validated in previous works with reference to bubble- [105], and droplet-dynamics [151] simulations, while the accuracy of the tabulated technique based on Helmholtz energy EOS has been verified with reference to the properties of n-dodecane [105]. An additional validation study has been set up in order to further evaluate the capability of the density-based solver with the Helmholtz EOS thermodynamic closure to capture wall-bounded LOx flows. A computational domain corresponding to a reference converging-diverging nozzle of circular cross section was realised and the numerical results were compared against a 1-D HLLC solver for the Euler equations considering an EOS of the form

**Table 4.3:** Comparison between experimental and numerical results. The Hertz-Knudsen model was utilised for the flow simulations.

Boundary conditions			Experimental	Numerical	Deviation
$p_{in} \times 10^5 [Pa]$	$p_{out} \times 10^5 [Pa]$	$T_{in} [K]$	$\dot{m}_{exp} [kg s^{-1}]$	$\dot{m} [kg s^{-1}]$	from $\dot{m}_{exp}$
49.2	7.1	134.0	0.669	0.677	1.25%
38.9	6.1	134.2	0.542	0.541	-0.17%
25.1	3.6	116.1	0.541	0.560	3.58%

$p = f(\rho, e)$ , which can be provided in either analytically [108] or in a tabular form [105]. The orifice cross-sectional area  $S$  varies with its length  $L$  according to the relation  $S(L) = 0.01L^2 + 0.01$  for  $L \in [-2, 2]m$ . A 5 ° wedge of the geometry was considered as the computational domain, discretised by a structured grid of 5200 cells. The cell size was uniform and equal to 10.0 mm along the longitudinal direction, while it varied between approximately 0.9 mm (throat region) and 4.3 mm (upstream and downstream parts) along the radial direction. The density and temperature at the domain inlet were set equal to  $\rho_{in}=817.07 \text{ Kg/m}^3$  and  $T=143 \text{ K}$ , respectively, which will lead to an inlet pressure of  $53.87 \times 10^5 Pa$ , while the outlet pressure was set to  $16.35 \times 10^5 Pa$ . As made evident by Figure 4.5, the obtained numerical solution and the reference 1-D solution are in excellent agreement regarding all the plotted quantities. Due to subsonic flow conditions in the entrance, the flow accelerates in the converging part (Figure 4.5.a). The expansion of the two-phase jet leads to further acceleration and transition to supersonic velocities (Figure 4.5.b), while the supersonic region is extended until the exit of the orifice without the manifestation of a shockwave system, as made clear by the pressure distribution of Figure 4.5.c. Almost full liquid vaporisation has occurred by the outlet location, as depicted in Figure 4.5.d. It has to be noted that, apart from this initial validation study, further comparisons of the numerical results have been conducted against available experimental data, as discussed in the following section.

Finally, the accuracy of the employed pressured-based solver using the REFPROP database to replicate phase change in the supercritical regime has been verified against the quantitative measurements of Mayer et al. [6] for a  $N_2$  jet, since quantitative data on supercritical LOx could not be obtained from the open literature. The jet

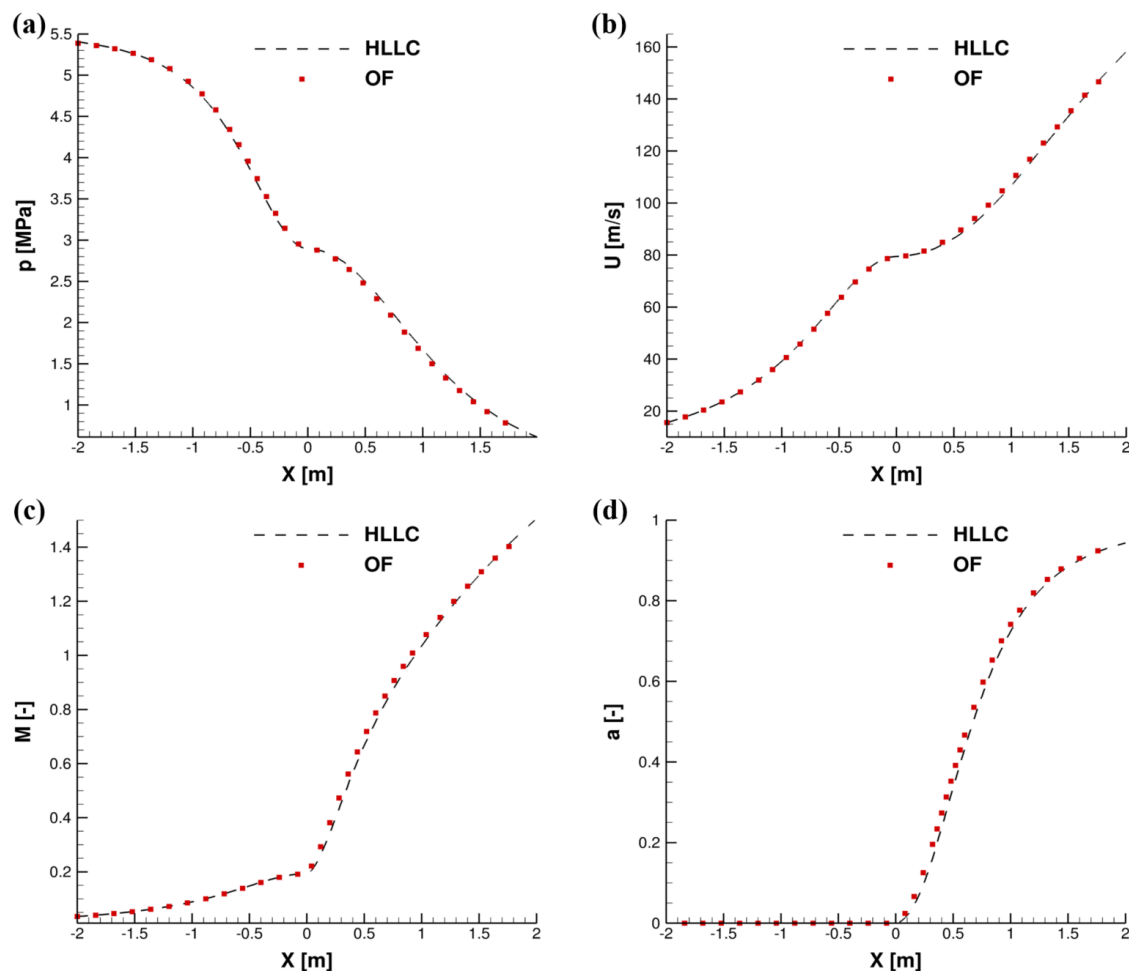


**Figure 4.5:** Validation of the density-based solver (OF) for the converging-diverging nozzle case: Numerical results for (a) pressure, (b) velocity magnitude, (c) Mach number (d) vapour volume-fraction distributions along the orifice symmetry line and comparison against the predictions of the 1-D solver (HLLC).

enters at a velocity of 5.4 m/s a chamber where supercritical pressure (3.98 MPa) and temperature (137 K) conditions persist. The Reynolds number characterising the injection is equal to  $1.53 \times 10^5$ . Figure 4.6 depicts the average density distribution along the jet axis obtained through 3D LES, while the averaged density field is presented in the figure inset. It is demonstrated that very good agreement is achieved between numerical and experimental results.

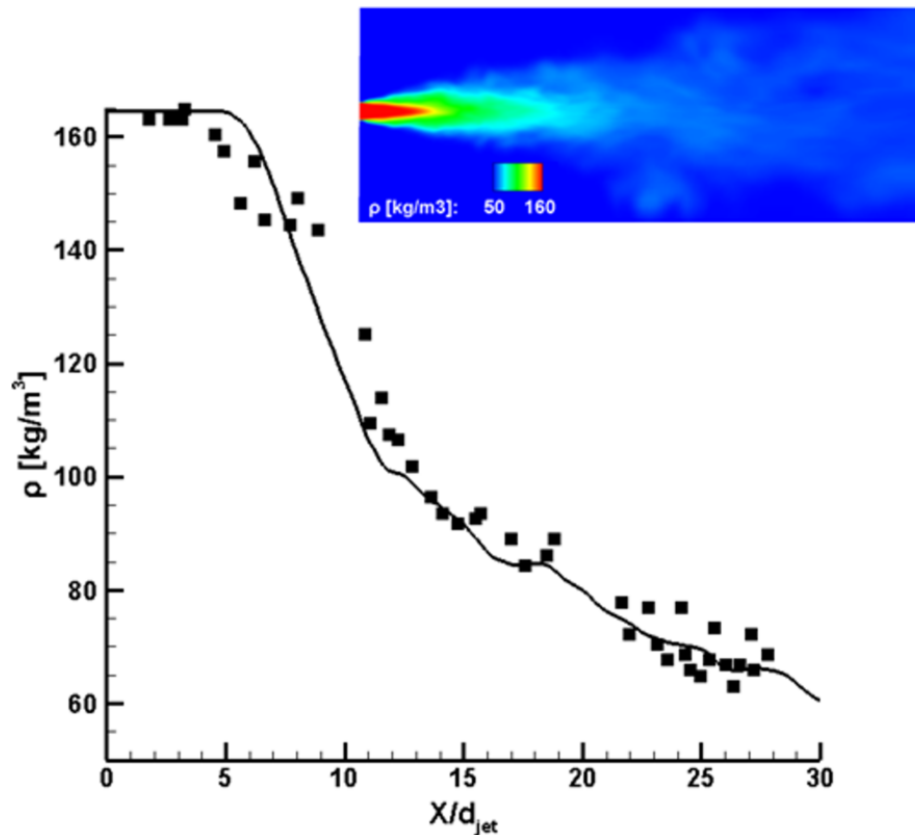


**Figure 4.6:** Validation of the pressure-based solver using NIST-REFPROP database: Comparison of numerical predictions of the average N<sub>2</sub>-jet density distribution at the jet axis (solid line) against experimental data (symbols) [6]. The average density contour plot is depicted in the inset.

### 4.3.2 Simulations in the subcritical regime

The numerical results corresponding to cases 1 and 2 of Table 4.2 are discussed in this section. Figure 4.7 illustrates the distinct flow features as predicted by the two solvers for case 1. The rapid fluid pressure drop in the throat region and downstream is clearly shown in the contour plots of Figure 4.7.a. It must be noted that the top and bottom frames correspond to the predictions of the thermal non-equilibrium phase-change model and the HEM, respectively. A pressure minimum is reached at the orifice diverging part followed by the manifestation of a shock wave. The pressure re-develops to its outlet value further downstream. As shown in Figure 4.7.b, the flow accelerates in the converging part, nevertheless, the flow velocity is adjusted by the local speed-of-sound velocity, which is in turn designated by the composition of the two-phase mixture. The flow further acceleration downstream the nozzle throat corresponds to the expansion of the in-nozzle choked flow ( $M=1$ ). Almost full

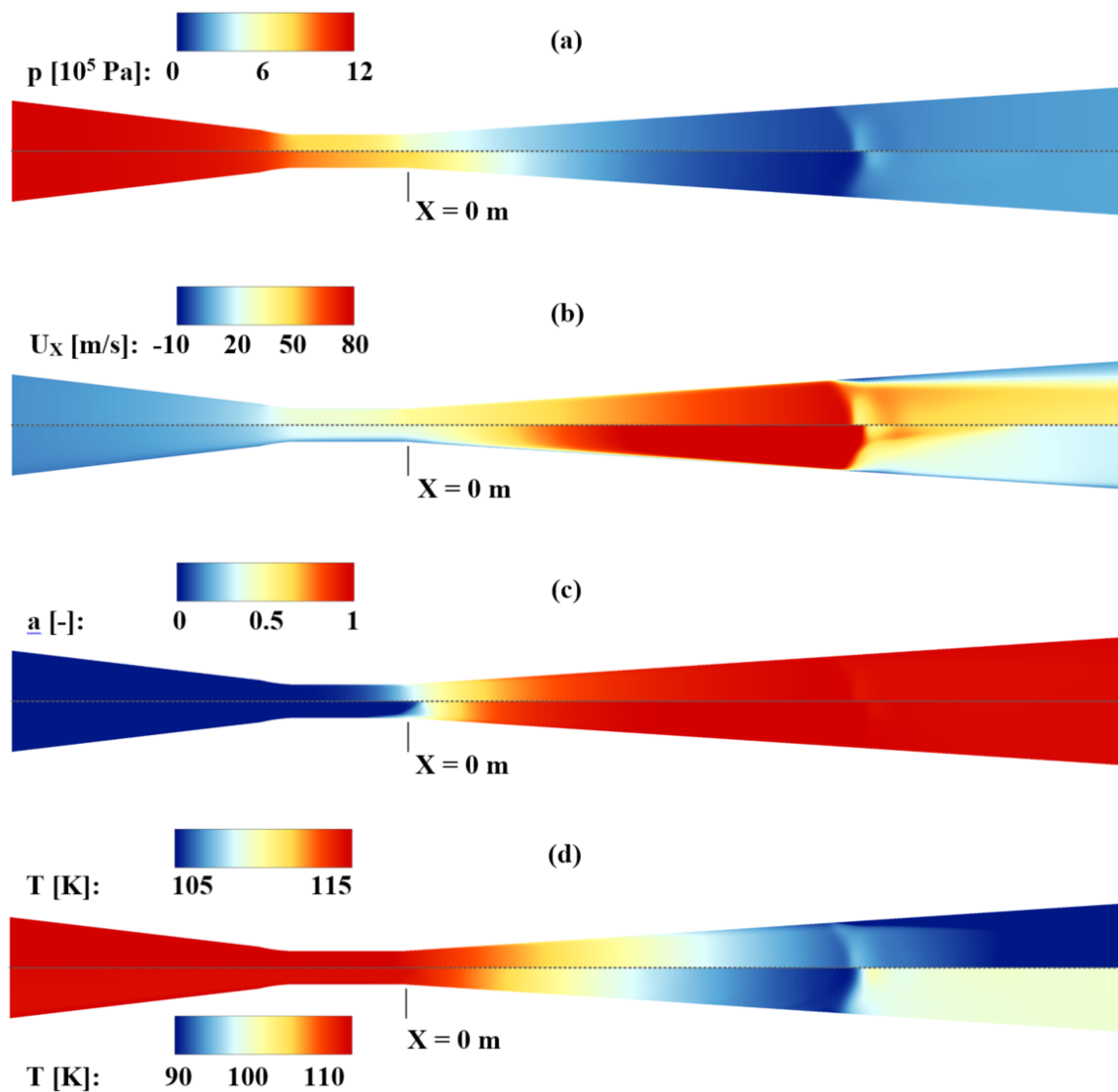


**Figure 4.7:** Contour plots of the (a) pressure, (b) velocity (c) gaseous volume fraction and (d) temperature field in the nozzle-throat region for case 1 of Table 4.2. It is noted that different variable ranges have been used in frame (d) to enhance clarity. Upper frames depict predictions produced using the Hertz-Knudsen ( $\lambda=0.7$ ) phase-change model (Equation 4.2), while lower frames those produced using the Helmholtz EOS (Equation 4.3). All contours represent the part of the nozzle from  $X=-0.045$  m to  $X=0.08$  m.

liquid vaporisation occurs at the diverging part of the geometry (Figure 4.7.c), thus, the value of the mixture Mach number increases (as highlighted also in Section 3.4). Furthermore, fluid temperature decreases in the region, as shown in Figure 4.7.d, due to the transformation of sensible to latent heat required for bubble nucleation. Although the physical-quantity fields predicted by the two solvers are qualitatively similar, distinct discrepancies can be detected, especially in the vapour fraction (Figure 4.7.c) and temperature fields (Figure 4.7.d). Those discrepancies are rooted in the inherent difference in the way that the rate of phase change is imposed in the two solvers. In essence, through the adoption of an EOS, an infinite phase-change rate is imposed and a homogeneous equilibrium model (HEM) is expressed by the density-based solver. On the contrary, the phase-change rate in the pressure-based counterpart is inherently finite due to the adoption of a thermal non-equilibrium phase-change model. Hence, the HEM predicts more rapid vapour formation in the nozzle throat (Figure 4.7.c), with noticeable after-effects in the flow and temperature fields.

Figure 4.8 depicts the distribution of physical quantities at the orifice axis of symmetry, as predicted by the two solvers for case 1, as well as the experimental data available by Hendricks et al. [5]. As it can be seen in Figure 4.8.a, the numerical results from both solvers are in good agreement with the experimental values regarding the axial pressure distribution. The profiles show an abrupt pressure drop initiating at the throat area along with a flow acceleration (Figure 4.8.b). The magnitude of the imposed phase-change rate leads to a noticeable variation between the axial velocity distributions obtained by the two numerical approaches. It is reminded that the thermodynamic closure of the density-based solver is based on tabulated data, intrinsically imposing thermodynamic equilibrium between the phases. On the contrary, phase-change in the pressure-based solver is designated by the source term in the vapour advection equation. It was verified through preliminary simulations that adopting an accommodation coefficient  $\lambda$  value (refer to Equation 4.2) of 0.7 gives the closest agreement between the predictions of the Hertz-Knudsen phase-change model and the experimental data of Hendricks et al. [5], which suggests a moderate yet clear departure from thermodynamic equilibrium. As already mentioned, the increased phase-change rate is the cause for the higher flow axial velocity (Figure 4.8.b) and vapour-fraction distributions in the throat region (Figure 4.8.c) obtained by the HEM. A higher vapour extent in the two-phase mixture forming in the nozzle throat affects the local speed-of-sound values and consequently the mixture acceleration in the diverging part. Likewise, the temperature drop is also linked to phase change; thus, the higher vapour formation observed in the case of HEM is associated with the

more extensive transformation of sensible to latent heat and consequent temperature decrease, as shown in Figure 4.8.d.

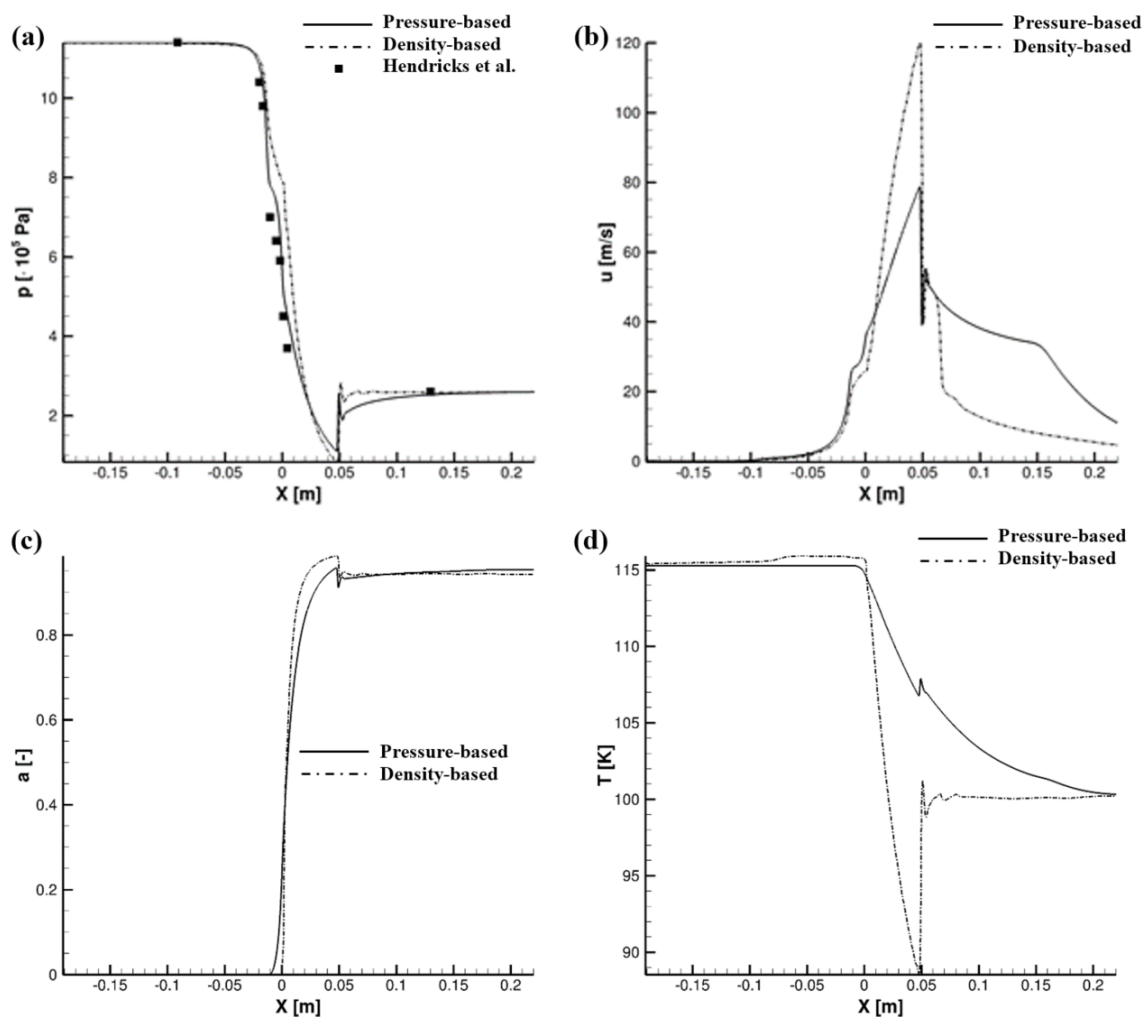


**Figure 4.8:** Distribution of (a) Pressure, (b) velocity, (c) vapour-volume fraction and (d) temperature at the orifice symmetry axis, as predicted by the two numerical approaches for case 1 of Table 4.2.

As an additional study of evaluating the accuracy of the proposed numerical approaches to replicate phase-change, the predicted mass flow rate through the nozzle has been compared against the measured value  $\dot{m}_{exp}$  ( $=0.27$  kg/s) by Hendricks et al. [5], for case 1 of Table 4.2. The discrepancies between numerical and experimental data are summarised in Table 4.4. As can be seen, the formulation based on the phase-change model achieves a closer agreement compared to the employing tabulated thermodynamics. In agreement with established knowledge regarding the departure of flashing flows from thermodynamic equilibrium ([152, 153, 69]) the density-based

solved imposing an infinite rate under-predicts the mass-flow rate, yet since only a moderate departure from equilibrium is experienced in the specific geometrical layout, as also shown in [4], the relevant results are still of acceptable accuracy.

**Table 4.4:** Evaluation of LOx mass-flow rate value through the orifice predicted by the two phase-change mechanisms for case 1 of Table 4.2.

Phase-change mechanism	Predicted $\dot{m}[\text{kg s}^{-1}]$	Deviation from $\dot{m}_{exp}$
Thermal non-equilibrium (pressure-based solver)	0.263	-2.59%
Thermal equilibrium (density-based solver)	0.247	-8.36%

The numerical results for case 2 of Table 4.2, characterised by a smaller pressure difference along the nozzle boundaries compared to case 1, are presented in Figure 4.9. A rapid fluid pressure drop at the nozzle-throat region followed by the manifestation of a series of pressure peaks at the diverging part is illustrated, particularly for the pressure-based solver (Figure 4.9.a, upper panel). The presence of this series of shock cells, which will be thoroughly discussed in Section 4.3.4, is a clear characteristic of an under-expanded jet and confirms the resemblance in expansion dynamics between two-phase flashing and supersonic gas jets [154]. Comparison between the upper and lower panels of Figure 4.9.a reveals that the locations of the first Mach disk (annotated as region 1) and oblique shock waves (region 2) are clearly discernible in the pressure field produced by the pressure-based solver (upper panel). On the contrary, the respective features cannot be clearly defined in the plot corresponding to the density-based solver. It must be noted that the specific solver converged to a transient, oscillating flow field, where the shockwave locations differed slightly over successive time instances, unlike the pressure-based counterpart that predicts an invariable flow field. Hence, the difference in shockwave dynamics is reflected in the time-averaged results presented in Figure 4.9. Figure 4.9.b depicting the axial velocity field also demonstrates a more significant flow deceleration at the locations of the normal and oblique shockwaves predicted by the pressure-based solver.

In a similar manner, distinct features emanating from the local pressure field are evident in the contour plots of the vapour-volume fraction depicted in Figure 4.9.c. Phase-change is not as extensive as in case 1 of Table 4.2, as it is disrupted due to the higher pressure to which the flow must equilibrate, in essence, through the formation of the complex shock-cell system. Once again, abrupt gradients of the

vapour volume fraction values in pressure-peak locations are evident in the predictions of the pressure-based solver, while the respective field produced by the density-based solver appears smoothed and somewhat ‘smeared’, owing to the averaging of the oscillating two-phase flow field. As expected, fluid temperature decreases in the throat region, as shown in Figure 4.9.d, due to phase change. Nevertheless, subsequent temperature increase takes place further downstream, in the nozzle diverging section, due to the compressible nature of the fluid, as the flow re-adjusts to higher pressures. Overall temperature differences are considerably more moderate compared to case 1.

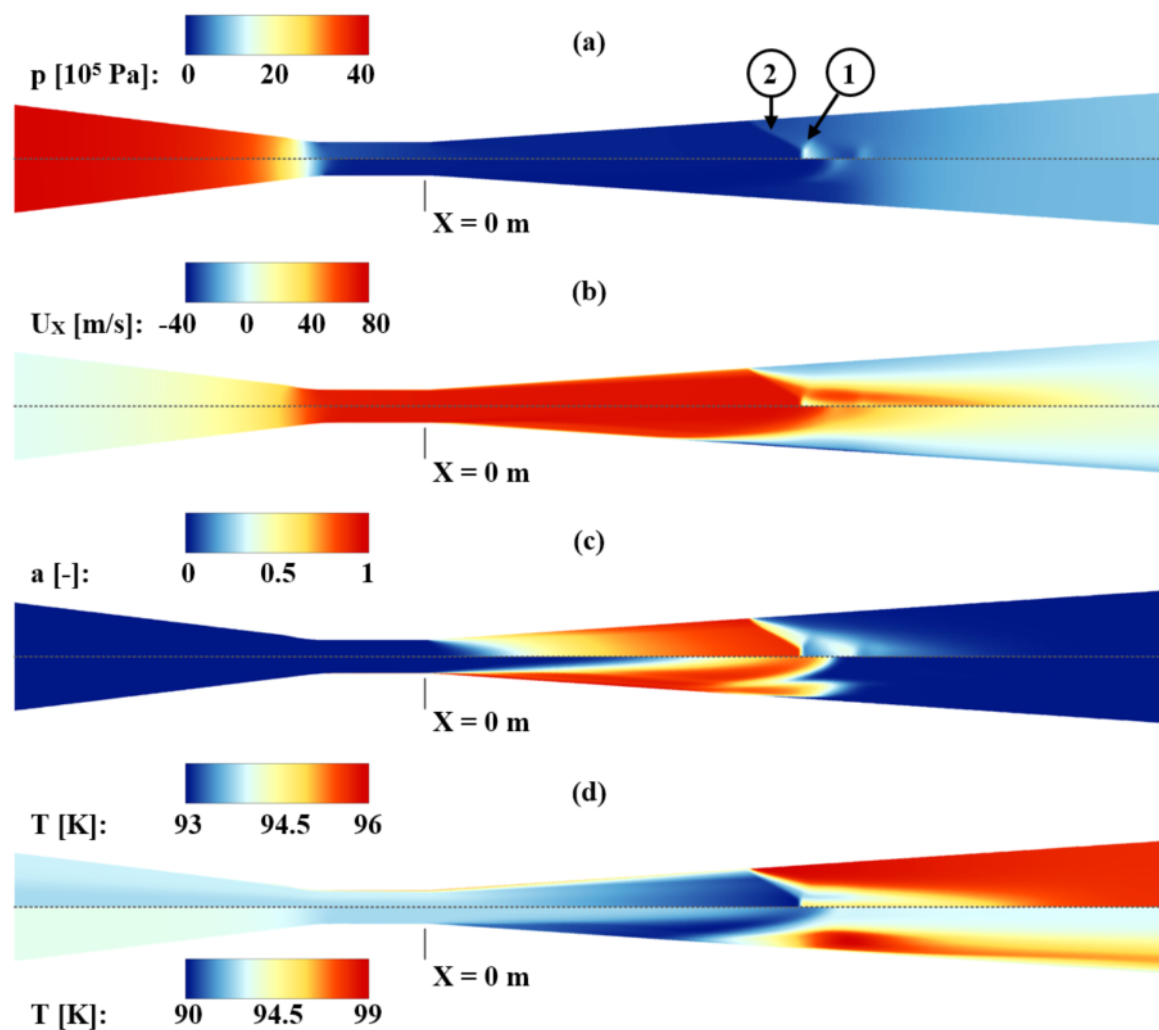


**Figure 4.9:** Contour plots of the (a) pressure, (b) velocity (c) vapour-volume fraction and (d) temperature fields in the nozzle throat region for case 2 of Table 4.2. It is noted that different variable ranges have been used in frame (d) to enhance clarity. The upper and lower panels depict predictions produced using the Hertz-Knudsen phase-change model (Equation 4.2) and the HEM/Helmholtz EOS (Equation 4.3), respectively. All contours represent the part of the nozzle from  $X = -0.045$  m to  $X = 0.08$  m.

Figure 4.10 depicts the axial distributions of physical quantities of interest at the orifice symmetry axis, as predicted by the two solvers for case 2. The pressure profiles of Figure 4.10.a highlight the discrepancies in the predictions of the two solvers, since the pressure peaks are much more clearly defined in the results produced by the pressure-based solver denoting the presence of two normal shockwaves. The transient nature of the results of the density-based solver will not allow for the shock formations to become evident on the presented time-averaged results as the shock axial location remains unsteady. The distinct features of the pressure field designate the respective velocity (Figure 4.10.b) and vapour-fraction distributions (Figure 4.10.c). Oscillations in both distributions can be detected at  $X \approx 0.08$  m where regions of high and low-pressure overlap, hence adjusting flow acceleration and phase change.

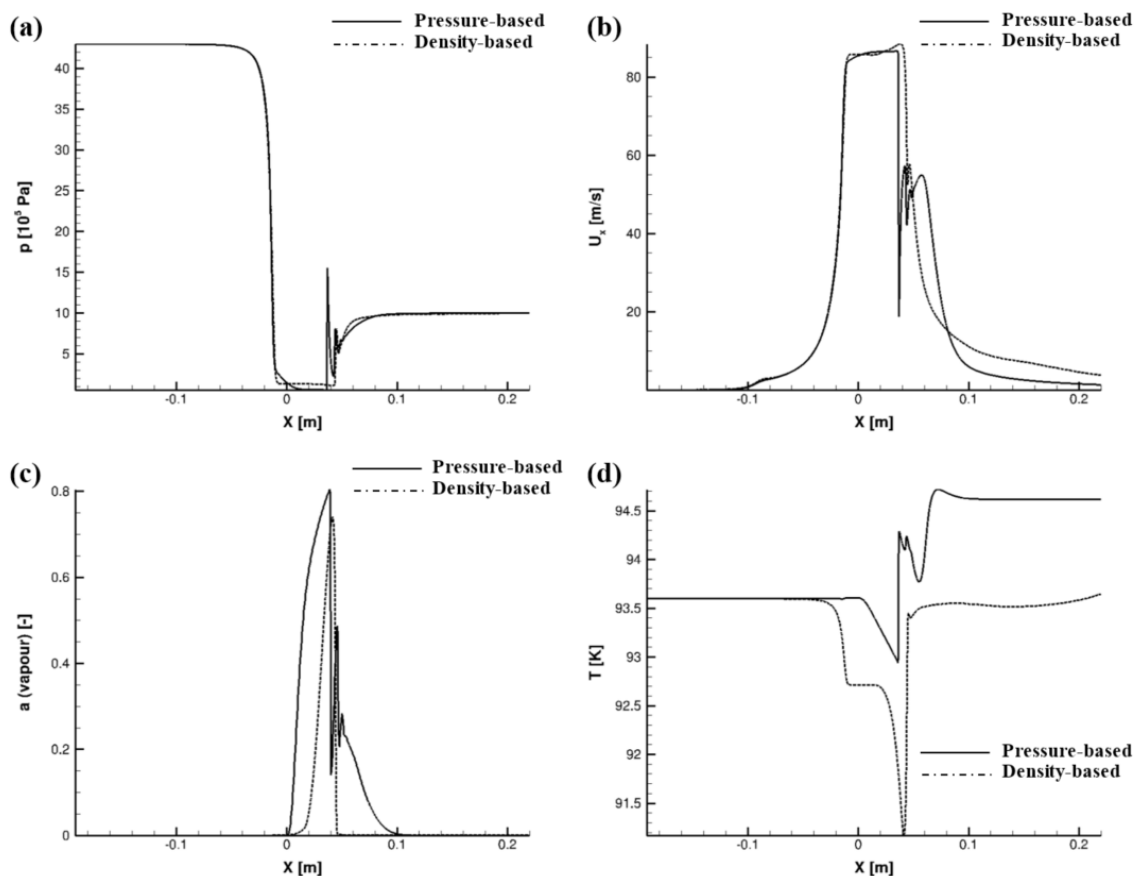


**Figure 4.10:** Distribution of (a) pressure, (b) velocity, (c) vapour volume fraction and (d) temperature at the orifice symmetry axis, as predicted by the two thermodynamic approaches for case 2 of Table 4.2.

The two approaches are in good agreement on the prediction of the maximum axial velocity immediately after the throat area. Unlike case 1, which corresponded to a lower outlet pressure outlet, full vapour condensation occurs in the diverging section and pure liquid exits the nozzle. The temperature distribution of [Figure 4.10.d](#) reveals that the mixture cools down only moderately during expansion, as phase-change is disrupted by the pressure re-adjustment to higher values. Once again, due to the infinite phase-change rate imposed, the temperature drop experienced is higher for the HEM approach.

### 4.3.3 Simulations in the supercritical regime

[Figure 4.11](#) illustrates the distinct features of the flow field with regards to supercritical pressure injection (case 3 of [Table 4.2](#)). Similar to the subcritical cases, the predictions of the two solvers are comparatively presented in each plot of [Figure 4.11](#). As can be observed, the two numerical approaches are in agreement regarding the overall flow evolution, which exhibits smooth transitions regarding all the plotted quantities. As expected, pressure decreases at the nozzle throat ([Figure 4.11.a](#)), as the flow accelerates due to the geometrical constriction ([Figure 4.11.b](#)). The fluid retains liquid-like densities throughout the domain ([Figure 4.11.c](#)), while the moderate depressurisation at the contracting section is accompanied by a mild temperature drop ([Figure 4.11.d](#)). All the distinct flow features identified for the two subcritical cases, i.e. flow expansion and formation of shockwaves, are completely absent in the supercritical regime.

Similar to the sub-critical cases discussed earlier, [Figure 4.12](#) presents in a comparative manner the distributions of the quantities of interest along the symmetry axis of the nozzle. The distributions of pressure ([Figure 4.12.a](#)) and density ([Figure 4.12.c](#)) demonstrate that since the entire flow process takes place at supercritical pressures, the fluid possesses liquid-like density, hence, compressibility effects are absent. Since all quantities are correlated to the medium density, the distributions of axial velocity ([Figure 4.12.b](#)) and temperature are also in good agreement ([Figure 4.12.d](#)). The pressure-based solver predicts slightly lower density values in the throat region than the density-based one. In this specific case, where both solvers employ tabulated thermodynamics, the differences in the results can be attributed to minor differences in the levels of accuracy and refinement of the tables from which thermodynamic properties are obtained.

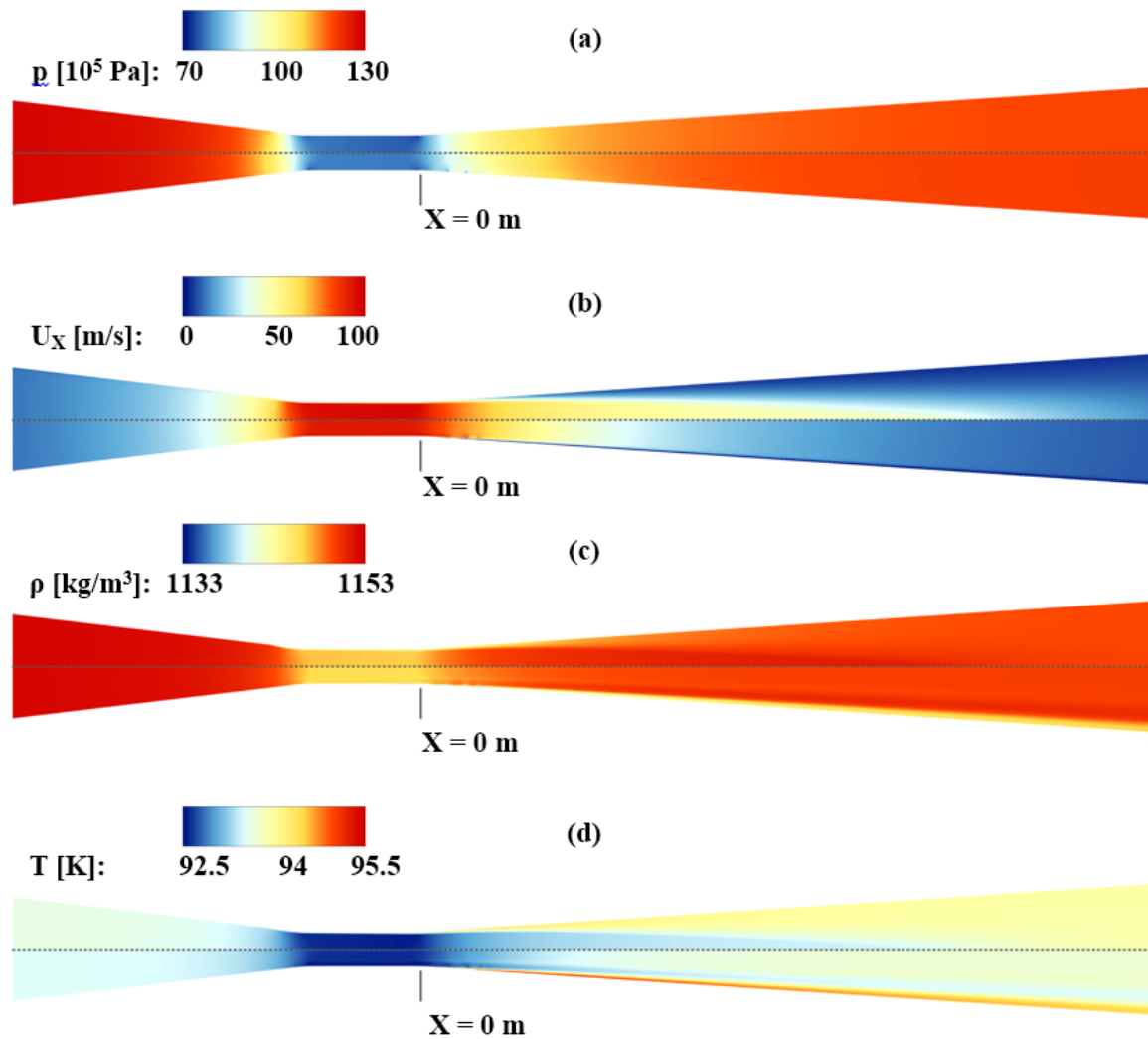


**Figure 4.11:** Contour plots of the (a) pressure, (b) velocity, (c) density and (d) temperature field for supercritical injection (case 3 of Table 4.2). The upper frames of each figure depict the predictions produced using the pressure-based solver and the NIST database, while the lower frames, those produced using a density-based solver and tabulated data produced by solving the Helmholtz EOS. All contours represent the part of the nozzle from  $X=-0.045$  m to  $X=0.08$  m

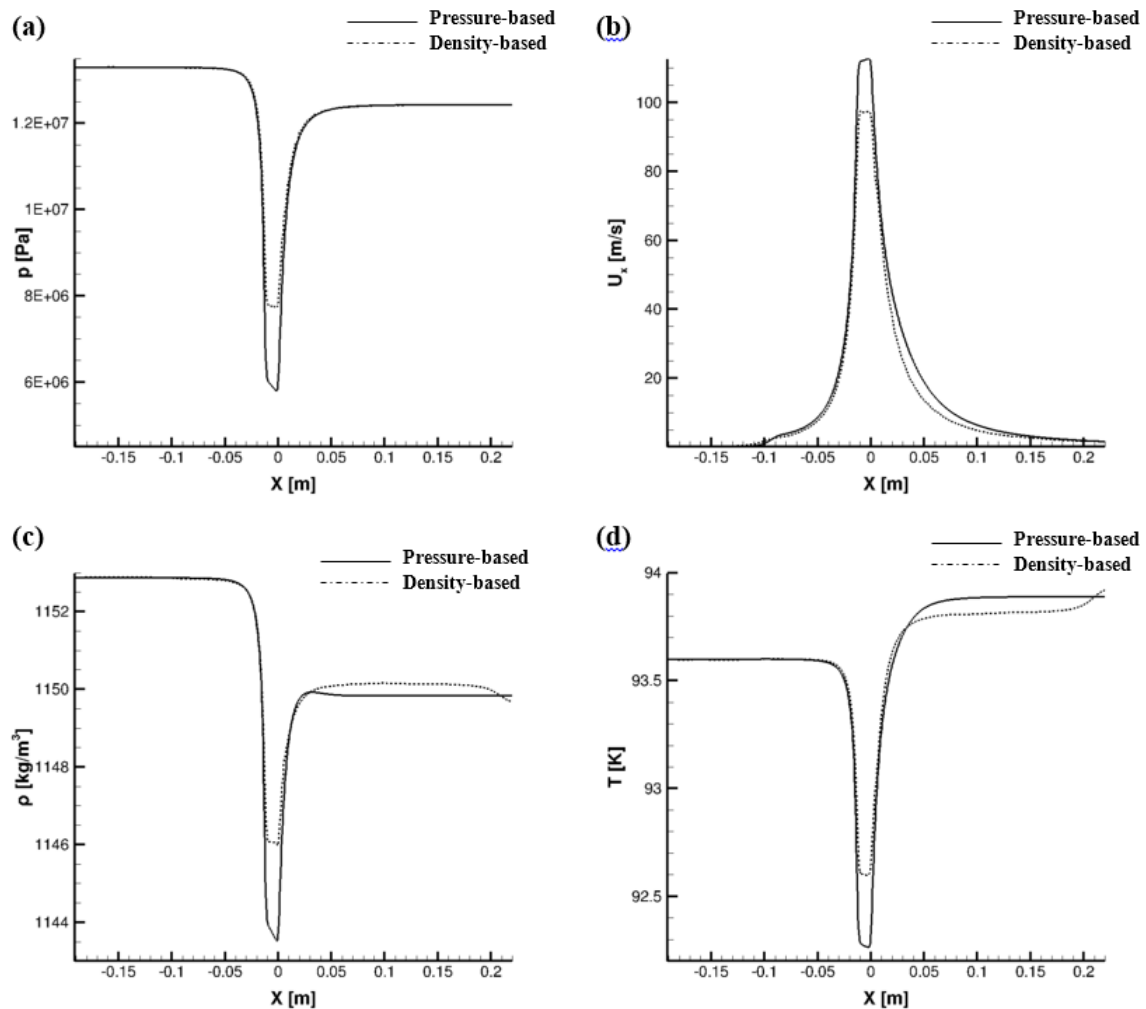


**Figure 4.12:** Distribution of (a) pressure, (b) velocity, (c) density and (d) temperature at the orifice symmetry axis, as predicted by the two solvers adopting different thermodynamic approaches for case 3 of [Table 4.2](#).

#### 4.3.4 Comparison of expansion dynamics for the two regimes

A comparison between the subfigures of [Figure 4.13](#) reveals that the flow evolution in the nozzle throat and downstream diverging region exhibits a highly variable behaviour between the subcritical and supercritical cases examined. In the subcritical pressure regime, the flow first becomes supersonic in the interior of the domain where sound speed is lowest. Shock waves occurring within the nozzle can interact with the boundary layer flow and result in a ‘shock train’ and a sequence of subsonic and supersonic flow, previously observed in single-phase nozzles ([\[155, 156\]](#)), refer especially to [Figure 4.13.b](#). Flow through the Mach stem is brought to subsonic velocities, while flow through the annular oblique shocks remains supersonic. The pressure across the boundary

between these two regions is matched, but temperature, entropy and velocity change almost discontinuously immediately downstream of the point where the oblique shock, Mach disk and reflected shock intersect, referred to as the triple point in relevant flow studies ([157, 158]). Turbulent mixing takes place across this boundary, eventually bringing the core of the flow back to supersonic velocities prior to the next shock cell. In the case of supercritical pressure (Figure 4.13.c), flow accelerates due to the geometry of the nozzle throat, without exceeding a Mach number of 0.2 at any point. In the diverging part, the flow decelerates with no discontinuities in any of the variable fields. As mentioned also in Section 4.3.3, the flow field exhibits no appreciable distinct features.

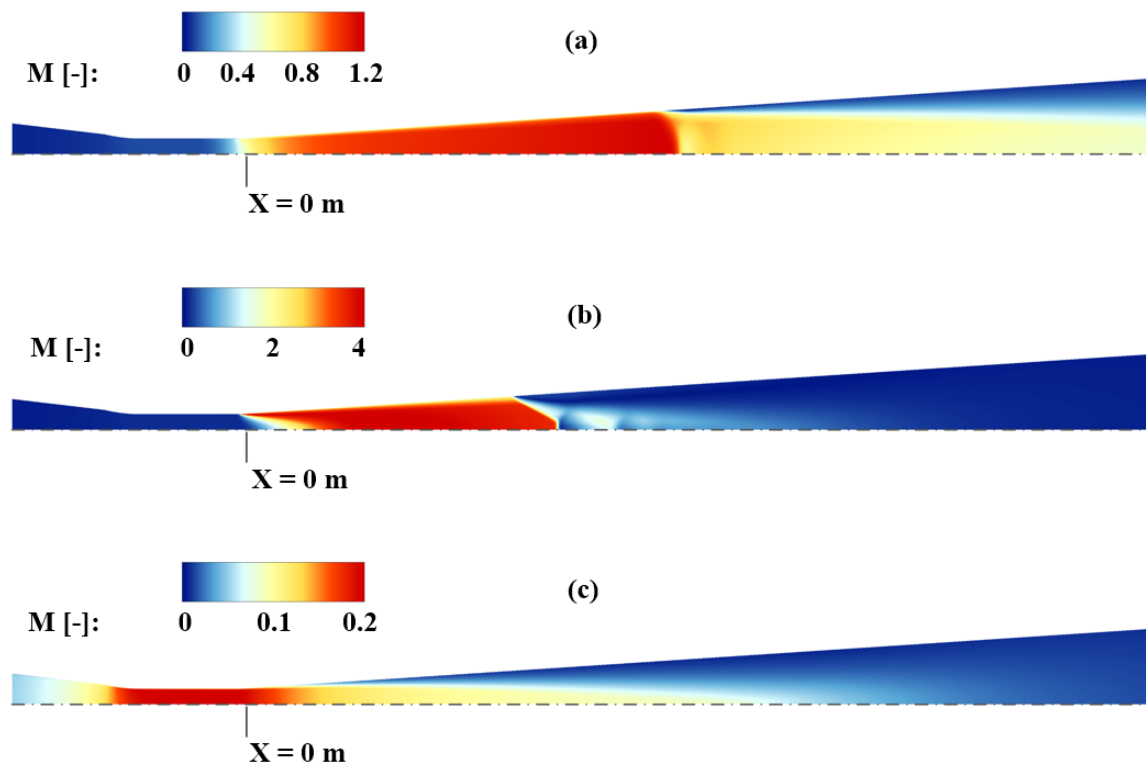


**Figure 4.13:** Contour plot of the Mach number in the throat and downstream regions (thermal non-equilibrium model). (a) Case 1 of Table 4.2:  $p_{in}/p_{out} = 11.4 \text{ bar}/2.6 \text{ bar}$ , (b) case 2 of Table 4.2:  $p_{in}/p_{out} = 43.0 \text{ bar}/10.0 \text{ bar}$ , and (c) Case 3 of Table 4.2:  $p_{in}/p_{out} = 133.0 \text{ bar}/124.2 \text{ bar}$ .

Figure 4.14 presents the axial velocity values on four different planes perpendicular to the nozzle axis of symmetry. For the subcritical case 2, Figure 4.14.a, where the flow reaches Mach values up to 4, it is clearly evident that the flow keeps accelerating past the nozzle throat ( $X = 0.0 \text{ m}$ ). Hence, the flow expansion due to the compressible nature of the two-phase mixture is once again demonstrated. On the contrary, with regards to the supercritical conditions where the fluid retains liquid-like densities (case

3, Figure 4.14.b), the flow reaches the maximum velocity at the end of the throat and then decelerates steadily, suggesting that any influence of compressibility is absent.

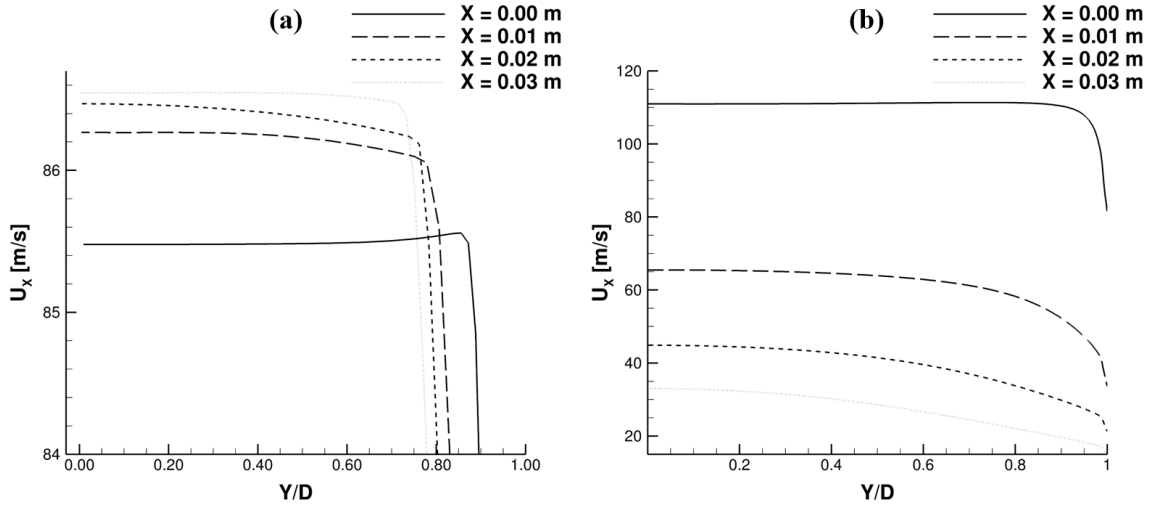


**Figure 4.14:** Cross-flow velocity profiles for (a) subcritical case 2 ( $U_{x,max} = 86.6$  m/s) and (b) supercritical case 3 ( $U_{x,max} = 111.4$  m/s of Table 4.2).

### 4.3.5 Flow instabilities

Flow instabilities arising due to the abrupt changes in pressure and density of the fluid are plausible to influence the flow field in the subcritical regime. In order to fully elucidate such effects, additional DES have been performed for cases 1 and 2 of Table 4.2. It should be noted that the pressure-based solver was employed in DES with the phase-change rate being imposed through Equation 4.2. Average fields were obtained for a total flow time of 5 ms, which is equivalent to 50,000 time steps, and are presented in Figure 4.15.

The elucidation of the influence of flow instabilities is of high practical importance since they can affect the delivery performance of the oxidiser injector with subsequent consequences on the combustion efficiency. A recirculation region has been identified immediately downstream of the Mach disk in numerical studies, yet experimental data do not verify this feature [159]. Figure 4.16 depicts three characteristic DES time instances for subcritical case 2 of Table 4.2, where a severe jet expansion has been observed; a detailed view of the region slightly downstream the nozzle throat is depicted. The black line evident on the vectors-over-contour plots signifies regions where  $M=1$ . The three instances make clear that the flow is oriented to the direction of the oblique shock waves and remains parallel in the region encompassed by the  $M=1$  iso-line. On the contrary, as depicted in all three instances a complex recirculation

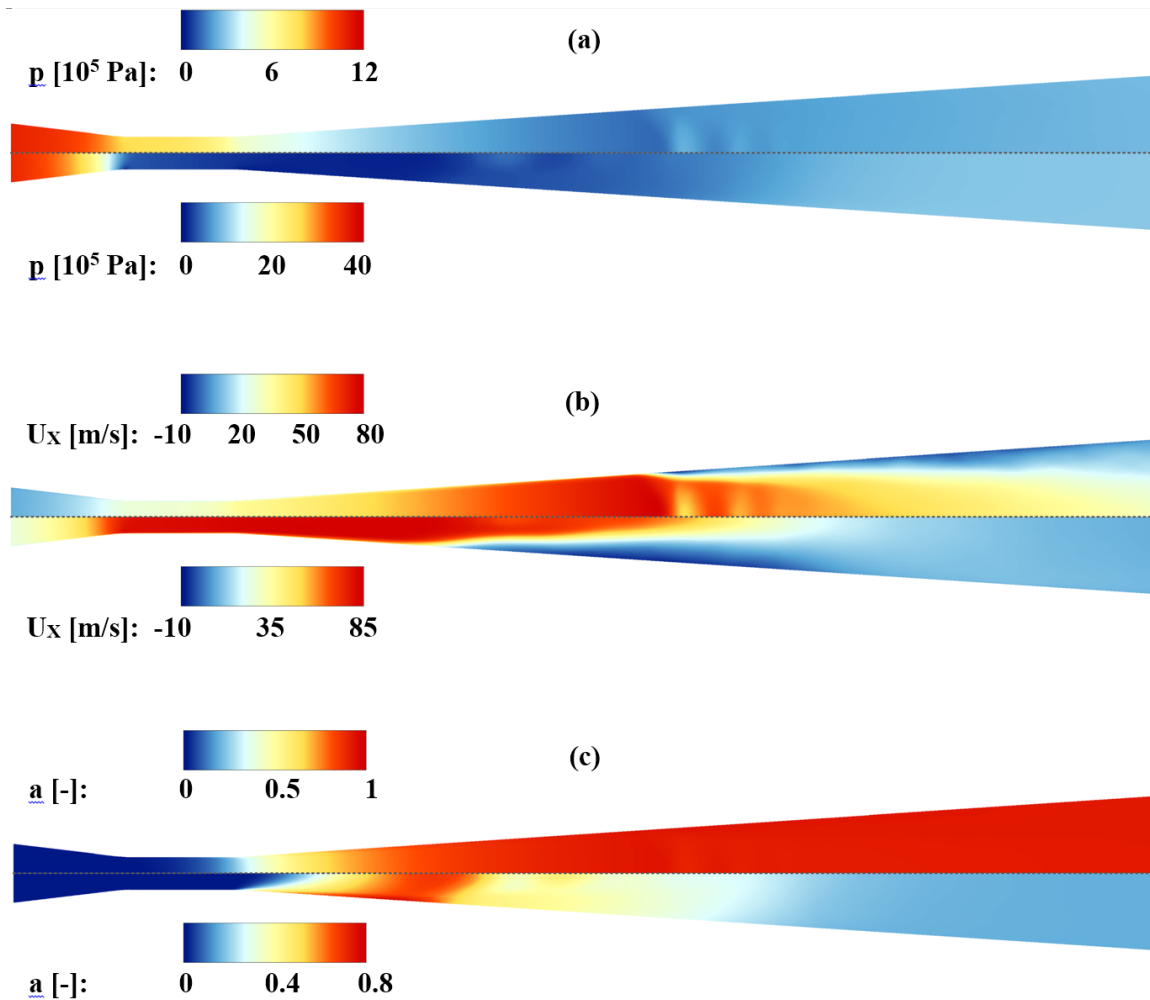


**Figure 4.15:** Contour plots of time-averaged field over the nozzle plane of symmetry. Results were produced using a detached eddy simulation (DES) approach. Upper frames correspond to case 1 and lower ones to case 2 of Table 4.2: (a) pressure (b) axial velocity and (c) vapour-volume fraction. The figures include the part of the nozzle from  $X=-23.5$  mm to  $X=98.2$  mm.

pattern sets in at the subsonic boundary layer. It is also interesting to notice in Figure 4.16.a and Figure 4.16.c that the flow turns away from the nozzle axis, i.e. towards the wall in the flow regions in the vicinity of  $M=1$  iso-lines (annotated as regions 1-3 in the plots). This flow behaviour is also similar to the velocity field of expanding supersonic gas jets [154]. Finally, as shown in Figure 4.16.b significant flow deceleration and transition to the subcritical regime perturbs the flow significantly, so as to induce the emergence of an extensive recirculation pattern even at the channel core (region 4), where parallel flow prevails in the other time instances.

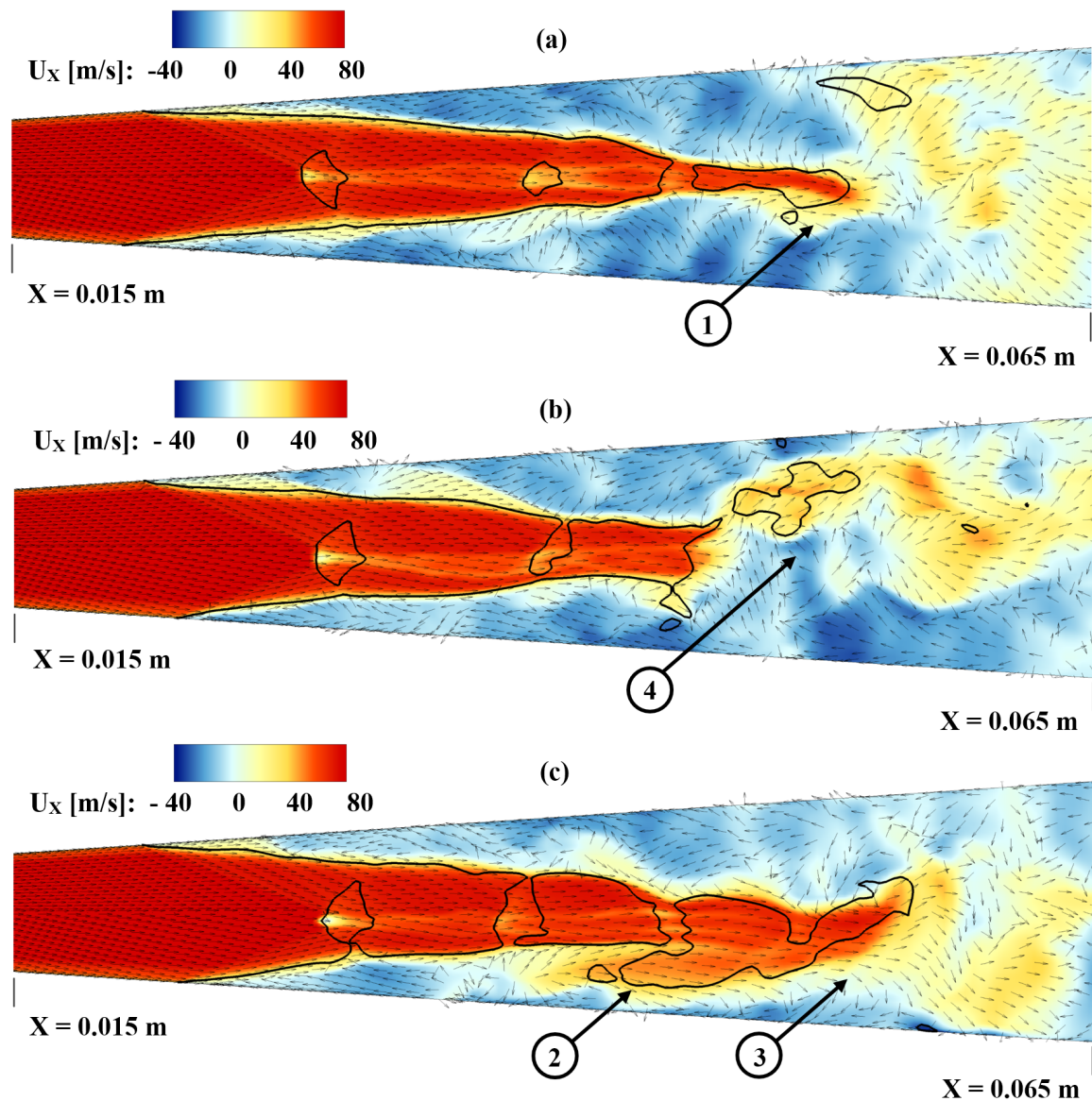


**Figure 4.16:** Velocity vectors over axial velocity contour plots in a detailed view after the nozzle throat exit ( $X=0.015$  m) corresponding to characteristic time instances of DES: (a)  $t = 0.240$  s, (b)  $t+1.0$  ms and (c)  $t+2.0$  ms. The black iso-line signifies  $M=1$  regions, while the numbered vectors indicate regions of distinct flow features

As can be observed in the three time-instances of [Figure 4.16](#), the locations in the channel core where the flow decelerates, thus denoting the presence of normal shockwaves, are not fixed in time for case 2. To highlight this behaviour, [Figure 4.17](#) presents the distribution of the pressure gradient over the nozzle symmetry axis for three different time instances. It is evident that the location and the magnitude of the first of the shock cells, which manifests in the vicinity of the axis are not stable but

rather oscillate in time, thus producing a less sharp representation on the time-averaged fields, a trend similar to that obtained by the density-based URANS solver (refer to [Figure 4.9](#) and [Figure 4.10](#)). These features have been verified to remain static for the subcritical case 1.

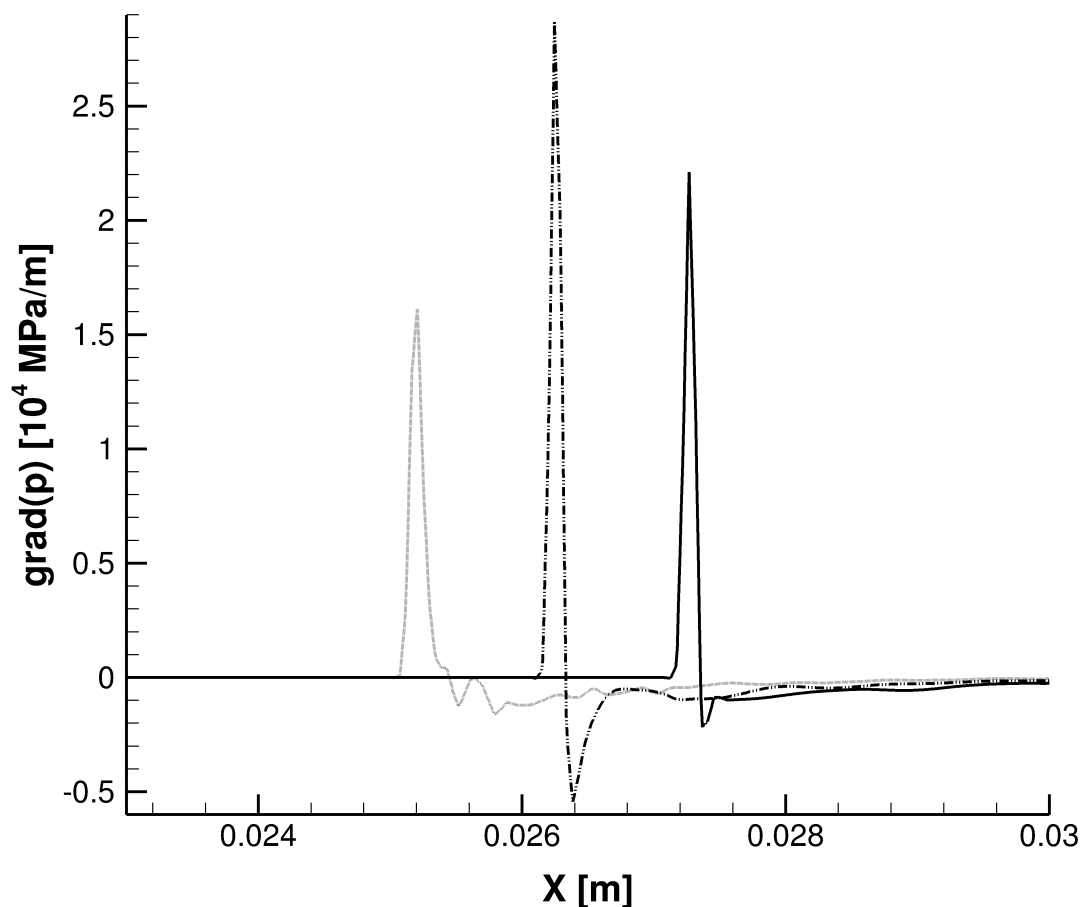


**Figure 4.17:** Distribution of the pressure gradient at the nozzle symmetry axis for case 2 of [Table 4.2](#). Time difference between the instances is 0.08 ms.

In order to highlight the manifestation of turbulence within the nozzle, [Figure 4.18](#) presents a visualization of the vortical structures arising for the subcritical cases 1 and 2, based on the DES results, using Q-criterion iso-surfaces. A common characteristic for both cases constitutes the almost complete absence of structures in the throat region. Rings are only formed on the walls of the nozzle where the constant-diameter throat begins and ends. A multitude of vortical structures emanating from the shockwave location develops in the diverging section of the nozzle, which occupies the major part of the section for case 1 ([Figure 4.18.a](#)), for which the flow retains high velocities until

the outlet, refer to Figure 4.15. The relevant distribution for case 2 (Figure 4.18.b) exhibits structures of smaller scale densely forming in the region of the shock-diamond system, yet decaying well upstream the nozzle outlet due to the low flow velocities past the normal-shock sequence.

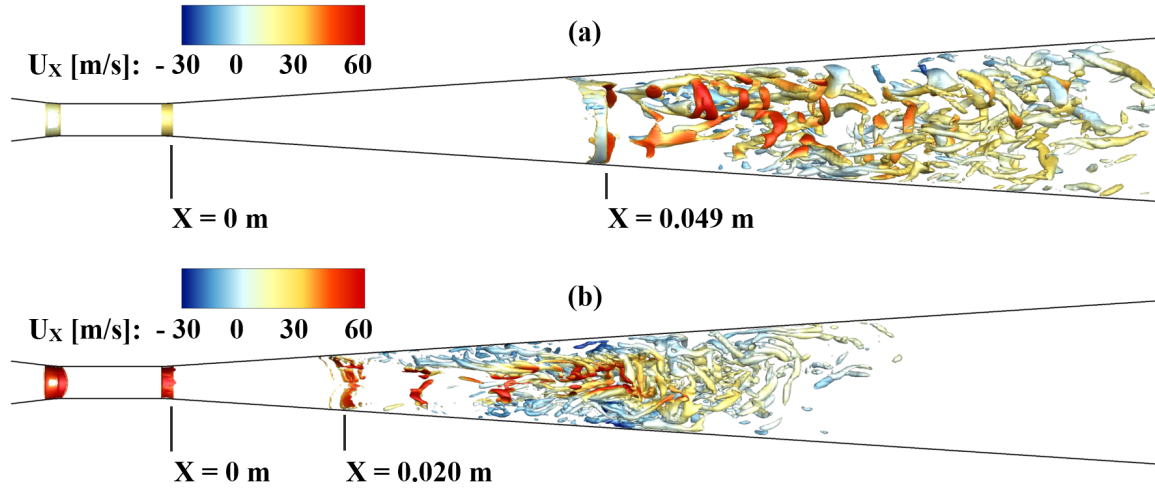


**Figure 4.18:** Visualisation of vortices using Q-Criterion iso-surfaces ( $Q=2\times 10^8$ ) coloured by axial velocity values for the DES results of (a) case 1 of Table 4.2:  $p_{in}/p_{out} = 11.4 \text{ bar}/2.6 \text{ bar}$  and (b) case 2 of Table 4.2:  $p_{in}/p_{out} = 43.0 \text{ bar}/10.0 \text{ bar}$ . The figures include the part of the nozzle from  $X=-0.017 \text{ m}$  to  $X=0.11 \text{ m}$ .

## 4.4 Concluding remarks

Two-phase oxygen flow was numerically investigated in a converging-diverging nozzle in both sub- and supercritical pressure conditions using both URANS simulations and DES. The selected conditions are typical for the component operation of lower and upper-stage rocket engines. Two phase-change mechanisms have been utilized. A finite phase-change rate imposed by a Hertz-Knudsen-type equation was found to give the most accurate results regarding the two-phase oxygen flow field in the subcritical regime, suggesting a moderate departure from thermodynamic equilibrium. Nevertheless, the tabulated approach based on the Helmholtz EOS proposed in this work was found to produce results of sufficient accuracy for both sub- and supercritical pressure regimes, hence, rendering it a universal modelling approach for cryogenic fluid injection. From a flow physics standpoint, in the supercritical regime, the flow exhibits smooth transitions for all quantities of interest. Overall, the flow field exhibits no appreciable distinct features and abrupt gradients. On the contrary, in the subcritical regime, flash boiling of LOx takes place, i.e. abrupt vaporisation of the liquid phase,

accompanied by flow acceleration to supersonic velocities and abrupt pressure gradients. In the case of the most severe two-phase jet expansion, a series of shock-diamonds set in at the nozzle diverging region verifying the flow similarity to the expansion of a supersonic gas jet. DES demonstrated that the flow transition from the super- to the subsonic regime perturbs the velocity field and gives rise to extensive recirculation patterns both in the boundary-layer region, as well as in the channel core. The main findings of this study are applicable to propulsion components of space vehicles where LOx is currently the prevalent oxidiser option but also to other applications where cryogenic liquids are the working media, e.g. CO<sub>2</sub> for refrigeration systems [160].

# CHAPTER 5

## Modelling of liquid oxygen and nitrogen injection under flashing conditions

The present numerical investigation of two-phase flashing flows examines the injection of liquid oxygen and liquid nitrogen into near-vacuum conditions prevailing in the upper-stage boosters of rocket engines. The predictive capability of a pressure-based solver and a density-based solver, each employing distinct approaches related to the imposed phase-change rate and thermodynamics closure, has been comparatively evaluated. Regarding the pressure-based solver, the departure from thermodynamic equilibrium during phase change has been taken into account via the implementation of a bubble-dynamics model employing the Hertz-Knudsen equation and assuming thermal non-equilibrium. In contrast, the density-based solver relies on the adoption of thermodynamic equilibrium while real-fluid thermodynamic properties are assumed by loading tabulated values to the solver. Each thermodynamic property value was calculated in advance by solving the Helmholtz Equation of State (EOS) for a wide range of density and internal energy conditions. Numerical findings have been compared against experimental data available in the literature. The comparison demonstrates the capability of both methodologies in capturing the evolution of cryogenic flashing flow expansion, phase change, and spray formation. The salient features identified in the numerical results, i.e. the expansion sphere immediately downstream of the injector exit, the bell-shaped topology of the spray, as well as the dependency of the spray cone angle on superheat, are in agreement with experimental measurements. Especially the thermal equilibrium approach has been proven highly accurate with respect to the steady expanding flow described by a level of superheat in the range of 3 to 245, while also being independent of any parameter tuning.

### 5.1 Introduction

Cryogenic propellants in liquid-state have been utilized since the 1960s [113] and are currently the selected type of propellants for many modern upper-stage rocket engines. The combination of LOx and LH<sub>2</sub> has been used to propel the main engines of NASA's space shuttle [161], Ares-I vehicle [162], the Centaur engine of Atlas rocket [114] and ESA's Ariane 5 upper stage engines [115], while SpaceX's Falcon and Blue Origin's BE-4 rocket, use as propellants a mixture of LOx/LCH<sub>4</sub> and LOx/Liquefied natural gas (LNG), respectively [163, 164]. For the lower-stage engines, LOx/RP-1 is a very common propellant mixture with Saturn V, Atlas V, the Russian Soyuz and Falcon being some of the rockets that operate on it [165, 166].

While the initial lift-off of a space launch vehicle takes place in atmospheric conditions, the upper-stage engines are expected to ignite and operate in near-vacuum conditions. Those low-pressure operating conditions of second-stage engines can lead to flash evaporation or flash boiling of the propellants during start-up, which can affect the ignition process [167, 134, 7, 29]. Investigation of cryogenic flash boiling is, therefore, essential for understanding and controlling the process. Extremely low pressure and temperature storage conditions required for cryogenic fluids, as well as the intense phase-change rates during flash evaporation, are hindering factors to the realization of experimental campaigns and, thus, the open literature relevant to the topic is relatively limited.

An early NASA report by Hendricks et al. [5] offers experimental data in terms of mass flow rates and pressure distribution of two-phase mixtures of LOx and LN<sub>2</sub> flowing through different types of converging-diverging nozzles for a wide range of sub- and super-critical conditions. Mayer and co-workers [47, 48] presented flow visualizations and measurements related to the propellant (LOx/H<sub>2</sub>) injection, mixing, evaporation, and combustion in a liquid rocket engine combustor at sub- and super-critical chamber pressures. The injection visualizations and studies under combusting conditions revealed a remarkable difference between subcritical spray formation and evaporation, and the supercritical injection and mixing processes. The experimental studies conducted on ONERA's Mascotte test bench [50, 49] focus mainly on the combustion processes involved in cryogenic propellant LOx/H<sub>2</sub> systems, although the characteristics of LOx sprays have also been investigated. The work of Chehroudi et al. [120] is focused on LOx and LN<sub>2</sub> injection into environments composed of N<sub>2</sub>, He, Ar, and CO/N<sub>2</sub> mixtures. Boundary conditions vary from sub- to supercritical and the resulting flows were captured by a CCD camera with the use of backlit illumination. A Subsequent work by Chehroudi gives an overview of experimental efforts to elucidate

the distinct features of high-pressure supercritical injection [168].

In contrast to the aforementioned publications that study the behaviour of cryogenic fluids for pressure regimes higher than atmospheric, experimental data on cryogenic flashing sprays at near-vacuum conditions are rare. A noteworthy mention should be made of the cryogenic facility at the Technical University of Munich (TUM) and the DLR facility, dedicated to fundamental research on cryogenic spray atomisation, ignition and combustion [46]. At TUM, Luo and Haidn [29] investigated a flashing LN<sub>2</sub> spray in a low-pressure environment using high-speed diffuse-light visualisation. The authors confirmed the correlation between the value of the non-dimensional energy barrier to nucleation, *chi*, and the transition from mechanical to flash-induced atomisation. They demonstrated that the onset of the fully flashing regime occurs at a *chi* value of around one. The same conclusion was reached by Lamanna et al. in [30], where a systematic study of flash atomization of standard and retrograde fluids using background illumination took place. Additionally, the authors reported the appearance of complex shock-wave structures at very high initial superheat. Finally, at the DLR facility, Lamanna et al. [7] investigated fully flashing LOx and ethanol sprays with the use of diffuse-light high-speed imaging. The authors demonstrated that the inception of flash boiling in cryogenic propellants requires a higher degree of superheat compared to storable propellants.

More recently, in the work of Rees et al. [24], the characteristic morphologies of the flash boiling LN<sub>2</sub> sprays like breakup patterns and spray angles were investigated with the use of high-speed shadowgraphy. Among the conclusions, the authors propose the introduction of a fourth breakup regime for highly superheated jets, the wide-flashing regime. In addition, in [8] a laser-based Phase Doppler system was set up to determine the spatial distributions of droplet velocities and diameters in highly superheated sprays. According to the authors, the droplet diameter decreases with increasing injection temperature; however, the dependence of the droplet diameter on the injection temperature is less dominant for increasing injection pressures and the droplets are bigger at the same injection temperatures.

The scarcity of cryogenic-flashing experimental data makes the need for accurate and robust numerical methods to simulate the phenomenon imperative. An accurate numerical prediction of such two-phase flows can lead to a better understanding of the underlying flow and phase-change processes. In the case of injector orifices under flashing conditions, the fact that the rapid evaporation of the fluid has a tremendous influence on the characteristics of the resulting spray is overall supported by the experimental data. The importance of flashing for the evolution of sprays has been

acknowledged in the area of gasoline direct injection (GDI) engines and the research is intense both in terms of experimental and numerical approaches [22, 23]. Cryogenic flashing has also been investigated for cooling purposes [169] while studies on water, refrigerants, and light hydrocarbons have shown that in the case of in-nozzle flash evaporation, finer sprays, wider cone-angles and reduced penetration lengths compared to flows subdued to inertia-driven phase-change are observed [31]. Safety concerns for fuel applications [170] but especially with respect to aerospace and nuclear applications have led to further numerical investigations of flash boiling. The relevant cryogenic flow processes and, consequently the numerical methodology presented are also relevant to a wide range of other applications, ranging from gas liquefaction and desalination to cryosurgery and food freezing [171, 172, 173, 174].

In cases of very rapid depressurisation, an initially subcooled liquid can transit to the meta-stable region, having a pressure equal to the respective saturation value, yet a temperature higher than the respective saturation value. When in the metastable state, the system can remain stable for small fluctuations of the thermodynamic variables. However, due to the pressure disturbances, the metastable conditions cannot be maintained for a long time. The metastable liquid will overcome the energy barrier to nucleation and release its latent heat through the flash-evaporation process, finally evolving to the global minimum of free energy and reaching a new equilibrium stable state. Metastability effects play an important role in transient processes [18]. In nuclear safety analysis, flashing phenomena are present in the case of a loss of coolant accident (LOCA), as well as inducing flow instabilities in passive safety systems driven by natural circulation. Liao and Lucas present the relevant advancements in the field in [175] and [18].

Nevertheless, not many numerical investigations highlighting the distinct characteristics of cryogenic sprays can be found in the open literature. In the work of Travis et al. [132], a theoretical two-phase model based on the Helmholtz energy EOS is developed. To account for the non-equilibrium effects, the homogeneous equilibrium model was modified and used for determining the critical flow rate for choked cryogenic flows. Lyras et al. [133] utilized the volume-of-fluid method coupled with the homogeneous relaxation model to investigate the flash boiling process and subsequent spray expansion of a liquid nitrogen flow through a throttle nozzle. Chen et al. [176] proposed a two-fluid numerical model that couples an interface area density model to the homogeneous relaxation model (HRM) for investigating the underlying physics of liquid nitrogen spray formation. In a numerical and experimental campaign to study flashing liquid nitrogen, Gärtner et al. [88] used a one-fluid approach, with tabulated

thermodynamic properties and the HRM to account for phase change. In the recent works of Lureiro et al. [177, 178] a multiphase solver based on the volume of fluid method and piecewise linear interface calculation (PLIC) reconstruction is used to perform direct numerical simulation) of the flash atomization of cryogenic LOx in the micro-scale and characterise the primary breakup regimes, as well as calculate the droplet-size distribution within the spray. Schmehl and Steelant [134] utilized an Eulerian-Lagrangian framework to simulate the pre-flow of nitrogen tetroxide ( $N_2O_4$ ) oxidizer during the start-up of an upper-stage rocket engine. To account for the flash-induced expansion of the jet, an empirical flash atomization model was used. Ramcke et al. [135] used a similar numerical approach utilizing a simplified droplet flash evaporation model to investigate the pre-flow of LOx for satellite rocket engines. The aforementioned publications reveal that both cryogenic and storable flashing liquid sprays exhibit analogous characteristics, namely enhanced droplet atomisation, increased cone angle and acceleration of the compressible mixture.

The above review of the existing literature makes it clear that although effective approaches have been implemented to predict cryogenic liquid injection and flashing evaporation, the proposed methods are developed depending on specific thermodynamic conditions and application needs. Previous work by the author's group in [138, 139] has demonstrated the robustness of the technique in modelling phase-change and spray mixing in fuel-injection applications. To the authors' best knowledge, this is the first work in the open literature to propose and evaluate a universal modelling framework suitable for the prediction of multiphase, cryogenic wall-confined and unconfined spray-flow characteristics, for pressure outlet environments that range from near-vacuum to supercritical [160]. More specifically, a time-resolved, explicit, density-based solver implementing a Mach-number consistent numerical flux scheme has been developed and utilised. Thermodynamic properties of the operating fluids were computed by solving the Helmholtz energy Equation of State (EOS) and inserted in the numerical code in tabulated form. In the context of examining flash boiling during second-stage engine ignition, liquid oxygen has been selected as the operating fluid due to its extensive use as an oxidiser. To further evaluate the developed solver, liquid nitrogen was also considered due to the availability of experimental data for flash boiling conditions. In parallel with the developed density-based solver, a coupled (pressure-based) solver utilising a kinetic-theory-based model is examined to comparatively assess the accuracy of numerical predictions produced with the use of diverse phase-change modelling approaches.

This universal methodology based on tabulated thermodynamics that is applicable

to a wide range of superheat levels, is presented in a comparative manner against the Hertz-Knudsen kinetic-theory-based mass transfer model and validated against relevant experimental data. This phase-change model can be calibrated to model flash evaporation for various superheat levels and therefore produce accurate results; however initial calibration data must be available. The use of a thermodynamic table with real-gas thermodynamic properties produces accurate results for high superheat values while capturing the process with satisfactory accuracy for lower values of superheat. The advantage of the tabulated methodology is that after the initial table of fluid properties is created for a range of conditions, no calibration is needed since the phase change rates are dictated by the tabulated real-gas thermodynamics. Therefore, the tabulated approach can be a flexible methodology to be used when examining a specific fluid for a wide range of conditions or different geometries. Overall, this investigation aspires to clarify the effectiveness of the two aforementioned approaches in simulating cryogenic flows of liquid oxygen and nitrogen under extreme flash boiling, near-vacuum conditions.

## 5.2 Methodology

Two flow solvers have been employed in the present investigation, i.e. an implicit coupled pressure/velocity solver (nominally referred to from now on as ‘pressure-based’) and an explicit density-based solver. The basic set of governing equations solved in both cases comprised the continuity, momentum and energy conservation equations, the fundamental formulations of which can be found in the work of Karathanassis et al. [4] and are summarised below.

$$\frac{\partial(\rho_{mix})}{\partial t} + \nabla(\rho_{mix}\vec{u}) = 0 \quad (5.1)$$

$$\frac{\partial(\rho_{mix}\vec{u})}{\partial t} + \nabla(\rho_{mix}\vec{u}\vec{u}) = -\nabla p + \nabla[\mu_{mix}(\nabla\vec{u} + \nabla\vec{u}^T)] \quad (5.2)$$

$$\frac{\partial}{\partial t} \sum_{i=1}^2 (\alpha_i \rho_i E_i) + \nabla \sum_{i=1}^2 (\alpha_i \vec{u} (\rho_i E_i + p)) = \nabla(k_{mix} \nabla T), \quad E_i = h_i - \frac{p}{\rho_i} + \frac{u_i^2}{2} \quad (5.3)$$

In equations 6.1 to 6.3,  $\rho$  denotes density,  $\vec{u}$  is the velocity vector,  $t$  is time,  $p$  represents the pressure field and  $\mu$  is the fluid viscosity. The volume fraction of each

phase is  $\alpha$ ,  $k$  denotes the thermal conductivity of the two-phase fluid,  $T$  stands for temperature and finally,  $h$  is the sensible enthalpy. The index “mix” corresponds to the mixture and “i” to a specific phase of the mixture. The complete numerical methodologies, along with the sets of equations solved have been described in more detail in previous works of the authors’ group, specifically in the work of Karathanassis et al. [4] regarding the pressure-based solver and Kyriazis et al. [105, 140] regarding the density-based solver.

With respect to the coupled (pressure-based) solver, a two-phase mixture approach was implemented, including an additional equation for the vapour transport, as outlined in the following section. Numerical schemes with  $2^{nd}$  order accuracy were employed for the discretisation of the governing equations. More specifically, the QUICK scheme was employed for the discretisation of the vapour-fraction equation, while a second-order upwind scheme was used for density interpolation, as well as for the discretisation of the momentum and turbulence transport equations. An implicit second-order backward differencing technique was used for time integration with a time step value of  $10^{-8}s$ , resulting in a CFL-criterion value smaller than 1 in the entire computational domain for all the pressure-based solver simulations. The solution for each time step was deemed as converged, once the residuals for the set of governing equations employed by the solver dropped by at least three orders of magnitude.

In the case of the density-based solver, a single-fluid modelling approach has been formulated and the 3-D URANS equations in conservative form were considered. In essence, an infinite phase-change rate was assumed at the bubble interface, i.e. the establishment of thermodynamic equilibrium, and the entire process was replicated by an appropriate EOS (refer to [Section 5.2.2](#)). The interphase temperature in the present investigation is taken as equal to the local cell temperature, which is calculated by the solution of the energy equation. Thermodynamic non-equilibrium and its effects play an important role in flashing conditions during highly transient processes with abrupt pressure gradients [18]. All the examined cases, however, reach a quasi-steady solution. The thermal equilibrium assumption, imposed by the density-based solver can, therefore, produce accurate results, as also demonstrated for cryogenic fluids in [160]. Additionally, it should be noted that the pressure-based solver’s phase-change model calibration yielded an accommodation coefficient value of  $\lambda = 1$ , suggesting close-to-equilibrium thermodynamic conditions. Since the Mach number is probable to obtain highly different values in the pure liquid, vapour and two-phase mixture regions, a Mach-number consistent numerical flux has been implemented based on the HLLC and the AUSM fluxes [106, 107]. Conservative variables at cell interfaces,

required for the calculation of the fluxes, were determined using the MUSCL-Hancock reconstruction [108],  $2^{nd}$  order accurate in space. A  $4^{th}$  order accurate, four-stage Runge-Kutta method has been selected for time integration, with a CFL criterion of 0.1 imposed for all the density-based explicit solver simulations performed. Again, the solution for each time step was deemed as converged, once the residuals for the set of governing equations employed by the solver dropped by at least three orders of magnitude.

### 5.2.1 Mass-transfer model

As mentioned, a two-phase mixture model was employed in the coupled, pressure-based solver to capture the phase-change process under flash-boiling conditions. Mechanical equilibrium, i.e. a common velocity field, was also assumed for the two phases. Regarding the liquid phase, compressibility was imposed with the use of Tait EOS using a reference density of  $1022.1 \text{ kg/m}^3$  at  $p = 17 \text{ bar}$ ,  $T = 113 \text{ K}$  for LOx and a reference density of  $782.86 \text{ kg/m}^3$  at  $p = 4 \text{ bar}$ ,  $T = 82.5 \text{ K}$  for LN<sub>2</sub>. The respective vapour phases were treated as ideal gases. The reference values of latent heat of evaporation were taken equal to  $185.25 \text{ kJ/kg}$  for LOx at a temperature of  $113 \text{ K}$  and  $192.19 \text{ kJ/kg}$  for LN<sub>2</sub> at a temperature of  $82.5 \text{ K}$ . Energy transfer between liquid and vapour phases was calculated based on reference latent heat values, the integration of heat capacity of each fluid for a temperature range and the calculated phase-change rate. The set of governing equations for the mixture was complemented by an advection equation (Equation 5.4) for the conservation of the vapour phase volume fraction.

$$\frac{\partial(\alpha_v \rho_v)}{\partial t} + \nabla(\alpha_v \rho_v \vec{u}) = \dot{R} \quad (5.4)$$

where the phase-change rate  $\dot{R}$  corresponds to flash vaporization. For the simulations conducted in this study, the rate was calculated from the Hertz-Knudsen equation (Equation 5.5) derived from the kinetic theory of gases [141].

$$\dot{R} = \frac{\lambda A_{int} (p_{sat} - p)}{\sqrt{2\pi R_g T_{int}}}, \quad A_{int} = n * 4\pi r^2 \quad (5.5)$$

where  $R_g$  and  $T_{int}$  are the ideal-gas constant and the bubble-interphase temperature respectively, while  $A_{int}$  is the overall vapour interface surface area, which is calculated assuming a nucleation-site density  $n = 10^{16} \text{ sites/m}^3$  and a bubble radius of  $r = 10^{-6} \text{ m}$ . The nucleation site density was calibrated based on the maximum spray cone angle, while the bubble radius has been deemed representative of flashing-flow propagation in

different benchmark geometries. In fact, along with an accommodation coefficient value of  $\lambda = 1.0$ , they are indicative of thermodynamic conditions approaching equilibrium [4]. Since a mixture model is employed, the interphase temperature is taken as equal to the local grid cell temperature provided by the solution of the energy equation. The degree of deviation from thermodynamic equilibrium is reflected in the value of the accommodation coefficient  $\lambda$ . Values of either 1.0 or 0.1 correspond to conditions similar to thermodynamic equilibrium and strongly deviating from it, respectively [33]. The capability of the Knudsen-based mass-transfer model to capture the phase-change rate in flashing flows has been demonstrated in [4] and has also been implemented in CFD software [111] in order to investigate flash boiling in gasoline fuel injector nozzles.

### 5.2.2 Helmholtz energy equation of state

LOx and LN<sub>2</sub> thermodynamic properties required by the density-based solver are derived from the Helmholtz energy EOS. The table containing the LOx properties is calibrated within the temperature range  $54.4\text{ K} \leq T \leq 500.0\text{ K}$ , for a maximum density of  $\rho_{max} = 1400.5\text{ kg/m}^3$ . For LN<sub>2</sub> the thermodynamic properties are tabulated for a temperature range of  $63.2\text{ K} \leq T \leq 329.8\text{ K}$ , for a maximum density value of  $\rho_{max} = 1100.0\text{ kg/m}^3$ . The properties are organised into a thermodynamic table that may include a wider or narrower range of values, depending on the application. The dimensionless form of the aforementioned EOS for the Helmholtz energy  $a$ , having as independent variables the density and the temperature [110] is presented in Equation 5.6.

$$\frac{a(r, T)}{RT} = \alpha(\delta, t) = \alpha^0(\delta, \tau) + \alpha^r(\delta, \tau) \quad (5.6)$$

where  $\delta = \rho/\rho_c$ ,  $\tau = T_c/T$ ,  $\alpha^0$  is the dimensionless Helmholtz energy of the ideal gas and  $\alpha^r$  is the residual Helmholtz energy. The last two variables,  $\alpha^0$  and  $\alpha^r$ , can be determined as reported by Kyriazis et al. in [105]. Equation 5.6 can then be used to determine pressure, internal energy, enthalpy and speed of sound of the fluid as a function of density and temperature. The saturation curve is identified using Maxwell's criterion. Properties within the saturation dome, are determined using a mixture assumption and the mixture's speed of sound is calculated using the Wallis speed-of-sound formula [33].

Due to the considerable computational cost that solving the Helmholtz EOS at each time step entails, a tabulated-data technique, similar to the one proposed in [145]

has been employed. The procedure and table development has been performed for each substance of interest. Two structured thermodynamic grids of approximately  $10 \times 10^4$  and  $7 \times 10^4$  elements have been created, one for each working fluid, namely LOx and LN<sub>2</sub>, containing information for all the thermodynamic properties on each thermodynamic node defined by a density and internal energy value. For LOx cases, the density range of the grid is  $0.125 \leq \rho \leq 1400.5 \text{ kg/m}^3$  divided into 251 points of fixed  $\Delta\rho = 5.055 \text{ kg/m}^3$ , while the internal-energy range of the grid is  $-171.14 \leq e \leq 165.51 \text{ kJ/kg}$  divided into 400 points of fixed  $\Delta e = 0.84161 \text{ kJ/kg}$ . For LN<sub>2</sub> cases, the density range of the grid is  $0.01 \leq \rho \leq 1100.01 \text{ kg/m}^3$  divided into 221 points of fixed  $\Delta\rho = 5.0 \text{ kg/m}^3$ , while the internal-energy range of the grid is  $-169.50 \leq e \leq 129.5 \text{ kJ/kg}$  divided into 300 points of fixed  $\Delta e = 1.0 \text{ kJ/kg}$ . The variation of pressure and internal energy of nitrogen as a function of density and temperature is presented in Figure 5.1. The surfaces have been produced by employing the aforementioned tabulating procedure. The saturation curves are represented as black dashed lines.

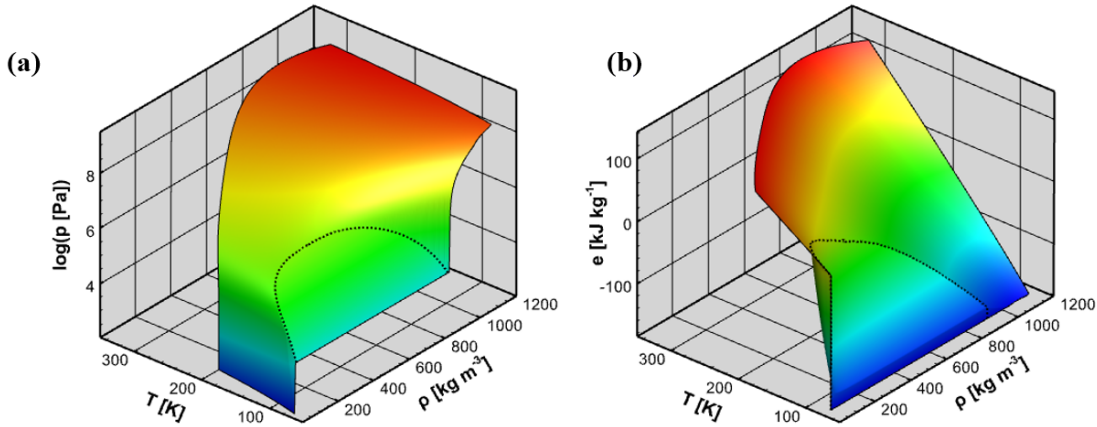


**Figure 5.1:** Three-dimensional phase diagrams for nitrogen: (a) pressure and (b) internal energy in terms of density and temperature.

Once density and internal energy are calculated by the URANS equations, the corresponding element of the thermodynamic table is identified through numerical inversion from the above quantities. Any thermodynamic property  $\phi$  of the table is then approximated by a finite element bilinear interpolation as described in Equation 5.7.

$$\phi(\rho, e) = \sum_n^{nodes} N_n(\rho, e)b_n \quad (5.7)$$

where  $\phi$  corresponds to pressure, temperature or speed of sound, required for the calculation of the fluxes in the density-based solver. Full details on the shape functions

$N$  employed and the calculations of unknowns  $b$  on each node  $n$  are reported in [105].

### 5.2.3 Turbulence closure

All the simulated cases are characterized by high Reynolds numbers ranging from  $8.7 \times 10^7$  to  $16.2 \times 10^7$ . The flow of cryogenic fluids developing through the selected orifices has therefore been found to be within the turbulent regime for all cases. For the calculation of Reynolds numbers, the diameter of each orifice was used as the characteristic length scale, while an approximation of the velocity was made based on experimental values of the mass flow rate. Finally, liquid phase properties at the injection pressure and temperature have been assumed for the Reynolds calculations. To account for contributions to the viscosity,  $\mu$  and thermal conductivity  $k$  due to turbulence effects, the  $k - \omega$  Shear Stress Transport (SST) turbulence model was employed since the specific turbulence model has been demonstrated to perform well in highly turbulent wall-bounded flows, where secondary flow is also possible to arise. More specifically, the SST formulation exhibits a  $k - \epsilon$  behaviour in the free-stream without suffering from excessive turbulence production in regions of recirculation [87]. The model is suitable for adverse pressure gradients that are present near the injector's exit hole [88] and has performed better than the  $k - \epsilon$  regarding mass flow results in the context of superheated nozzle flows [133]. Standard wall functions were utilised for near-wall turbulence treatment. The respective  $y+$  values for the numerical grid employed for the simulations were of the order of 10.

### 5.2.4 Domain discretisation

Two geometries are represented in this study referred to as injector A and injector B. Injector A is a typical cylindrical LOx injector of 0.36 mm length and constant diameter of 0.30 mm and presented in Figure 5.2.a. The specific injector geometry has been used for obtaining the experimental data available from Lamanna et al [7]. Injector B is a cylindrical LN<sub>2</sub> injector of 2.9 mm length and a constant diameter of 1 mm, utilized in the experimental campaign of Rees et al. [8] and is presented in Figure 5.2.b.

Since both orifices are axisymmetric, both domains were reduced to a wedge produced by rotating the nozzle layout, around the symmetry axis by 50° as depicted in Figure 5.3. As can be seen in the same figure, the inflow section has been expanded upstream in both domains to impose the stagnation conditions of the experiments. After the grid independence study presented in Section 5.2.6, numerical grids of

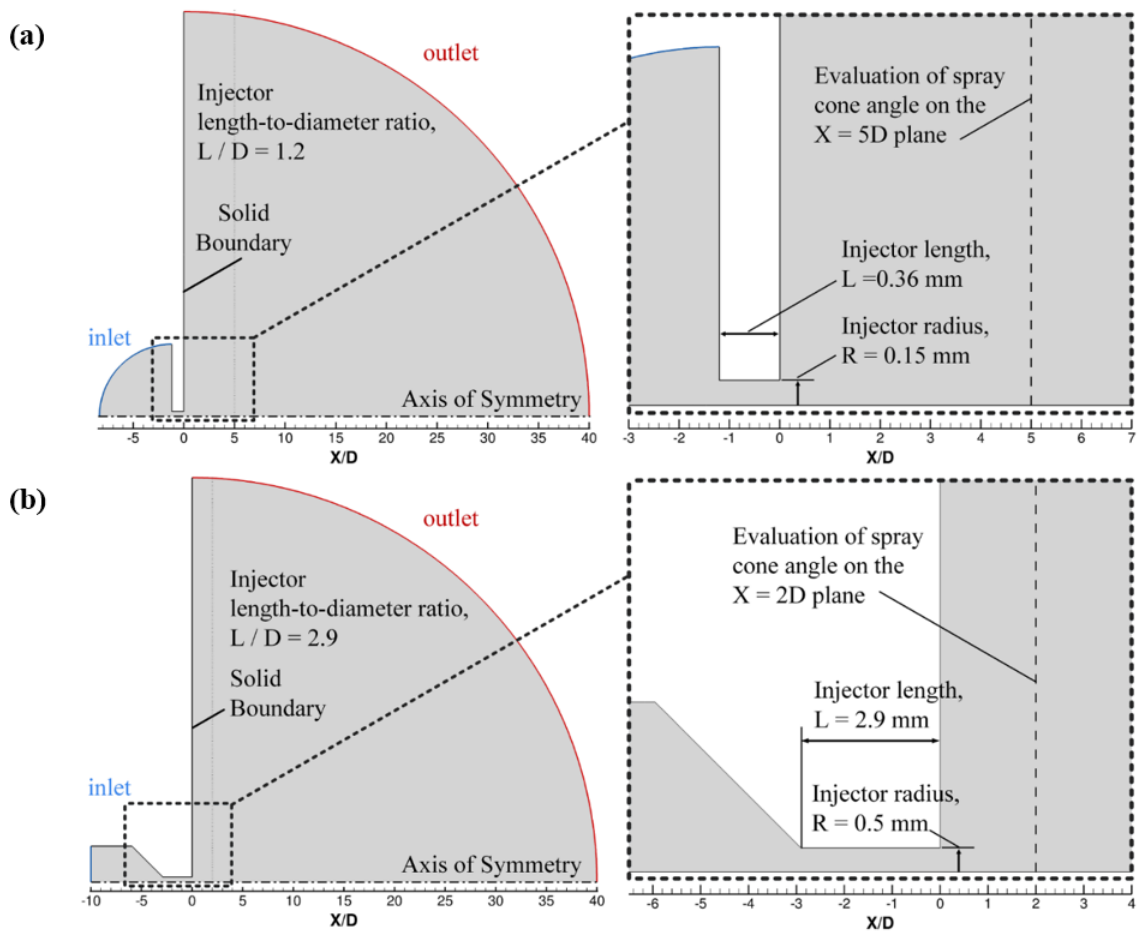


**Figure 5.2:** Geometry of (a) liquid oxygen injector (injector A) employed in [7] and (b) liquid nitrogen injector (injector B) employed in [8]. The panels represent the numerical domain used for the simulation. The outflow part extends downstream the injector exit to a length equal to 40 orifice diameters.

approximately 26,000 and 50,000 cells were employed to represent injectors A and B, respectively, with comparable cell density in the in-nozzle and spray-outlet regions for both geometries. The developed numerical grids were primarily structured comprising more than 97% hexahedral cells. Regarding the injector hole, the spatial discretisation for both injectors was 50 cells through the cross-section. The near-wall region in each case was refined with the use of 12 inflation layers with a growth factor of 1.2. The grids resulted in  $y+$  values of the order of 10, suitable for turbulence modelling using URANS.

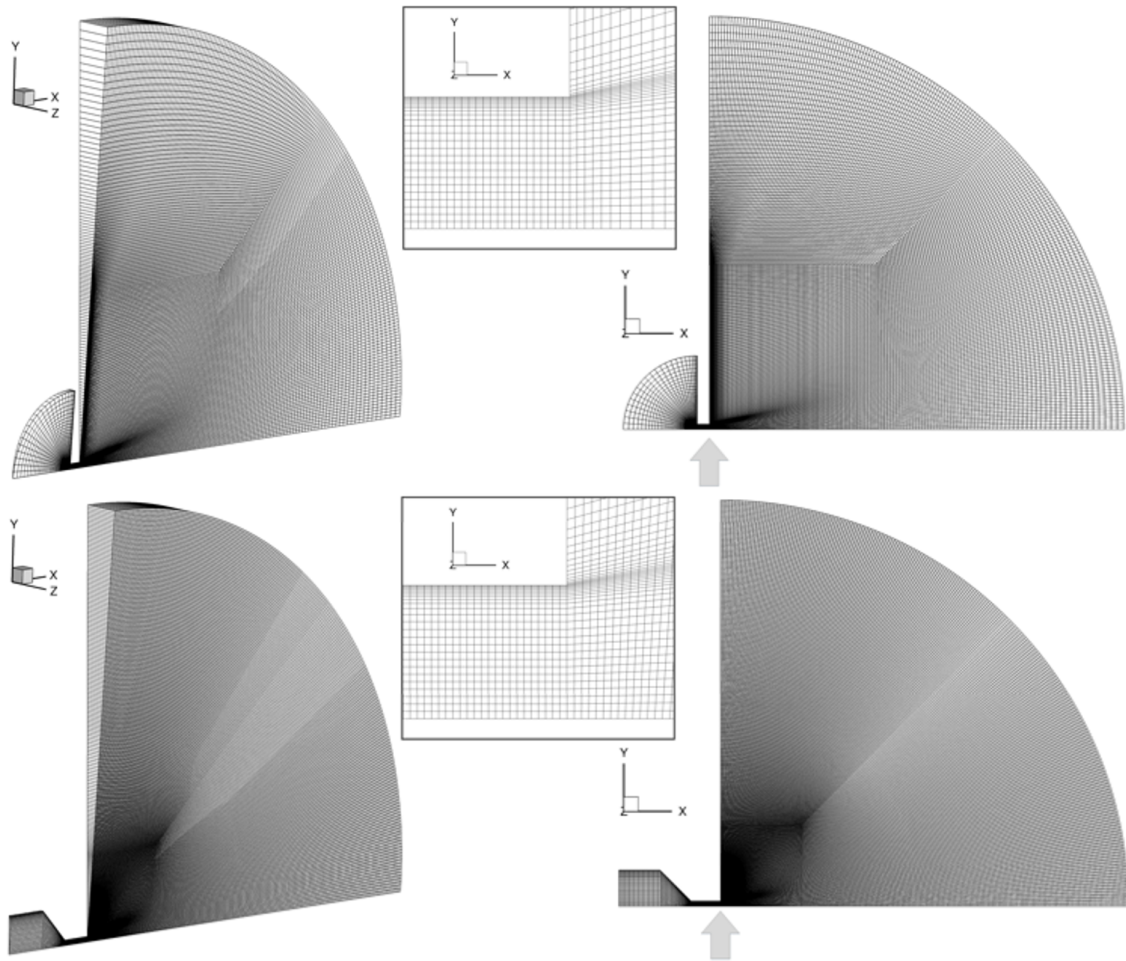


**Figure 5.3:** Views of the numerical grid of (a) the LOx injector and (b) the LN<sub>2</sub> injector including a focused view of the location marked with an arrow around the exit of each injector.

### 5.2.5 Boundary and initial conditions

The set of boundary conditions imposed in the examined cases replicate the physical conditions prevailing during the actual LOx and LN<sub>2</sub> experiments presented in [7] and [8]. Appropriate constant values of static pressure were imposed at the inlet and outlet of the domain in accordance with the experimental conditions. A zero-gradient condition was imposed for the boundary-normal velocity component at the inlet, while the remaining velocity components were set to zero. At the outlet boundary, zero-gradient boundary conditions were set for all velocity components and all the transported quantities. A no-slip condition was imposed on all the surfaces acting as orifice walls that were also treated as adiabatic. Regarding energy-conservation considerations, a constant temperature value in the case of the pressure-based solver

and a constant internal energy value in the case of the density-based solver were imposed on the domain inlet and outlet according to the equation formulations implemented in each solver.

Regarding initialization, in the cases of the pressure-based solver, a Laplace-based equation was solved to establish an initial pressure field while quiescent fluid was assumed at the initial time instance. For the density-based solver, a solution produced by the SIMPLE solver was used for the initialization of the pressure and velocity fields. All simulations were initialized assuming pure liquid in the inlet and nozzle volume, while the gas phase was assumed to fill the downstream volume. Finally, temperature values were set equal to the respective inlet values throughout the domain. Table 5.1 summarizes the set of boundary and initial conditions applied to all examined cases.

**Table 5.1:** Summary of boundary and initial conditions imposed for the numerical simulations.

Boundary Conditions	Inlet	Outlet	Wall
Pressure-based	$p = p_{in}, T = T_{in}$	$p = p_{out}, T = T_{out}$	$\vec{u} = 0$ $\partial T / \partial n = 0$
Density-based	$p = p_{in}, e = e_{in}$	$p = p_{out}, e = e_{out}$	$\vec{u} = 0$ $\partial T / \partial n = 0$
Initial Conditions			
Both solvers	$T = T_{in}, \alpha_{inlet} = 0, \alpha_{orifice} = 0, \alpha_{outlet} = 1$		
Pressure-based	$p = p_0$	$\vec{u} = 0$	
Density-based	$p = p_0$	$\vec{u} = \vec{u}_0$	

### 5.2.6 Validation and grid independence

The pressure-based solver employing the Hertz-Knudsen phase-change model has been extensively validated for internal and external flashing flows considering water as the working medium in previous works of the authors [160, 4]. Specifically, the model has been demonstrated to accurately capture phase change in a converging-diverging nozzle, a (throttle) nozzle with an abrupt contraction and a rapidly depressurising duct (pipe blow-down). Furthermore, the density-based algorithm has been validated in previous works with reference to bubble- [105], and droplet-dynamics [151] simulations, while the accuracy of the tabulated technique based on the Helmholtz energy EOS has

been verified in reference to the properties of n-dodecane [105]. In a different study, an additional validation study was set up in order to further evaluate the capability of the density-based solver to capture LOx flows using the Helmholtz EOS thermodynamic closure. The relevant predictions are presented in detail in [160].

In order to ensure the independence of the URANS numerical solution from the density of the numerical grid, three different grids of increasing cell count were created to represent the geometry of injector A, consisting approximately of 10, 26 and  $107 \times 10^3$  cells. The pressure-based solver was utilized to simulate case 3 of Table 5.2 for the grid independence study, a case with high superheat where severe expansion and large spray cone angles were expected. The results produced by the three numerical grids are presented in Figure 5.4, in terms of pressure and vapour volume fraction distributions along the orifice symmetry axis.

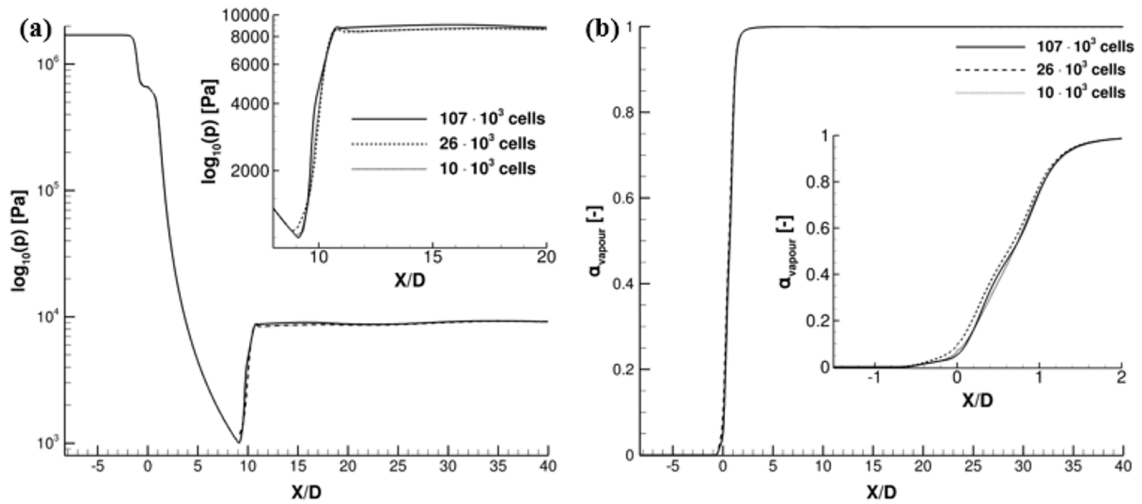


**Figure 5.4:** Grid independence analysis of the URANS numerical solution. (a) Pressure and (b) vapour volume fraction distributions on the orifice symmetry axis for three numerical grids of increasing cell number.

Due to the fact that the resulting flow field reaches quasi-steady state conditions, the flow variables are time-averaged over a period of 20 milliseconds, initiating after an initial transient period of around 4 ms. The results presented in Figure 5.4 reveal that all used grids can qualitatively capture the overall flow characteristics. The intermediate grid has been adopted for all following simulations, as the results produced with said grid were of comparable accuracy to those of the dense grid, with negligible discrepancies, yet with reduced computational load. A numerical grid of similar topology consisting of 51,856 cells has been employed for Injector B, with comparable cell density both in in-nozzle and spray regions.

### 5.3 Results

The test cases examined in this study are summarized in [Table 5.2](#). Specifically, cases 1 to 4 refer to LOx flow and correspond to the experimental conditions and the resulting spray cone angles reported by Lamanna et al. [7], whereas cases 5 to 10 refer to LN<sub>2</sub> flow and specifically the experimental campaign of Rees et al. [8] for which data regarding mass flow rates and spray cone angles are available.

**Table 5.2:** List of examined test cases, including the operating fluid, boundary conditions and superheat  $R_p = p_{sat}(T_{in})/p_{out}$  for each case.

Case	Fluid	$p_{in} \cdot 10^5$ [Pa]	$p_{out}$ [Pa]	$T_{in}$ [K]	Superheat $R_p$ [-]
1	LOx	17	20600	113.0	33
2		17	14140	113.0	48
3		17	9100	113.0	74
4		17	2750	113.0	245
5	LN <sub>2</sub>	8	58020	82.5	3
6		8	24870	82.5	7
7		8	6130	82.5	28.4
8		4	58020	82.5	3
9		4	24870	82.5	7
10		4	3330	82.5	52.3

The rationale for selecting the aforementioned cases was to test the applicability of the methodologies presented in this study for a wide range of boundary conditions and for two different cryogenic fluids. Moreover, the juxtaposition of the results from specific cases provided useful insight into the flash evaporation process. Transient simulations have been performed for all cases, yet it was confirmed that the respective flow and temperature fields reached to steady-state (or quasi-steady-state) solutions in all cases; thus, the time-averaged flow and temperature fields are presented.

Due to the fact that the tested temperature and pressure conditions can lie below those of the triple point of LOx and LN<sub>2</sub>, there is indeed a possibility of solidification of the operating fluids. Nevertheless, in the work of Lamanna et al. [7] (cases 1 to 4 of [Table 5.2](#)), no reports of solidified LOx are found. In the case of fully-flashing LN<sub>2</sub>

sprays of Rees et al. [8] (cases 7 and 10 of Table 5.2) flakes of solidified nitrogen were indeed observed close to the walls of the vacuum chamber and therefore away from the active visualisation region. Since the current investigation is mainly oriented towards aerospace applications, where icing is to be avoided, a simple limiter was set in the energy equation to avoid temperatures below solidification. It was confirmed that this limiter did not interfere with the robustness and accuracy of the solution process.

### 5.3.1 Liquid Oxygen flashing flow

The numerical results corresponding to cases 1 to 4 of Table 5.2 are discussed in this section. In this specific set of cases, LOx is used as the working fluid and the imposed boundary conditions are chosen to result in an increasing superheat. Experimental data are available for comparison from the experimental campaign of Lamanna et al. [7] where the spray cone angle of flashing LOx was measured at a distance equivalent to 5 nozzle diameters downstream of the nozzle's exit.

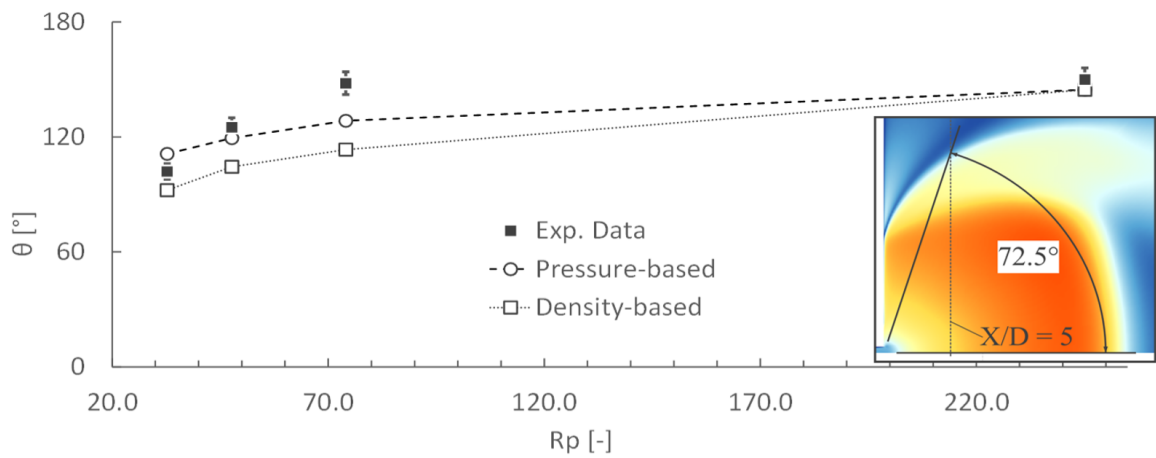


**Figure 5.5:** Oxygen spray cone angle for inlet pressure of 17 bar and variable LOx injection conditions of increasing superheat degree. Conditions correspond to cases 1 to 4 of Table 5.2. Spray cone angles measured at a distance equivalent to 5 nozzle diameters downstream the nozzle (see figure inset).

Figure 5.5 summarizes the results produced by the two approaches and evaluates the predictive capability of the two methods in terms of spray cone angle, for superheat ranging from 33 to 245. In accordance with the experimental spray cone-angle measurements, the angle is measured at a distance equivalent to 5 nozzle diameters after the nozzle's exit, as can be seen in the inset of Figure 5.5. Since no manufacturing asymmetries or irregularities can be explicitly captured numerically, the numerical data only correspond to half of the diverging layout downstream of the injector outlet and

the angle value is then doubled. Figure 5 showcases the differences in the behaviour of the two algorithms in terms of phase-change modelling.

The Hertz-Knudsen phase change model can be calibrated to model flash evaporation for various degrees of superheat. In the literature, the model has been used for closed geometries and lower superheat with a nuclei density value of  $10^{13}$  and has produced accurate results [160]. In this numerical campaign, the model was properly calibrated based on the maximum spray cone angle parameter in order to qualitatively capture an intense flashing process, unrestricted by wall boundaries, and the bubble nuclei density was set to  $10^{16}$  for all examined cases. The second method employing a thermodynamic table with real-gas thermodynamic properties produces equally accurate results for high LOx superheat (case 4) while capturing the process with satisfactory accuracy for lower superheat ratios. The advantage of this method is that, after the initial table of fluid properties has been created for a range of conditions, no calibration is needed, since the phase change rates are dictated by the tabulated real-gas thermodynamics. Therefore, between this numerical campaign and the LOx campaign presented in [160], no changes were needed in terms of the thermodynamic table used, which demonstrates the applicability of the specific approach regardless of the boundary conditions or the geometry used.

Figure 5.6 presents a comparison between the two approaches in terms of pressure, velocity, density and temperature fields for a case of  $R_p = 245$ . Comparing the pressure fields (Figure 5.6.a), the two approaches are in good agreement, as it is clear that the pressure decreases in a similar manner. The velocity, density and temperature contour plots reveal the formation of bell-shaped Oxygen spray with an almost identical spray cone angle on the measurement location ( $X[m] = 5 \times$  Nozzle diameter). Although the pressure decrease that takes place is similar for both approaches, the use of tabulated thermodynamics with the density-based solver imposes an infinite phase-change rate that affects the temperature ranges of the expanding flow after the nozzle exit (Figure 5.6.d). The thermal equilibrium model predicts, therefore, the presence of an area of lower temperature and comparable but slightly higher density (Figure 5.6.c) than the Hertz-Knudsen model. Those changes in the density affect the maximum velocity that the expanding flow reaches (Figure 5.6.b), before decelerating and adjusting to the ambient pressure with a steep gradient. The evolution of the field-variables values along the axis of symmetry further supports the aforementioned findings and is presented in Figure 5.7.

The comparison between the thermal non-equilibrium, pressure-based solver curve,  $R_p = 245(PB)$ , and the HEM, density-based solver curve,  $R_p = 245(DB)$ , in Figure 5.7

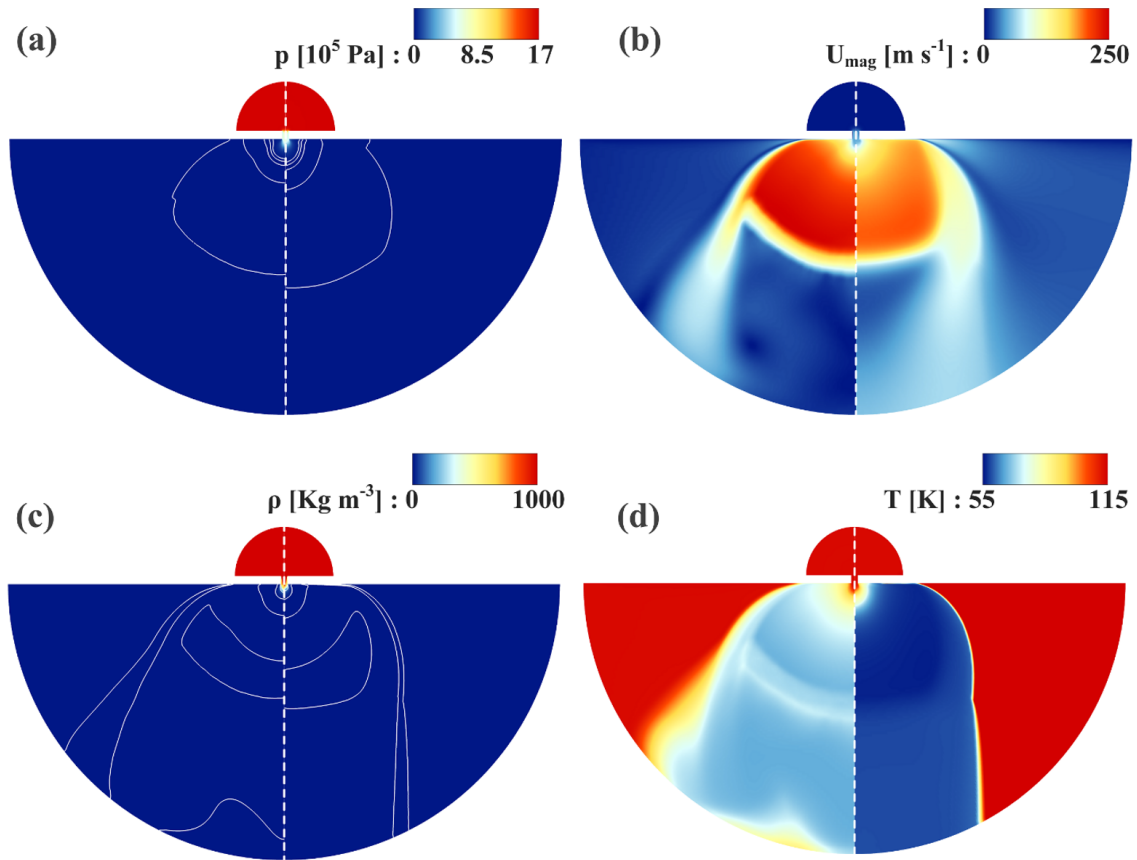


**Figure 5.6:** Contour plots of (a) Pressure, (b) Velocity magnitude, (c) Density and (d) Temperature variable distribution for cases 4 of Table 5.2. Pressure based solver results are presented on the left of each subplot while density based solver results are on the right.

reveals the characteristic features of the flash evaporation process and the differences between the two approaches. For those curves, the pressure and velocity fields (Figure 5.7.a and Figure 5.7.b) share the location where the minimum and maximum values are reached, approximately 15 nozzle diameters downstream of the nozzle exit. Regarding the thermal non-equilibrium model, the pressure decreases in a marginally steeper fashion and the maximum velocity value is almost 25% greater in comparison to the HEM. This difference in maximum velocity values emanates, predominantly, from the density field (Figure 5.7.c), which adjusts the speed of sound in the orifice. Regarding the temperature fields (Figure 5.7.d), the phase change mechanisms play a key role in the behaviour of the quantity. In the case of the tabulated HEM approach, higher (infinite) phase change rates lead to higher energy absorption which results in lower temperatures.

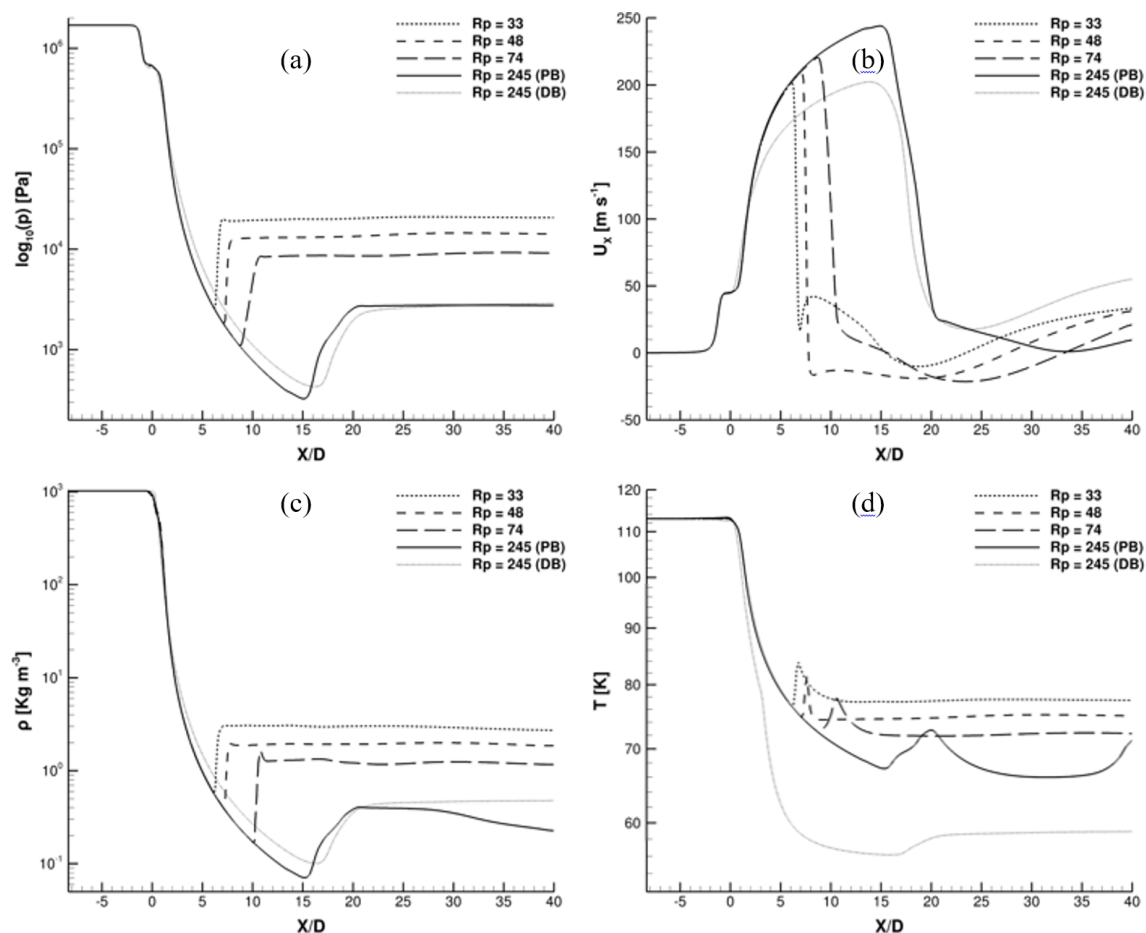


**Figure 5.7:** Distribution of (a) Pressure, (b) Axial Velocity, (c) Density and (d) Temperature along the nozzle axis of symmetry as predicted by the two approaches for case 4 of Table 5.2 and as predicted by the thermal non-equilibrium model of the pressure-based solver for cases 1 to 3 of Table 5.2.

Examining the results of Figure 5.7 in terms of increasing superheat ( $R_p = 33, 48, 74$  and  $245(PB)$ ), reveals that the pressure and density fields (Figure 5.7.a and Figure 5.7.c) are exhibiting similar variations after the nozzle exit. A step initial decrease is observed after the  $X/D = 0$  point and an equally sharp gain that reinstates the variable value to match a final equilibrium value. The higher the superheat level, the further from the nozzle exit the increase of pressure and density will take place, and the lower the equilibrium value will be. Temperature profiles (Figure 5.7.d), reveal their decrease due to the intense evaporation process and the absorption of latent heat. On the location where the flow expansion stops, a static (over time) shockwave is formed; an amount of vapour undergoes condensation, and a local increase in the temperature is observed. Finally, regarding the axial velocity (Figure 5.7.b), a flow-recirculation

region can be discerned for the cases of lower superheat (cases 1 to 3), as negative axial velocity values prevail between approximately 10 to 15 nozzle diameter lengths past the location of the injector exit. The recirculation can be attributed to shear forces from the flow surrounding the spray core. For the cases of higher superheat, the expansion is more extended and the surrounding flow is located further away from the spray axis, thus limiting the shear effects on the axial velocity value over the symmetry axis.

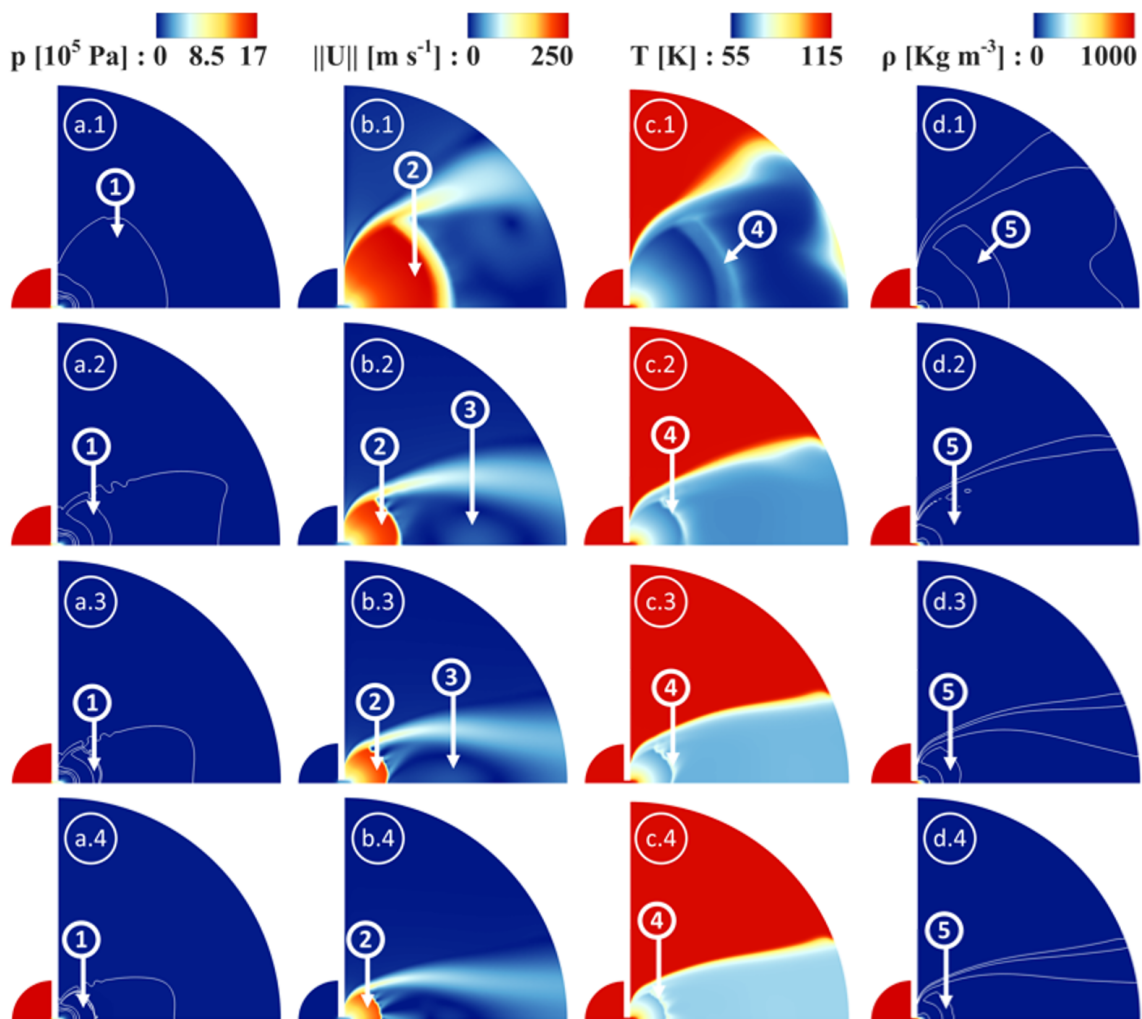


**Figure 5.8:** Contour plots of (Column a) Pressure, (Column b) Velocity magnitude, (Column c) Temperature and (Column d) Density variable distribution for cases 1 to 4 of Table 5.2. Each case is presented in a separate row. All variables are time-averaged.

Figure 5.8 presents contour plots of the flow and temperature fields for cases 1 to 4 of Table 5.2 in a manner of increasing superheat level. Distinct topologies common for all cases can be identified. Regarding the pressure field (Figure 5.8.a) a hemispherical volume of steep pressure gradients forms immediately after the nozzle exit, followed

by a region (Marker “1”) where pressure obtains values lower than the outlet pressure. This particular area becomes more extensive with increasing superheat ratio. For instance, for  $R_p = 245$ , it reaches up to a length of 20 nozzle diameters downstream of the nozzle exit. Likewise, the velocity field (Figure 5.8.b) reveals a hemispherical zone of fluid acceleration, or, in other words, flow expansion (Marker “2”), where supersonic velocity values are reached. The expansion stops at the location where pressure recovers in an abrupt manner, i.e. a shockwave forms. From an overall-topology standpoint, a bell-shaped spray forms that encloses the annotated areas. The flow velocity at the boundaries of the spray is higher than the core where recirculation zones (Marker “3”) form in the wake that is created downstream of the pressure discontinuity due to shearing induced by the high-velocity periphery. Besides, the density field (Figure 5.8.c) closely follows the pressure field, with the regions of low fluid density (Marker “4”) corresponding to regions of low pressure as well. The proximity to the injector’s outlet of this low-density/low-pressure location (Markers “1” and “4”) is a function of superheat. The higher the superheat, the further from the injector’s exit is the density/pressure minima located. Finally, temperature decreases within the spray area (Figure 5.8.d), as expected due to the evaporation of LOx and the absorption of latent heat. The higher the  $R_p$  the lower the minimum temperature. For all cases, there is a region where temperature briefly increases as condensation takes place after the pressure recovery (Marker “5”).

### 5.3.2 Liquid Nitrogen flashing flow

The numerical results corresponding to cases 5 to 10 of Table 5.2 are discussed in this section. In the specific set of cases, LN<sub>2</sub> is used as the working fluid and the imposed boundary conditions are chosen to result in an increasing superheat level for two values of inlet pressure. Experimental data are available for comparison from the campaign of Rees et al. [8], where in-nozzle mass flow rates and spray cone angles of flashing LN<sub>2</sub> were measured. Table 5.4 presents the comparison between the experimental measurements and the numerical data produced using the two solvers tested. As can be seen, good agreement between experiments and predictions has been achieved, with the HEM approach outperforming the respective kinetic-theory-based, thermal non-equilibrium model in terms of accuracy owing to its independence from tuning parameters.

Figure 5.9 summarizes the results produced with the two approaches and their predictive capability is evaluated in terms of spray cone angle, for two different values of inlet pressure, namely 8 (Figure 5.9.a) and 4 bar (Figure 5.9.b), respectively. As

**Table 5.4:** Comparison between numerical predictions and experimental measurements for LN<sub>2</sub> mass flow rate in injector B.

Mass-flow rate [kg/m <sup>3</sup> ]	Cases 5,6,7	Cases 8,9,10
Experimental	0.017 (±0.0005)	0.0097 (±0.0001)
Non-equilibrium (pressure-based)	0.01859	0.01141
Equilibrium (density-based)	0.01713	0.01058

demonstrated by [Figure 5.9.a](#), both numerical methods exhibit high accuracy in terms of spray cone angle for cases of higher inlet pressure (5 to 7 of [Table 5.2](#)). For the lower inlet-pressure counterparts (cases 8 to 10 of [Table 5.2](#)) the numerical results match perfectly the experimental values of the spray-cone angle for a high level of superheat. For  $R_p = 7$  both methods seem to underestimate the cone angle while for  $R_p = 3$ , only the HEM (tabulated) approach underestimates the angle of the spray cone as [Figure 5.9.b](#) suggests. What becomes apparent from the comparison between the high and low inlet-pressure data is that the discrepancies between numerical predictions and experiments do not exhibit any particular trend dependent on the superheat value. For instance, case 6 and case 9 share the same value of  $R_p = 7$ , yet the level of solver accuracy differs and hence the underlying cause should be sought in delicate features inherent to flash boiling such as the degree of liquid metastability and the complementary influence of transient processes that cannot be captured in full [18], especially by the density-based solver where thermodynamic equilibrium is postulated.

[Figure 5.10](#) presents, in a comparative manner between the two solvers, the distribution of characteristic quantities along the axis of symmetry, for the two inlet-pressure values examined. The comparison reveals differences between the two methods, along with advantages and limitations. To distinguish between the presented curves, a solid line has been used for the 4-bar-inlet cases and a dotted line for the 8-bar-inlet. Varying superheat levels result in different curves each marked with coloured points that, depending on the variable, may indicate the location of a local minimum/maximum.

To further elucidate distinct features of the flow expansion, four regions have been marked in [Figure 5.10](#). Marker “1”, points to the nozzle exit ( $X/D = 0$ ) region, with pressure being the variable of interest. The pressure-based solver (realising a mass-transfer-based modelling approach) predicts a region immediately downstream of the exit of the nozzle where the pressure remains unchanged ([Figure 5.10.a](#), left panel),

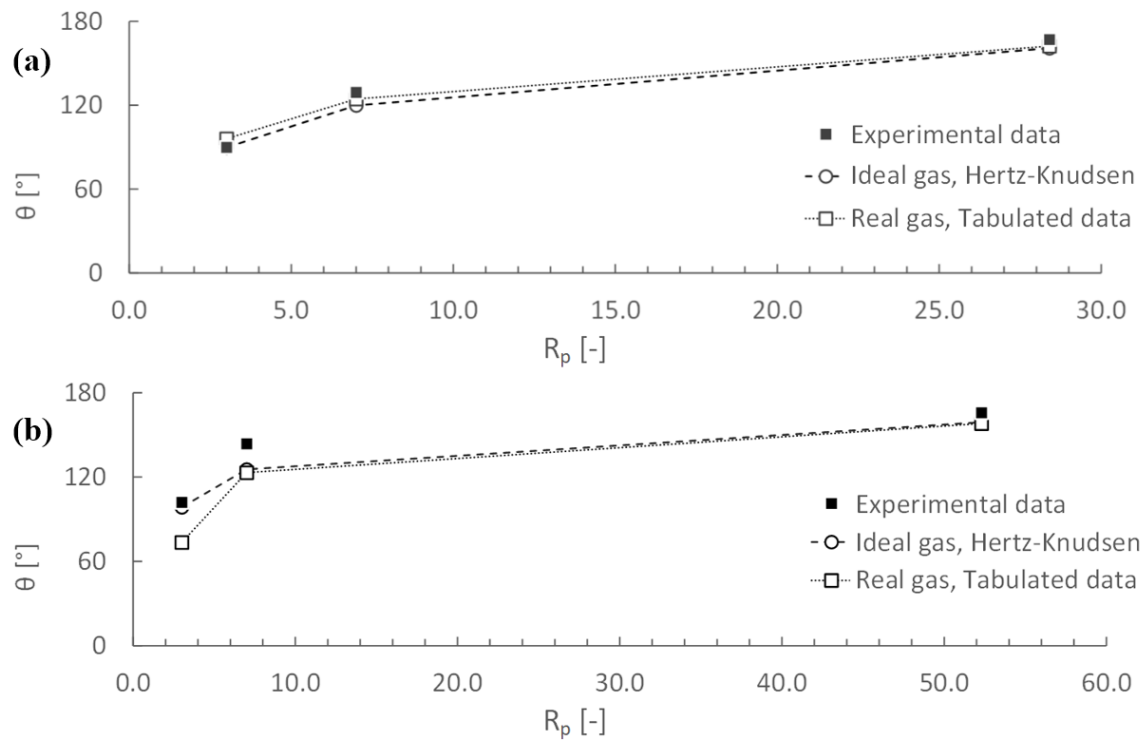


**Figure 5.9:** Nitrogen spray cone angle for inlet pressure of 8 bar and variable LN<sub>2</sub> injection conditions of increasing superheat degree. Conditions correspond to cases 5 to 7 of Table 5.2. Spray cone angles are measured at a distance equivalent to 2 nozzle diameters downstream the nozzle exit.

suggesting the presence of a liquid core as also demonstrated by the constant density values in the region (Figure 5.10.c, left panel). On the contrary, the density-based (tabulated-thermodynamics-HEM) solver predicts an almost instant phase-change response of the fluid (Figure 5.10.c, right panel) to pressure change, also correlated to pressure fluctuations in the outlet region, refer to Marker “1” on the right-hand side panel of Figure 5.10.a. This behaviour is expected due to the infinite phase-change rate replicated through the use of the equation of state.

Regarding flow velocity presented in Figure 5.10.b, the pressure-based solver predicts a steeper increase, i.e. a more violent flow expansion, reaching a higher maximum velocity value (Marker “2”) compared to the density-based solver. This behaviour is attributed to the sonic velocity that, in essence, adjusts the flow velocity within the nozzle and is dependent on the phase-change rate, as it is designated by the two-phase mixture composition with lower sonic velocities obtained for bubbly mixtures. The density distribution along the axial coordinate at the nozzle symmetry axis (Figure 5.10.c) reveals that in the case of the pressure-based solver for different  $R_p$

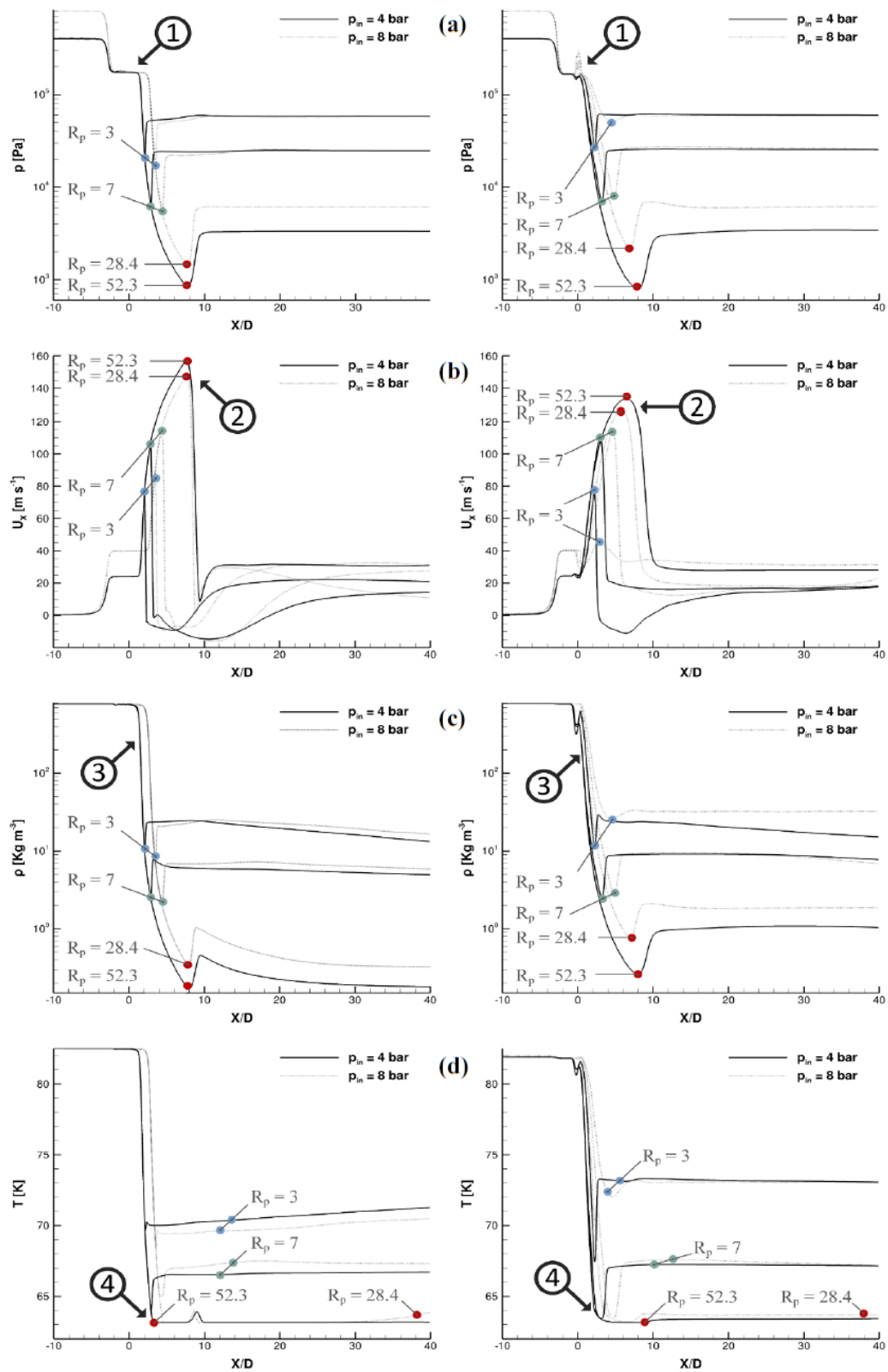


**Figure 5.10:** Time-averaged values resulting from the use of a pressure-based solver with a thermal non-equilibrium model (left) and a density-based solver utilizing a HEM (right). Distribution of (a) Pressure, (b) Axial Velocity, (c) Density and (d) Temperature along the nozzle axis of symmetry for cases 5 to 10 of Table 5.2.

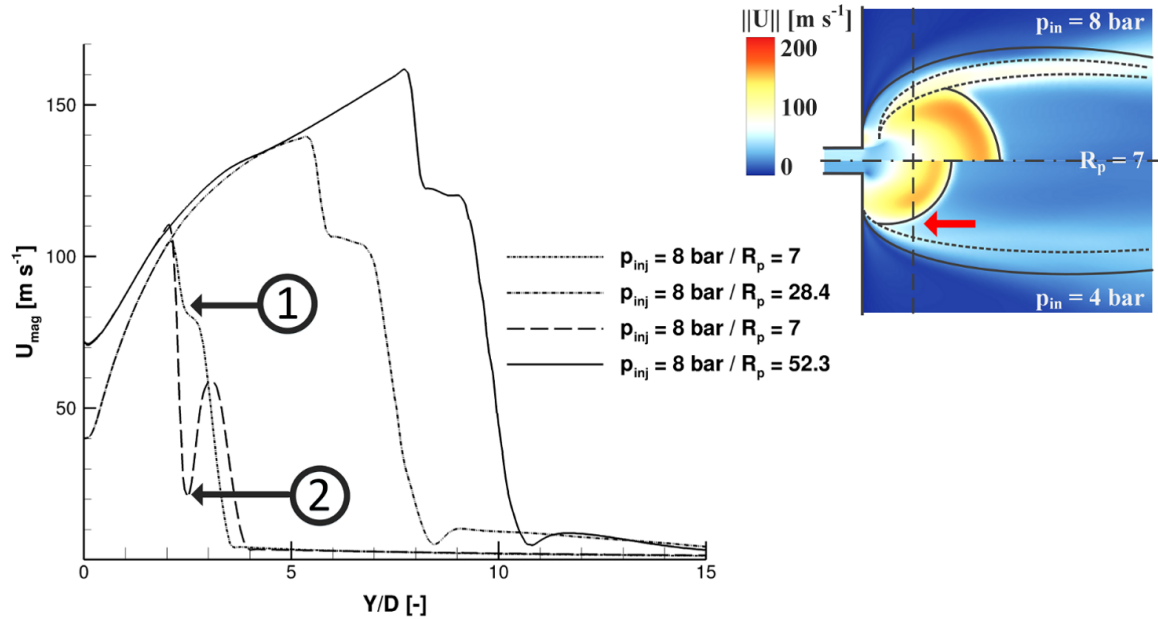
values, phase change evolves in an identical, gradual manner, i.e. density distributions coincide (Marker “3”) until disrupted at the shockwave location. On the contrary, the density-based solver predictions on the right-hand side of the figure indicate an oscillating behaviour, potentially stemming from the averaging of a flapping pattern at the injector outlet since the density-based solver converges in a quasi-steady solution.

Finally, the temperature field is presented in [Figure 5.10.d](#). As expected, temperature decreases sharply once phase change commences due to the conversion of sensible to latent heat required for the formation of bubbles. A subsequent temperature readjustment occurs in the pure-gas region. It must be noted that due to the ideal-gas assumption adopted in the pressure-based solver, the minimum temperature in the domain had to be limited to the triple-point temperature ( $63.15K$ ), which, of course, constitutes a drawback of the thermodynamic-modelling approach. On the contrary, the density-based solver following a vapour-liquid equilibrium approach produces a physically accurate temperature field with the minimum temperature being approached asymptotically (Marker “4”).

[Figure 5.11](#) presents the radial velocity magnitude profiles of the expanding nitrogen flow as a function of the dimensionless cross-flow coordinate ( $Y/D$ ), calculated at a distance of two nozzle diameters ( $X/D = 2$ ) downstream the exit of the injection nozzle. The results for cases 6,7 and 9,10 of [Table 5.2](#) follow a common trend indicating a flow acceleration pattern indicative of an under-expanded jet. Starting from the symmetry axis, velocity increases gradually up to the spray periphery where vapour fraction values are higher and thus compressibility effects are more pronounced.

The flow velocity subsequently decreases due to shearing with stagnant ambient. For the cases examined, this velocity decrease shows either a monotonical, Marker “1”, or a non-monotonical trend, Marker “2”. This behaviour is indicative of the morphology of the expansion cone, which, in turn, if the same  $R_p$  value is maintained, is designated by the inlet pressure, as illustrated in the inset of [Figure 5.11](#). Increased inlet pressure (8 bar) shifts the bell-shaped, flow-acceleration region downstream while it also increases its extent so as to overlap with the high-velocity region of the jet periphery. On the contrary, for an inlet pressure of 4 bar, the wake region past the shockwave (red arrow in the inset) intervenes between the expansion cone and the radial high-velocity zones producing the characteristic oscillating behaviour highlighted by Marker “2”.

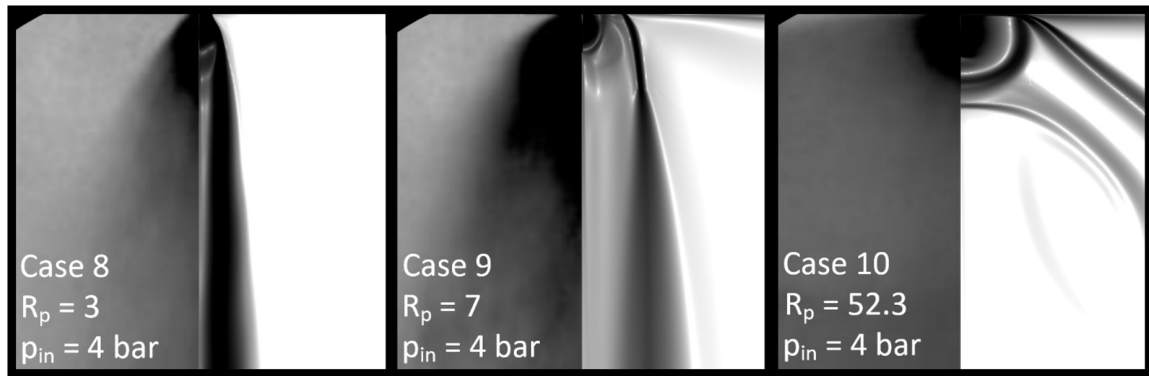
The experimental investigation of Rees et al. [8] provides, apart from spray cone angles and mass flow-rate measurements, shadowgraph images of the spray topology. To present a visual comparison between the experimental images and numerical results,



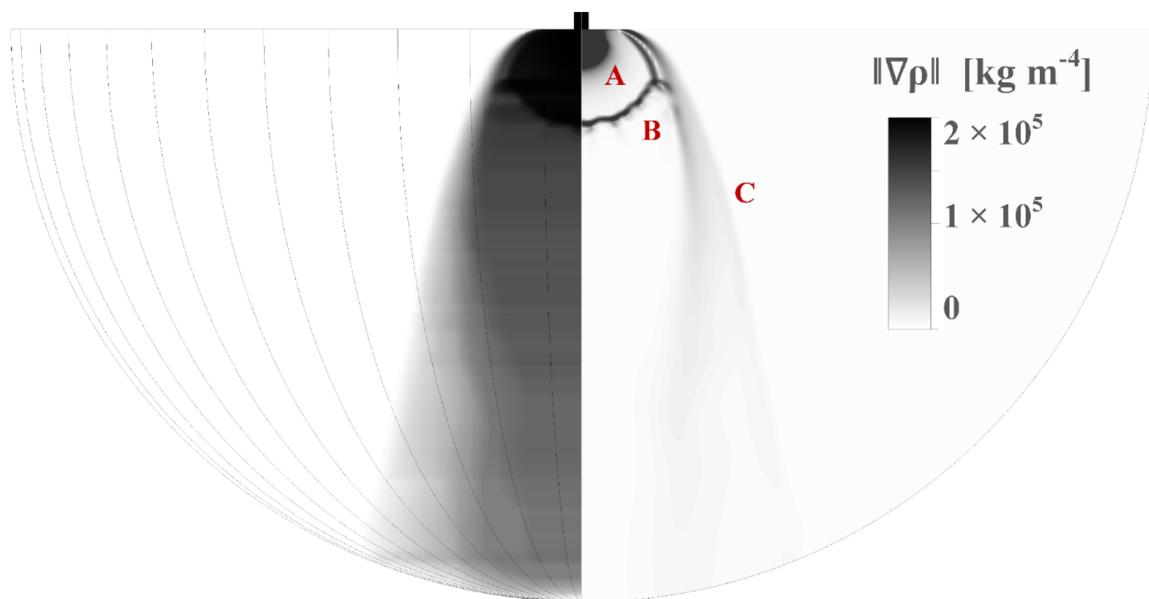
**Figure 5.11:** Velocity profiles for cases 6,7,9 and 10 of Table 5.2 at  $X/D = 2$  as a function of the dimensionless radial coordinate  $Y/D$ . Inset depicts velocity contour plots in the near-nozzle region of cases 6 (upper panel) and 9 (lower panel) of Table 5.2,  $R_p = 7$ .

Figure 5.12 has been compiled. For cases 8 to 10 of Table 5.2, experimental images are presented side-by-side with grayscale contours of the numerically-derived density gradient highlighting the locations of intense phase change. Although the numerical images constitute a slice of the spray, they do capture the spray topology resembling a bell-shaped hollow cone becoming more pronounced for increasing superheat, as demonstrated by the white, i.e. zero-gradient, regions around the axis of symmetry. The hemispherical region of steep gradients, which is abruptly terminated by the presence of the condensation shockwave is also reproduced accurately by the numerical results, as highlighted by the plots corresponding to the highest value of superheat. As can also be discerned, the spray cone becomes tangential to the nozzle outlet solid surface for high superheat values.

Complementary to Figure 5.12, an illustration of the three-dimensional spray topology is presented in Figure 5.13, resulting from a  $180^\circ$  revolution of a contour plot (produced for case 3) similar to those presented in Figure 5.12. Since the experimental visualization technique is based on refractive index gradients, i.e. density changes, a density gradient iso-surface has been used to render the three-dimensional numerical spray representation. The slice contour plot on the right-hand side of Figure 5.13



**Figure 5.12:** Nitrogen injection, cases 8 to 10 of [Table 5.2](#). Comparison between shadowgraphy images as presented by Rees et. al [8] (left panel of each frame) and numerically derived results using the HEM, tabulated approach (right panel). Density gradient magnitude has been plotted using a logarithmic scale with a darker colour corresponding to higher gradients similar to the colour band of [Figure 5.13](#).



**Figure 5.13:** Rendering of three-dimensional spray topology by revolution of the density gradient contour (left). Density gradient contour plot (right). Numerical data correspond to case 3 of [Table 5.2](#),  $R_p = 74$ .

reveals distinct areas of steep density gradients, i.e. the expansion cone (region A), the shockwave location (region B) and the spray periphery (region C). By rotating this slice around the injector axis of symmetry, the topology shown on the left part of [Figure 5.13](#) is produced. As can be clearly seen, the resemblance with the qualitative experimental images of [Figure 5.12](#) is evident. The expansion-cone region directly

downstream of the outlet appears darker due to the vigorous phase change and the presence of a pressure discontinuity, while a thin halo stemming from the periphery of the spray shrouds the regions further downstream leading to milder refractive index gradients.

## 5.4 Concluding remarks

In this work, two-phase flashing flows of liquid oxygen and liquid nitrogen injected into near-vacuum conditions have been numerically investigated. For this purpose, a pressure- and a density-based solver with two different approaches regarding the imposed phase change rates and thermodynamics closure have been employed and their predictive capabilities have been evaluated. For the pressure-based solver, the departure from thermodynamic equilibrium during phase change has been taken into account via the implementation of a bubble-dynamics model employing the Hertz-Knudsen equation, whereas thermodynamic equilibrium has been adopted in the density-based solver. Tabulated data for the variation of the fluid thermodynamic properties have been derived by the Helmholtz energy equation of state and used for the density solver operation. All the numerical results were compared against experimental data available in the literature.

The comparison demonstrated that both employed methodologies are suitable for calculating the evolution of a cryogenic flow expansion, phase-change/flashing and spray atomisation with certain advantages and limitations based on the inherent formulation of each technique. The Hertz-Knudsen phase-change model must be calibrated in order to model flash evaporation for various degrees of superheat. Therefore, in order to produce accurate results, initial calibration data must be available. The use of a thermodynamic table with real-gas thermodynamic properties produces accurate results for high superheat values while capturing the process with satisfactory accuracy for lower values of superheat. The level of accuracy differs among cases for reasons that can be sought in features inherent to flash boiling such as liquid metastability effects and the influence of transient processes that cannot be captured in full, especially by the density-based solver where thermodynamic equilibrium is postulated. The inherent inability of the method to account for metastability effects can be identified as a limitation of the presented methodology. Metastability effects could become important in transient flashing processes, as in blowdown tubes. Yet, for cryogenic fluid injection, which occurs under steady conditions, the method is sufficiently accurate and presents the advantage that, after the initial table of fluid properties is created

for a range of conditions, no calibration is needed, unlike models based on a vapour-transport equation, since the phase change rate is dictated by the tabulated real-gas thermodynamics. Therefore, the tabulated approach can be utilized regardless of the boundary conditions or the geometry [179].

# CHAPTER 6

## Large eddy simulation of iso-Octane under flashing injection conditions

The numerical work presented in this chapter studies the flow of iso-octane through the ECN Spray G injector under flashing (Spray-G2) operating conditions [10] in the context of a large eddy simulation (LES) numerical approach. Section 6.1 includes a review of the experimental and numerical research that has been conducted in the field of spray formation of gasoline direct injection (GDI) engines, mostly focusing on the spray-G injector geometry. The numerical models that were utilized are presented in Section 6.2, while the relevant numerical results are discussed in Section 6.3. The conclusions of this investigation are presented in 6.4.

### 6.1 Introduction

The experimental and numerical research volume in the area of gasoline direct injection (GDI) engines, particularly on fuel injectors, is enormous. The automotive industry is continuously under regulatory pressure to decrease emissions and increase efficiency. Combustion efficiency is hugely influenced by the spray quality of the liquid fuel injected in the combustion chamber and the appearance of flash-boiling can improve or decrease the quality of fuel sprays [180]. For this reason, flash boiling of GDI engine injector sprays has risen to an important research area with continuous progress. Recent developments regarding multi-hole injectors are presented in the work of Lee et al. [181], an overview of the advancement in flash boiling atomisation research in the context of combustion applications can be found in the investigation of Li et al. [182], while a review of the studies regarding the effect of flash boiling on the spray of GDI injectors is presented by Chang et al. [183]. Relevant experimental investigations of multi-hole injectors are presented in the following paragraphs.

Guo et al. [184] investigated the spray characteristics of a five-hole gasoline direct injector for ambient pressure ranging from 0.5 to 10.0 bar and fuel injection temperature

from 20 to 80 °C. The morphology of the spray was captured using high-speed imaging and droplet dynamics were studied with the use of phase Doppler measurement technique. The authors report spray collapses in elevated ambient pressure and flashing conditions. Near-field spray collapse is observed at elevated ambient pressure and is attributed to the low-pressure areas created by the neighbouring high-speed jets. On the contrary, far-field collapse is taking place under flashing conditions as a result of the low-pressure areas created by the temperature drop and vapour condensation.

Diffusion back illumination (DBI) and Schlieren imaging scheme were used by Payri et al. [185] to capture the morphology of flash boiling sprays, formed with the use of an ECN Spray G injector. DBI was used for measuring the liquid component in the spray, while the vapour distribution was determined using Schlieren imaging. The imaging results showed the manifestation of spray collapse induced by the ambient pressure values. Spiccas et al. [186] also studied the 8-hole ECN Spray G fuel injector. High-speed particle image velocimetry was applied along a plane between plumes to study plume interaction and the possibility of spray collapse and was coupled with diffused back illumination and Mie-scatter techniques. The results show the formation of a recirculation zone that is initially limited between plumes. With the interaction of adjacent plumes, the gap closes and the spray collapse progresses.

Zhang et al. [187, 188] practised the laser-induced exciplex fluorescence (LIEF) method on the FB-DEMA-hexane combination, to quantify the liquid-vapour composition of flashing gasoline sprays. The measurements were taken for a multi-hole gasoline DI injector over a range of superheated conditions. The results showed that with increasing superheat degrees, individual plumes of the multi-hole injector collapse and their interaction forms a single solid plume. The collapse of the vapour phase was found to be more significant than that of the liquid phase. The vapour quantity increased linearly with the superheat degree. Finally, when the superheat level reaches the point where spray collapse appears, the vaporisation rate rises dramatically signalling the presence of flashing conditions.

Due to the fact that the work on flash-induced atomisation and spray formation can largely vary in terms of injector topologies, operating conditions or fuel properties, the adaption of well-established industry standards for performing any type of experimental or numerical research is necessary. To facilitate the collaboration among experimental and computational researchers in engine combustion, the National Technology and Engineering Solutions of Sandia (NTESS) operates the Engine Combustion Network (ECN) with the purpose of establishing an internet library of well-documented experiments that are appropriate for model validation and the

advancement of scientific understanding of combustion at conditions specific to engines, to provide a framework for collaborative comparisons of measured and modelled results and to identify priorities for further experimental and computational research [10]. Based on the geometries, meshes and datasets included in the ECN platform, a large number of numerical investigations have been reported. Investigations relevant to the ECN spray-G injector (6.2.2) are presented in the paragraphs that follow.

In a collaborative investigation focusing on the internal flow and the near nozzle flow of the ECN-Spray G injector, Mohapatra et al. [189] evaluated five different modelling approaches. All models were able to accurately predict the mass flow rate through the injector, however, the predictive capability regarding other features was varying. Regarding plume width and fuel mass distribution, the predictions showed a wide variation, while, all modelling approaches encountered difficulties regarding the prediction of fuel dispersion and jet velocity. Due to those predictive inaccuracies, the authors identify the need for improvement in the area of Eulerian modelling of dense fuel jets.

In the work of Moulai et al. [190] the ECN-Spray G eight-hole counterbore injector was computationally and experimentally studied under a variety of operating conditions. The effects of turbulence, cavitation, flash-boiling, compressibility, and the presence of non-condensable gases were taken into consideration. The authors presented three injection scenarios; submerged conditions, injection into a pressurized nitrogen atmosphere, and flashing conditions. Long-distance microscopy was used to visualise the resulting sprays. According to their findings, the discharge coefficient of the injector was consistent for all three scenarios. Regarding cavitation, the results showed the presence of vapour in a significant volume of the counterbore, suggesting that the counterbore further expands the two-phase fuel flow. Flash-boiling conditions were found to produce wide plume angles and large amounts of vapour were generated. However, the produced vapour represented a small amount of mass.

The work of Saha and co-workers on the modelling of GDI injectors is extensive. In a 2016 publication [191], the authors present a numerical study of a two-phase flow inside the ECN-Spray G nozzle. The needle lift has been considered fixed and the effects of turbulence, compressibility, and non-condensable gases have been included. Standard k– $\epsilon$  turbulence model was used for turbulence modelling and the Homogeneous relaxation model (HRM) coupled with a volume of fluid (VOF) scheme was used to capture the phase-change process for three sets of boundary conditions. Non-flashing and evaporative, non-flashing and non-evaporative, and flashing conditions were considered. The numerical results showed mass flow-rate

variation on a hole-to-hole basis under all operating conditions. Cavitation and flash-boiling were observed under the corresponding conditions. The authors comment on the need for a large numerical domain at the nozzle outlet and on the observation that volume averaging was more effective than mass averaging.

The influence of transient needle motion on the ECN spray G injector under non-flashing (spray G) and flashing (spray G2) conditions was numerically investigated by Baldwin et al. [192]. In-nozzle flow and near-field spray simulations were performed using a compressible Eulerian solver. Liquid, vapour, and non-condensable gas were considered and the homogeneous relaxation model (HRM) was used to account for phase change. Dynamic mesh motion was implemented using Laplacian smoothing, with a minimum needle lift of 5  $\mu\text{m}$ . The low needle lift resulted in vapour generation near the injector seat. The internal injector flow was found to include many transient and interacting vortices that affect the spray angle and produce fluctuations in mass flow rate. Finally, the authors report the formation of intermittent string flash-boiling.

The work of Gärtner et al. [193] focuses on the numerical investigation of spray collapse using a modified OpenFOAM solver. The ECN spray G2 conditions were examined and the results were compared to relevant experimental data. The study concludes that spray collapse behaviour, can not be described using the superheat ratio,  $R_p$ , that is used for the characterisation of flashing regimes. Moreover, the numerical findings show the formation of under-expanded vapour jets and shock structures that interact and can be assumed to cause the spray to collapse.

In a coupled Eulerian-Lagrangian approach, Mohan et al. [194] also investigated the ECN Spray-G geometry under non-flashing (Spray-G1) and flashing (Spray-G2) conditions. The homogeneous relaxation model (HRM) coupled with the volume of fluid (VOF) method was used for the Eulerian approach that provided the initial and boundary conditions of the Lagrangian spray simulations that used the blob injection model. The authors state that the applied methodology can be used as a method of determining the appropriate initial and boundary conditions for spray simulations in the case of limited experimental data availability, as the results show that it is capable of capturing the rate of injection, mass injected through each hole, discharge coefficient, average spray plume angle, and half cone angle with satisfactory accuracy. Another Eulerian-Lagrangian approach was made by Duronio et al. [195]. A flashing-spray breakup model was developed and embedded in the sprayDyMFoam OpenFOAM's Eulerian-Lagrangian solver and used to simulate the ECN Spray G injector under flash-boiling conditions. The results showed an overall good spray morphology representation, prediction of spray-collapse for strong flash boiling conditions and correct diameter

dimensions estimations when compared to experimental data.

It is clear from the literature that many different approaches have been used to represent the flashing spray formation in the area of GDI engine injectors, all of them being able to capture the phenomenon with different levels of accuracy, or by focusing on certain topologies of the spray. In the present work, methodologies that were used in chapters 4 and 5, i.e. tabulated thermodynamics and non-equilibrium bubble-dynamics-based phase-change-model are implemented in a large eddy simulation (LES) framework and the results are evaluated.

## 6.2 Methodology

For the work performed in this chapter, the compressible form of mass, momentum and energy equations are considered (Equations 6.1,6.2,6.3). A single-fluid mixture approach was implemented, with the mixture including three phases. Nitrogen is the primary phase that fills the outlet of the injector, while isooctane liquid and iso-octane vapour are the secondary phases. The liquid phase has been modelled using a real-fluid approach, employing tabulated thermodynamic data derived from the Helmholtz energy equation of state. The ideal gas assumption was made for the fuel vapour and the non-condensable nitrogen. Between the iso-octane liquid and vapour phases, mass transfer takes place through the implementation of a thermal non-equilibrium bubble-dynamics-based phase-change model as described in Section 3.4.

$$\frac{\partial(\rho_{mix})}{\partial t} + \nabla(\rho_{mix}\vec{u}) = 0 \quad (6.1)$$

$$\frac{\partial(\rho_{mix}\vec{u})}{\partial t} + \nabla(\rho_{mix}\vec{u}\vec{u}) = -\nabla p + \nabla[\mu_{mix}(\nabla\vec{u} + \nabla\vec{u}^T)] \quad (6.2)$$

$$\frac{\partial}{\partial t} \sum_{i=1}^3 (\alpha_i \rho_i E_i) + \nabla \sum_{i=1}^3 (\alpha_i \vec{u} (\rho_i E_i + p)) = \nabla(k_{mix} \nabla T), \quad E_i = h_i - \frac{p}{\rho_i} + \frac{u_i^2}{2} \quad (6.3)$$

### 6.2.1 Turbulence closure

To address the turbulence closure requirement, a Large Eddy Simulation (LES) approach has been selected for this investigation with the implementation of the wall-adapting local eddy-viscosity subgrid-scale (WALE) model [196]. The subgrid-scale

model employs the Boussinesq hypothesis and computes the subgrid-scale turbulent stresses from Equation 6.4.

$$\tau_{ij} - \frac{1}{3}\tau_{kk}\delta_{ij} = -2\mu_t\bar{S}_{ij} \quad (6.4)$$

where  $\mu_t$  is the subgrid-scale turbulent viscosity,  $\tau_{kk}$  is the isotropic part of the stress tensor and is not modelled and  $\bar{S}_{ij}$  is the tensor of rate of strain of the resolved scale as defined by Equation 6.5.

$$\bar{S}_{ij} \equiv \frac{1}{2} \left( \frac{\partial \bar{u}_i}{\partial x_j} + \frac{\partial \bar{u}_j}{\partial x_i} \right) \quad (6.5)$$

where  $\bar{u}$  is the mean velocity. According to the WALE model, the eddy viscosity,  $\mu_t$ , is modelled as described in Equation 6.6.

$$\mu_t = \rho L_s^2 \frac{\left( S_{ij}^d S_{ij}^d \right)^{3/2}}{\left( \bar{S}_{ij} \bar{S}_{ij} \right)^{5/2} + \left( S_{ij}^d S_{ij}^d \right)^{5/4}} \quad (6.6)$$

where  $L_s^2$  and  $S_{ij}^d$  are given by equations 6.7 and 6.8.

$$L_s = \min\left(\kappa d, C_w \Delta\right) \quad (6.7)$$

$$S_{ij}^d = \frac{1}{2} \left( \left( \frac{\partial \bar{u}_i}{\partial x_j} \right)^2 + \left( \frac{\partial \bar{u}_j}{\partial x_i} \right)^2 \right) - \frac{1}{3} \delta_{ij} \left( \frac{\partial \bar{u}_k}{\partial x_k} \right)^2 \quad (6.8)$$

where  $\kappa = 0.41$  is the von Karman constant,  $d$  is the distance to the nearest wall,  $C_w = 0.325$  and  $\Delta = V^{1/3}$  is the local grid scale computed based on  $V$ , the volume of the cell.

## 6.2.2 Injector geometry, boundary conditions and initialisation

The injector examined is the Spray-G eight-hole counterbore injector as defined by the database of the ECN [10], based on experimental measurements e.g. the work of Duke et al. [197], where a wide range of techniques were employed, including both X-ray and visible-light imaging. The injector's main characteristics are presented in Figure 6.1, while its nominal dimensions and relevant boundary conditions are presented on Tables 6.1 and 6.2. Regarding the spatial discretisation, Figure 6.2 presents the three-dimensional computational domain corresponding to the injector.

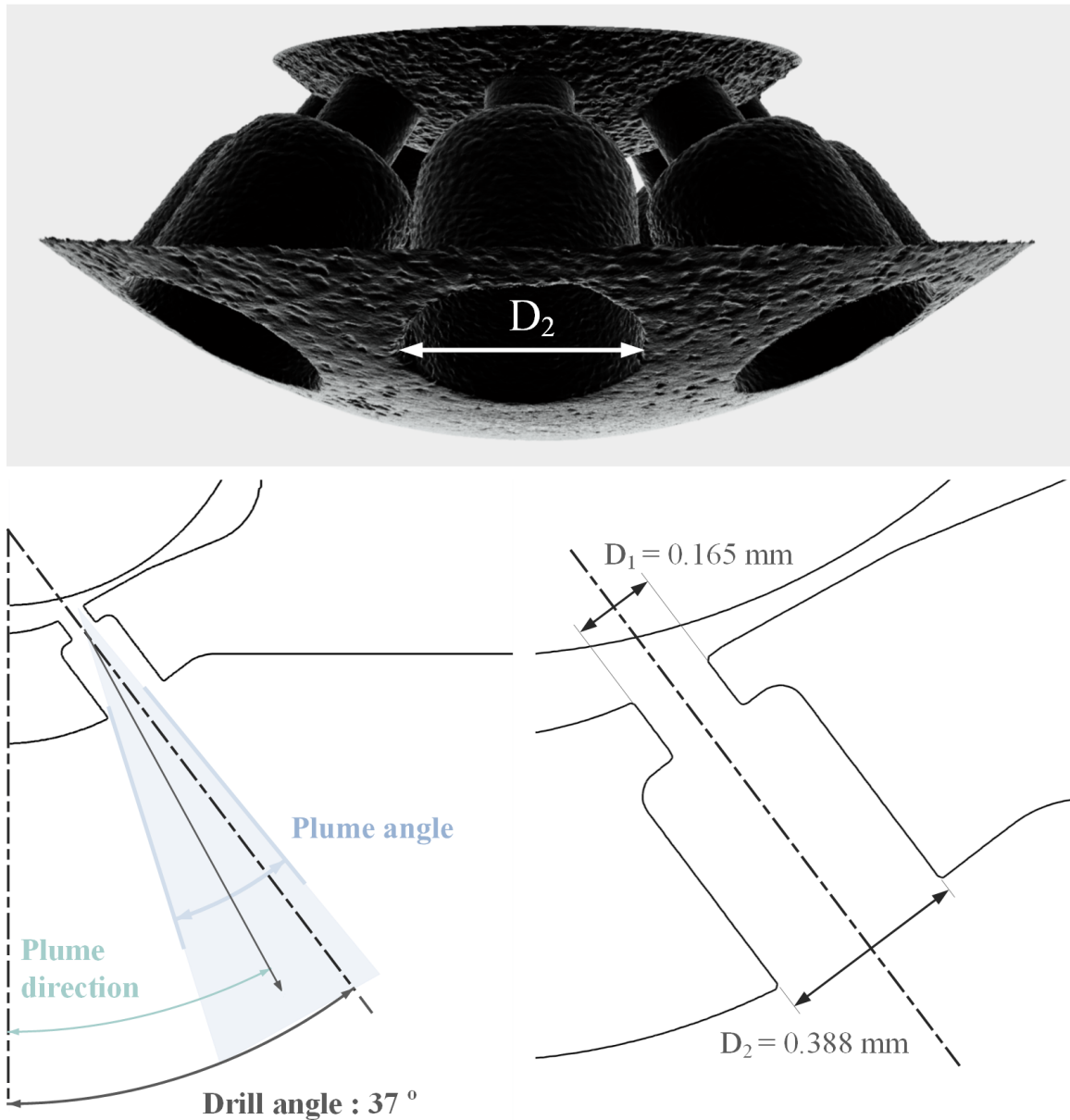


**Figure 6.1:** Characteristics of the Spray-G 8-hole counterbore injector.

The mesh represents one-fourth of the seat geometry and a semi-spherical volume of the immediate downstream area where the fuel plumes develop. The mesh consists of approximately 1.8 million polyhedral cells resulting in a spatial resolution of  $8 \mu m$  at the nozzle area and in the counterbore area. The minimum cell size at the needle tip, at the location of minimum needle lift, is  $2 \mu m$ . Downstream the nozzle exit, the cell size gradually increases, reaching a maximum cell size of approximately  $360 \mu m$  near the numerical domain exit.

**Table 6.1:** Nominal dimensions and manufacturing characteristics of ECN, Spray G injector [10].

<b>Parameter</b>	<b>Value</b>
Number of holes	8
Spray Shape	Circular
Bend Angle	0°
Length-to-Diameter ratio (L/D)	1.4
Hole shape	Straight
Nominal flow rate	15 cc s <sup>-1</sup> at 10 MPa
Nozzle type	Valve covered orifice (VCO)
Nozzle shape	Step hole
Orifice diameter	0.165 mm
Orifice length	0.16 - 0.18 mm
Step diameter	0.388 mm
Orifice drill angle	37°
Full spray angle	80°

**Table 6.2:** Boundary conditions of ECN, Spray G injector for non-flashing (Spray-G) and flashing (Spray-G2) operation [10].

<b>Parameter</b>	<b>Spray-G</b>	<b>Spray-G2</b>
Fuel type	Iso-octane	Iso-octane
Inlet fuel temperature	363 K	363 K
Inlet fuel pressure	20 MPa	20 MPa
Ambient gas temperature	573 K	333 K
Ambient pressure	600 kPa	50 kPa
Ambient density	3.5 kg m <sup>-3</sup>	0.5 kg m <sup>-3</sup>
Initial ambient gas velocity	Less than 1 m/s	Less than 1 m/s

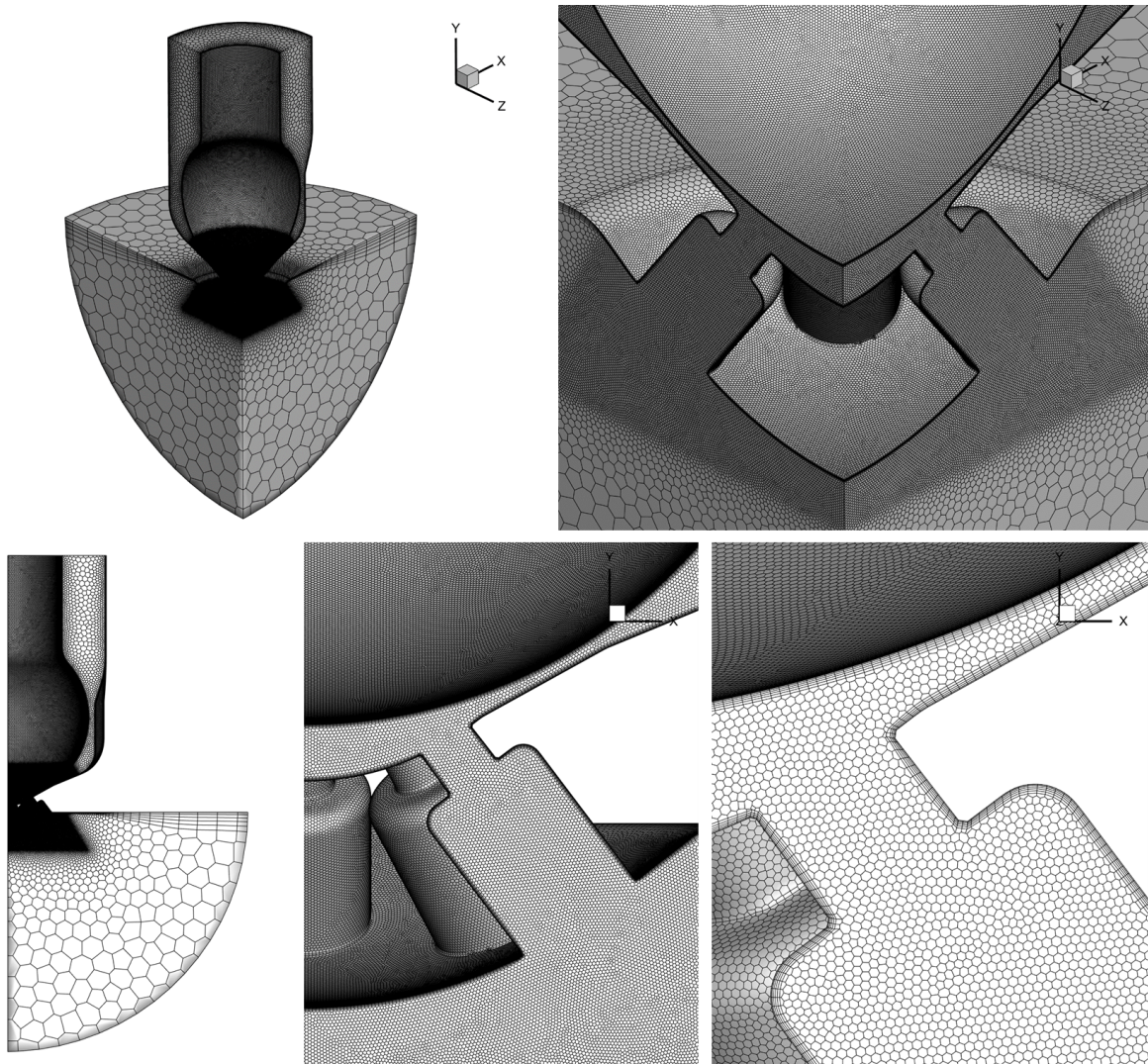


**Figure 6.2:** Overview of the numerical domain used for the spray G investigation including enlarged details of the numerical mesh at the location of the injector hole and counterbore.

The Taylor length scale,  $\lambda$ , for single-phase flow can be estimated from the correlation  $\lambda/D \approx \sqrt{10} Re^{-1/2}$ , yielding an estimate at the exit of the nozzle of  $\lambda \approx 2.4\mu m$ . This value implies a mesh-to-Taylor lengths scale ratio of around 4, which in turn suggests that the mesh resolution at the needle tip and within the nozzle holes can be considered adequate for an LES of the near-nozzle area. For the purpose of the LES initialisation, the nozzle and the orifices are filled with liquid iso-octane at the injection temperature of 363 K and a constant pressure equal to the injection pressure of 200 bar. The pressure in the discharge chamber is set at 50 kPa. A URANS simulation was initiated with the abovementioned conditions and a solution of the flow field was

obtained. The URANS solution was subsequently used as the starting point for the LES calculations. This approach was followed in order to decrease the computational cost of the numerical investigation by reducing the time needed for the LES treatment to reach a statistically stable mode.

### 6.3 Results

The numerical work presented in this section corresponds to case 14 of Table 3.3 and took place with the utilisation of a high-performance computing (HPC) service called Hyperion, provided by City, University of London. The Hyperion HPC unit is a collection of servers interconnected to a high-speed network. Hyperion has 72 CPU nodes and 4 GPU nodes. Each compute node has 2 Intel® Xeon® Gold 6248R processors. Each processor has 24 cores, 384 GB RAM and a local 1TB Solid State Disk (SSD) drive. The system has a regular file store that is backed up every day and backups are kept for 14 days. It has a fast parallel file system for storing temporary files which greatly enhances performance. The flashing iso-octane LES cases were executed on 2 of the 72 CPU nodes, where approximately one millisecond of flow time was calculated every 20 days. The complete set of boundary conditions of case 14 is presented in Table 6.2. The mass flow rate for the steady-lift phase of injection has been calculated based on the numerical results and is presented, both per-hole and in total, in Table 6.3. The results are compared with experimental data available for “Spray-G” conditions by Payri et al. [11] and the ECN [10], and describe the mass flow rate at maximum needle lift.

**Table 6.3:** Mass flow rate values for each injector hole during the maximum needle lift phase. Comparison of total mass flow rate with experimental values [11, 10].

Mass flow rate [kg s <sup>-1</sup> ]	Hole “1”	Hole “2”	Hole “3”	Total
Numerical ( $p_{amb} = 0.5 \text{ bar}$ )	0.00242	0.00211	0.00220	<b>0.01768</b>
Experimental ( $p_{amb} = 3 \text{ bar}$ )	-	-	-	<b>0.01446</b>

It should be noted that relevant experimental data for the “Spray-G2” boundary conditions that are pertinent to flashing are not available, a fact that highlights once more the need for relevant numerical approaches. The hole-to-hole flow rate variation of the numerical results is of the order of 15% while the rate of injection calculated numerically is comparable to the average experimental value reported for an ambient pressure of 3 bar. The numerical value is reported at an ambient pressure of 0.5 bar

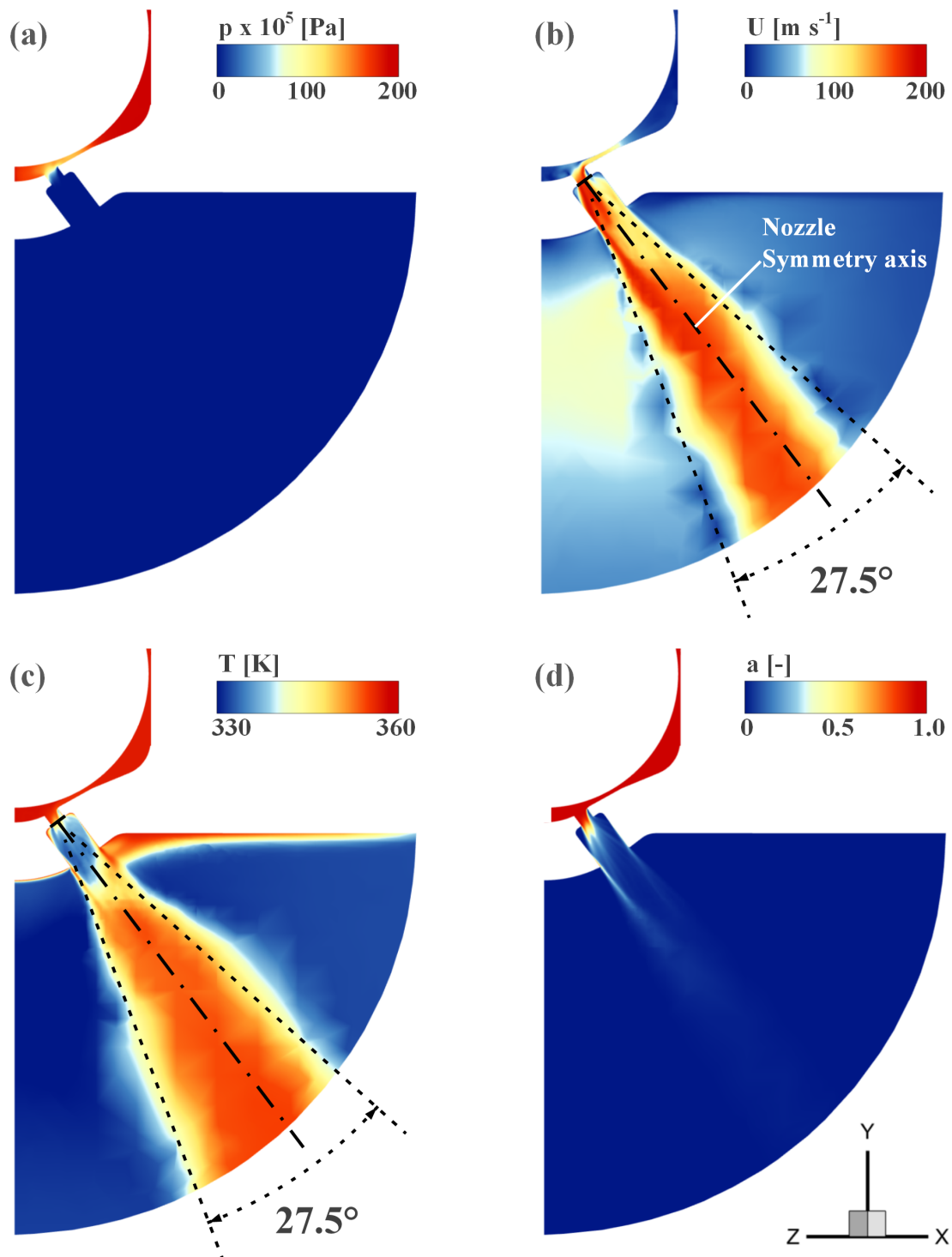


**Figure 6.3:** Contour plot over spray G hole plane of symmetry alongside the injection direction. Distribution of (a) pressure (b) velocity, (c) temperature and (d) liquid volume fraction.

and therefore the overprediction is justified. Due to the fact that symmetry boundary conditions were applied to the domain, the flow rate of the injector holes 1 and 3 has been adjusted to account for the complete hole opening.

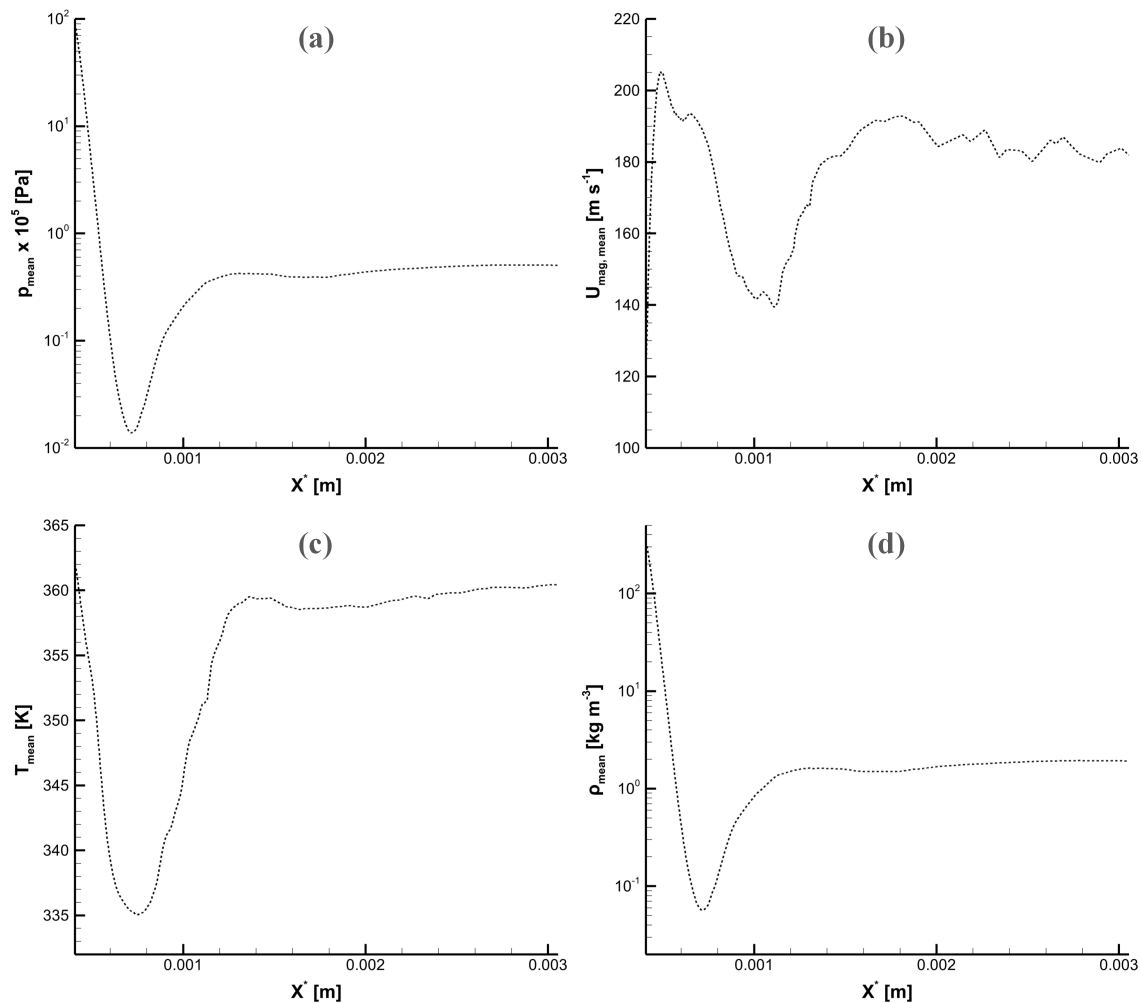


**Figure 6.4:** Line plots of variable evolution along the spray G hole central axis of symmetry. Distribution of (a) pressure logarithm (b) velocity, (c) temperature and (d) density.

To study the resulting spray, a contour plot over the plane of symmetry of injector hole “2” has been extracted and presented in [Figure 6.3](#). The fields of pressure, velocity, temperature and liquid volume fraction can be observed. All variables have been averaged over a time period of  $1 \mu\text{m}$ . The pressure field contour that is presented in [Figure 6.3.a](#) reveals the immediate pressure drop at the entrance of the nozzle hole, where a low-pressure area can be identified. The same low-pressure core extends up to the end of the counterbore, where it gradually adjusts to ambient pressure levels. The velocity profile, as presented in [Figure 6.3.b](#) shows the acceleration of the fuel,

starting at the location of the needle contraction, where the velocity reaches up to 140 m/s. When entering the nozzle, the area of high velocity coincides with a low-pressure location. At the beginning of the counterbore volume, the flash evaporation initiates and the two-phase mixture reaches velocity values of up to 200 m/s. Recirculation zones are forming at the perimeter of the inlet of the counterbore. The resulting plume angle was assessed as presented in [Figure 6.3.b](#) and [6.3.c](#) and is found to be  $27.5^\circ$ . The nozzle axis of symmetry is also indicated. Moreover, in [Figure 6.3.c](#), the temperature contour depicts the phase-change process that takes place within the counterbore volume, where the temperature drops as low as  $333\text{ }^\circ\text{C}$  due to the evaporation of iso-octane. The temperature recovery indicates that condensation appears downstream of the counterbore. Finally, the vapour volume fraction contour is presented in [Figure 6.3.d](#), where it becomes apparent that the flash-evaporation is dominant in the counterbore volume. On the walls of the counterbore, the results show a higher liquid volume fraction, indicating an interaction between the fuel and the wall that results in vapour condensation. The evolution of the field variables is additionally presented in a line plot manner, in [Figure 6.4](#), where density was chosen to be presented over liquid volume fraction. The reason for this was that the variations of density are more pronounced and provide better insight into the spray evolution. The distance axis marked as  $X^*[m]$  corresponds to the radial distance from the symmetry axis of the complete 8-hole spray G injector.

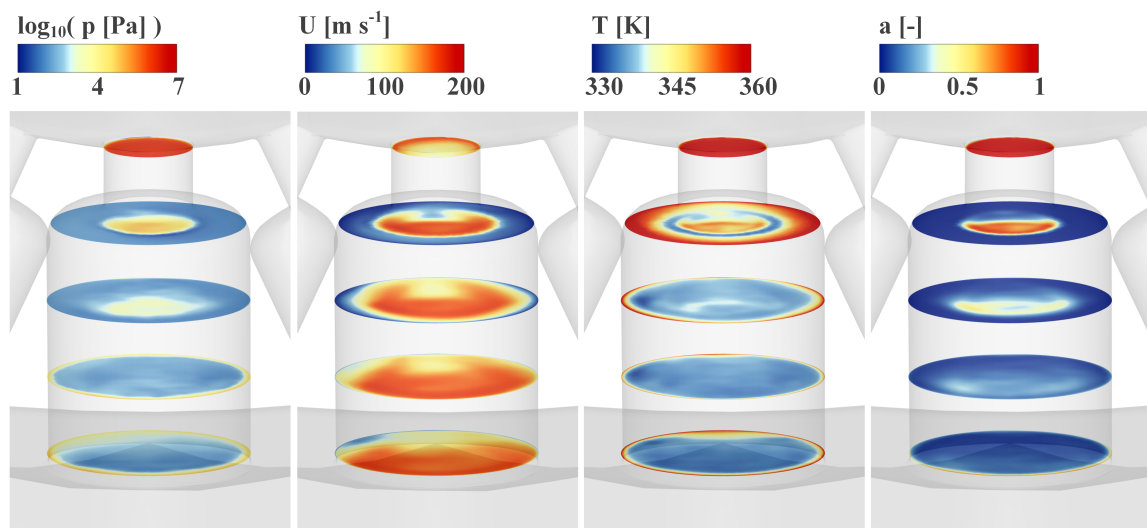


**Figure 6.5:** Contour plots on equidistant planes lying perpendicular to the spray G hole central axis of symmetry. Distribution of (a) pressure logarithm (b) velocity, (c) temperature and (d) liquid volume fraction.

In order to better examine the injector hole and counterbore volume, [Figure 6.5](#)

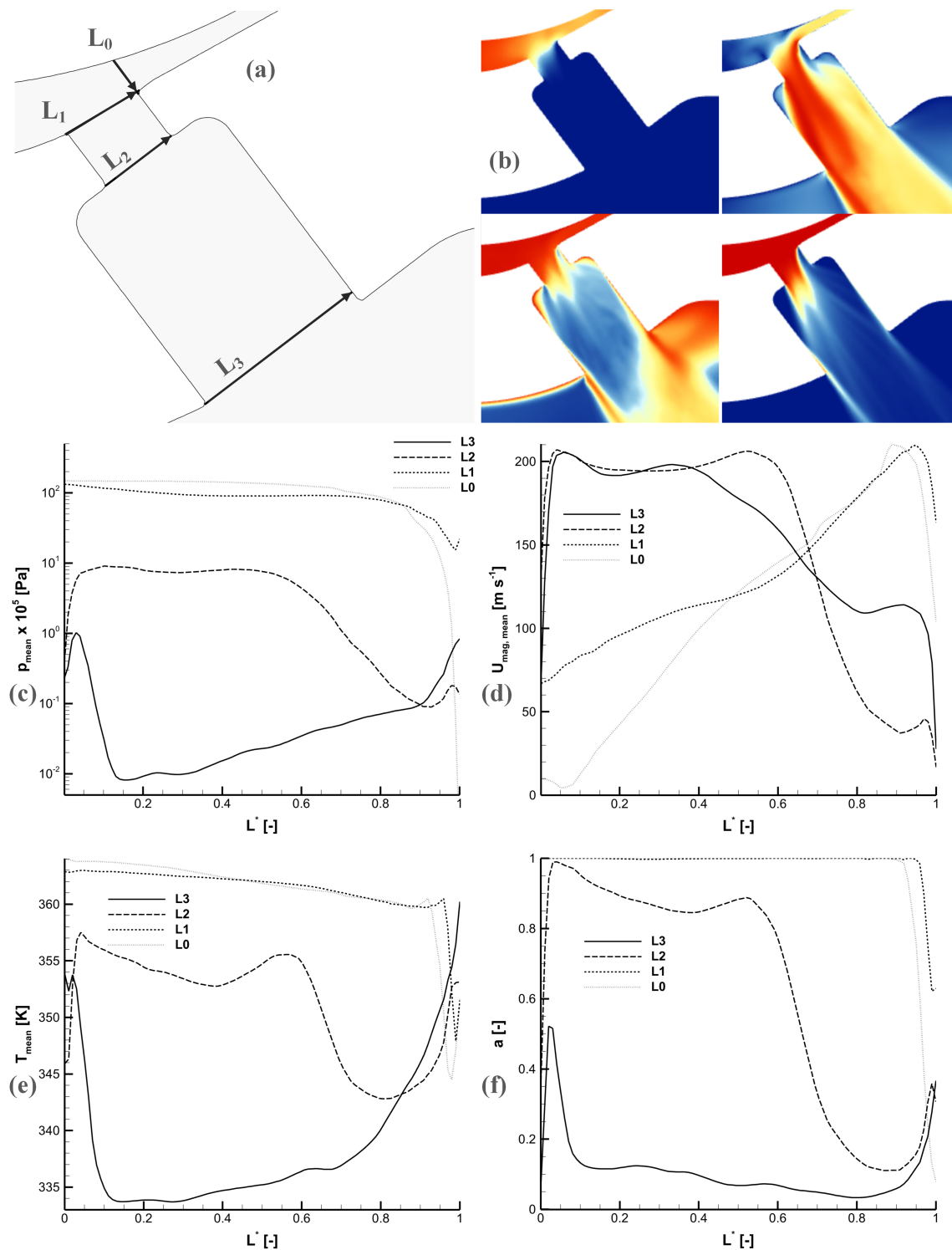


**Figure 6.6:** Definition of (a) vectors  $L_0$  to  $L_3$  and (b) contour of an enlarged view of the in-nozzle variable fields. Line plots of variable evolution along the vectors  $L_0$  to  $L_3$ . Distribution of (c) pressure (d) velocity, (e) temperature and (f) liquid volume fraction.

has been compiled. The variables of pressure logarithm, velocity, temperature and liquid volume fraction are presented on five planes positioned perpendicularly to the nozzle symmetry axis. By observing the pressure logarithm and liquid volume fraction contours, it can be deduced that a liquid core is present at the exit of the nozzle. In the velocity sub-figure, the recirculation area can be observed at the entrance of the counterbore section, while in the temperature sub-figure, the cool ring that is formed, marks the location where phase-change takes place and develops, downstream, into a vapour cone.

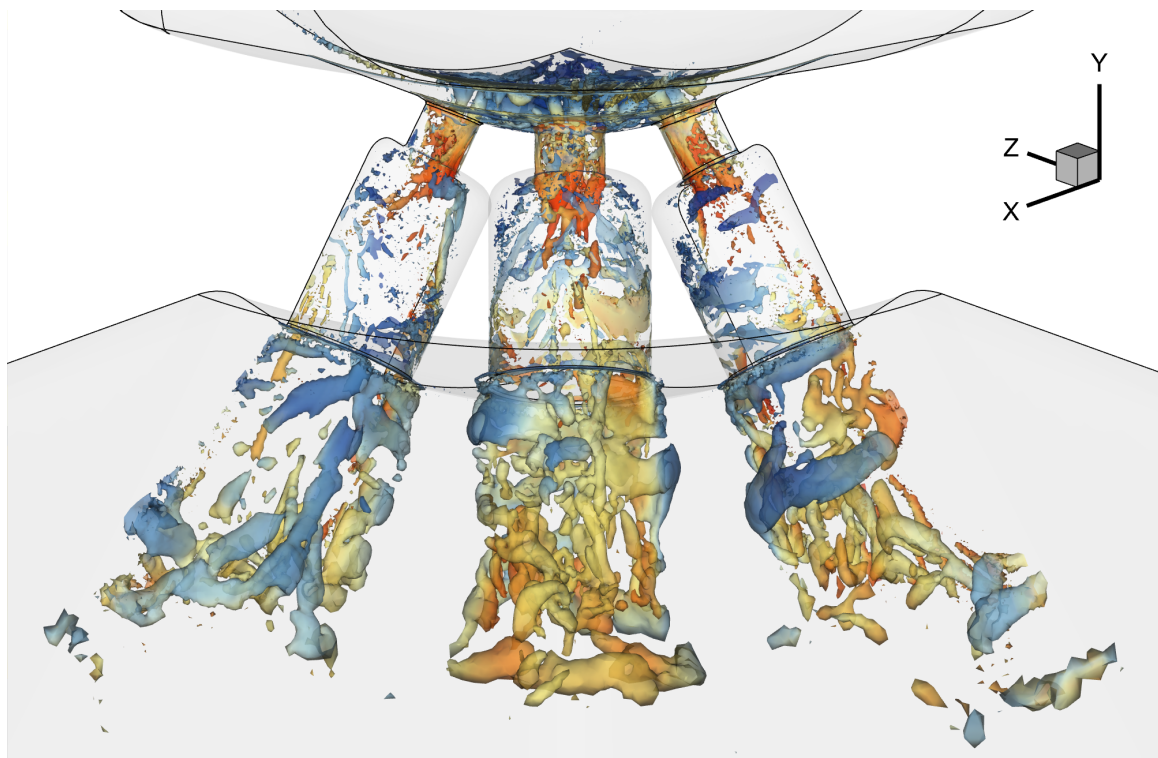


**Figure 6.7:** Turbulent structures at the in- and near-nozzle area presented by a Q-criterion iso-surface of a magnitude of  $1^{12}$ . Surface coloured by the magnitude of velocity.

The in-nozzle topology is presented more closely in [Figure 6.6](#). Four lines have been selected over the single-hole plane of symmetry and the evolution of field variables over said lines is presented.  $L_0$  corresponds to the smallest distance between the needle and the nozzle entrance, with an angle equivalent to the drill angle,  $L_1$  follows the diameter of the hole at the nozzle's entrance,  $L_2$  coincides with the diameter of the hole at the beginning of the counterbore and  $L_3$  corresponds to the counterbore diameter at its exit. The Y axis of the diagrams represents a dimensionless distance, where 0 and 1 correspond to the beginning and the end of each line respectively, according to the vectors drawn in [Figure 6.6.a](#). The evolution of the variables further into the spray-G

nozzle reveals the location of the flashing inception. Low-pressure values near the nozzle wall ( $L^* = 1$ ) mark the initialisation of the phase-change process that, due to the asymmetry of the flow with respect to the nozzle axis, propagates and creates a low-pressure region towards the opposite wall ( $L^* = 0$ ). The temperature differences over the examined lines appear to follow the trend of the corresponding pressure lines. Finally, Liquid volume fraction curves clearly depict the phase change that begins at the edge where the  $L_0$  and  $L_1$  vectors end.

Turbulent structures at the in-nozzle and near nozzle area are presented in [Figure 6.7](#). A transparent iso-surface of Q-criterion magnitude of  $1^{12}$  is presented in the Figure and coloured by the flow velocity magnitude passing through the vortex core regions. Turbulent structures are mostly found within the nozzle at locations of high velocity. After the nozzle inlet, within the counterbore volume, the structures are limited while downstream the counterbore exit a higher concentration is observed.

### 6.4 Concluding remarks

In the work presented in this chapter, a two-phase flow of iso-octane was simulated using a Large Eddy Simulation framework. The operating conditions correspond to the “Spragy-G2” boundary conditions provided by the Engine Combustion Network (ECN). A third phase was introduced to account for the ambient nitrogen acting as a non-dissolved gas. For this numerical investigation, a pressure-based solver was used, utilising a bubble-dynamics model employing the Hertz-Knudsen equation. The specific model takes into account the thermodynamic non-equilibrium between the two phases with the introduction of an accommodation coefficient. The liquid phase was thermodynamically represented with the introduction of a real-gas table of properties whereas the vapour was treated as an ideal gas. The resulting rate of injection is comparable to the rate corresponding to the “Spray-G” conditions. Further testing and, ideally, more experimental data are deemed needed to conclusively confirm possible advantages of the utilised phase-change model, however, the applied numerical approach appears to be able to represent the in- and near-nozzle flashing process of the ECN “Spray-G2” configuration.

# CHAPTER 7

## Conclusions

Flash boiling in aerospace and automotive applications has been the focus of this work. However, the methods proposed in this thesis can be applied to a broad spectrum of engineering problems, ranging from gasoline direct injection (GDI) and aerospace engine optimisation to industrial cooling and nuclear safety. To study the phenomenon two different numerical solvers are implemented. The first solver is a compressible, transient, explicit, density-based solver, on which tabulated thermodynamic properties have been implemented. The thermodynamic data was derived from solving a high-order equation of state based on Helmholtz free energy. The solver structure implies the assumption of thermal equilibrium regarding the phase change. The density-based solver operates within the OpenFOAM framework and has been executed for URANS simulations. The second solver is a compressible, transient, implicit, coupled, pressure-based solver that was used within the framework of ANSYS Fluent software. A two-phase mixture approach that assumes mechanical equilibrium was implemented. A mass transfer model based on bubble-dynamics considerations, representing a thermal non-equilibrium approach, has been developed and tested not only on URANS but DES and LES formulations as well.

Quantitative and qualitative comparisons between the two approaches have taken place. A wide range of experimental conditions has been investigated. The condition ranged from non-flashing, to fully flashing with high superheat ratios of up to 245. The majority of cases took place in the subcritical regime but supercritical pressure conditions were also examined. Both the selected boundary condition sets and the selected operating fluids are of relevance to space applications. More specifically, in the first part of this numerical work, two-phase oxygen flow was numerically investigated in a converging-diverging nozzle in both sub- and supercritical pressure conditions. In the second part of the present work two-phase flashing flows of liquid oxygen and liquid nitrogen injected into near-vacuum conditions were simulated. Finally, iso-octane injection under flashing conditions was studied using Large Eddy Simulation.

The variable level of accuracy among the numerical results highlights the fact that

flash boiling, in the context of jets and sprays, is a process of high uncertainty due to its inherent features, namely metastability effects and transient phenomena that may take place upon its development. Although the thermal equilibrium assumption might not always be justified, in the case of cryogenic fluid injection under steady conditions, the method is sufficiently accurate. Under such conditions, unlike models based on a vapour-transport equation, the presented methodology can be applied without any calibration for any range of conditions that have been tabulated, regardless of the boundary conditions or the involved geometry.

Recommendations for future work fall under three categories. Firstly, the expansion of the investigation to a wider range of flashing applications, secondly the decrease of the computational cost of the developed solver and finally, the expansion of the thermodynamic properties from a single-fluid approach to fluid mixtures. As the results of this research work suggest, the developed framework is applicable for flashing flows under steady conditions, therefore, the investigation of transient phenomena in flashing processes is recommended as a next step. Regarding the computational cost, the use of low time-step value is unavoidable during the explicit numerical resolution due to the extremely fast evolution of the flash boiling phenomenon and the high vapour velocities that develop. Thus, the computational time needed to produce the results of this research was demanding even for a URANS framework. The development of an implicit implementation of the presented methodology, with the ability to use larger time-step values can significantly reduce the computational cost. Finally, on the matter of fluid properties, implementation of the tabulation process to fluid mixtures and assessment of the accuracy of the results is an important step for broadening the applicability of the methodology.

## Developed solvers and functions, and implementation process

Open-FOAM solver, “tabFoam”

```
1 #include "fvCFD.H"
2 #include "dynamicFvMesh.H"
3 #include "kinematicMomentumTransportModel.H"
4 #include "fixedRhoFvPatchScalarField.H"
5 #include "incompressibleTwoPhaseMixture.H"
6 #include "directionInterpolate.H"
7 #include "localEulerDdtScheme.H"
8 #include "fvcSmooth.H"
9 #include "tableInfo.H" //thermo class definition
10 #include "functions.H" //functions implementation
11
12 int main(int argc, char *argv[])
13 {
14     #include "postProcess.H"
15     #include "setRootCaseLists.H"
16     #include "createTime.H"
17     #include "createDynamicFvMesh.H"
18     #include "initContinuityErrs.H"
19     #include "createFields.H"
20     #include "createTimeControls.H"
21
22     turbulence->validate();
23
24     #include <fstream>
25     #include <iostream>
```

```
26     #include <string>
27     #include <stdio.h>
28     #include <stdlib.h>
29
30     dimensionedScalar v_zero("v_zero", dimVolume/dimTime,
31                               0.0);
32     dimensionedScalar v_zero2("v_zero2", dimMass/dimTime,
33                                 0.0);
34     dimensionedScalar uBounded("uBounded", dimLength/
35                                   dimTime, 200.0);
36
37     ofstream resFile("residual.txt");
38
39     word nameOfTable(" ");
40     runTime.controlDict().readIfPresent("nameOfTable",
41                                         nameOfTable); //read file from controlDict
42     tableInfo unif(nameOfTable); //call constructor
43
44     #include "calculateThermo.H"
45
46     // Courant numbers used to adjust the time-step
47     scalar CoNum = 0.0;
48     scalar meanCoNum = 0.0;
49
50     Info<< "\nStarting time loop\n" << endl;
51
52     while (runTime.run())
53     {
54         volScalarField rhoOld("rhoOld",rho);
55         volVectorField rhoUOld("rhoUOld",rhoU);
56         volScalarField rhoEOld("rhoEOld",rhoE);
57
58         #include "createFlux.H" // --- Directed
59             interpolation of primitive fields onto faces
60
61     for( int cycle = 0; cycle < RK4values.size(); cycle++)
62         { //RK stages
```

```
57
58     Info << "starting cycle " << cycle << endl;
59
60     volScalarField& rhokcycle = rhok[cycle]();
61     volVectorField& rhoUkcycle = rhoUk[cycle]();
62     volScalarField& rhoEkcycle = rhoEk[cycle]();
63
64     if(cycle==0){// save the old time modify rho,rhoU
65
66         rhokcycle = fvc::div(rhoPhi);
67         rhoUkcycle = fvc::div(phiUp) - fvc::laplacian(
            muEff, U) - fvc::div(tauMC);
68
69         rhoEkcycle =
70         (
71             fvc::div(phiEUp)
72             - fvc::div(sigmaDotU)
73             - fvc::laplacian(k_eff,T)
74         );
75
76     }//if
77
78     else{
79
80         rho = rhoOld;
81         rhoU = rhoUOld;
82         rhoE = rhoEOld;
83
84         volScalarField& rhokcycle0 = rhok[cycle - 1]();
85         volVectorField& rhoUkcycle0 = rhoUk[cycle - 1]();
86         volScalarField& rhoEkcycle0 = rhoEk[cycle - 1]();
87
88         // --- Solve density
89         solve(fvm::ddt(rho) + rhokcycle0 * RK4values[
            cycle]);
90         rho.correctBoundaryConditions();
91
```

```
92     // --- Solve momentum
93     solve(fvm::ddt(rhoU) + rhoUkcycle0 * RK4values[
          cycle]);
94
95     //U.ref() = rhoU.ref() /rho.ref();
96     U.ref() = rhoU() /rho();
97     U.correctBoundaryConditions();
98     rhoU.boundaryFieldRef() == rho.boundaryField()*U.
          boundaryField();
99
100    // --- Solve energy
101    solve(fvm::ddt(rhoE) + rhoEkcycle0 * RK4values[
          cycle]);
102    e = rhoE/rho - 0.5*magSqr(U);
103    e.correctBoundaryConditions();
104    rhoE.boundaryFieldRef() == rho.boundaryFieldRef()
          *( e.boundaryFieldRef() + 0.5*magSqr(U.
          boundaryFieldRef()) );
105
106    #include "flux.H"
107
108    rhokcycle = fvc::div(rhoPhi);
109    rhoUkcycle = fvc::div(phiUp) - fvc::laplacian(
          muEff, U) - fvc::div(tauMC);
110
111    rhoEkcycle =
112    (
113        fvc::div(phiEUp)
114        - fvc::div(sigmaDotU)
115        - fvc::laplacian(k_eff, T)
116    );
117
118    #include "calculateThermo.H"
119
120 }//else
121
122     runTime.write();
```

```
123
124     }//forLoop
125
126     rho = rhoOld;
127     rhoU = rhoUOld;
128     rhoE = rhoEOld;
129
130     volScalarField rhokRK = rhok[0]();
131     volVectorField rhoUkRK = rhoUk[0]();
132     volScalarField rhoEkRK = rhoEk[0]();
133
134     Info << RK4values2 << endl;
135
136     rhokRK *= RK4values2[0];
137     rhoUkRK *= RK4values2[0];
138     rhoEkRK *= RK4values2[0];
139
140     for( int i = 1; i < RK4values.size(); i++){
141         volScalarField rhoki = rhok[i]();
142         volVectorField rhoUki = rhoUk[i]();
143         volScalarField rhoEki = rhoEk[i]();
144
145         rhokRK += RK4values2[i]*rhoki;
146         rhoUkRK += RK4values2[i]*rhoUki;
147         rhoEkRK += RK4values2[i]*rhoEki;
148     }
149
150     Info << "Runge Kutta 4 " << endl;
151
152     // --- Solve density
153     solve(fvm::ddt(rho) == -rhokRK);
154     rho.correctBoundaryConditions();
155
156     // --- Solve momentum
157     solve(fvm::ddt(rhoU) == -(rhoUkRK));
158
159     U.ref() = rhoU() / rho();
```

```
160     U.correctBoundaryConditions();
161     rhoU.boundaryFieldRef() == rho.boundaryField()*U.
        boundaryField();
162
163     // --- Solve energy
164     solve(fvm::ddt(rhoE) == -(rhoEkRK));
165     e = rhoE/rho - 0.5*magSqr(U);
166     e.correctBoundaryConditions();
167     rhoE.boundaryFieldRef() == rho.boundaryField()*( e
        .boundaryField() + 0.5*magSqr(U.
        boundaryFieldRef()) );
168
169     #include "calculateThermo.H"
170
171     turbulence->correct();
172
173     runTime.write();
174
175     #include "residuals.H"
176
177     Info<< "ExecutionTime = " << runTime.
        elapsedCpuTime() << " s"
178         << "   ClockTime = " << runTime.
        elapsedClockTime() << " s"
179         << nl << endl;
180
181     } //while runTime
182
183     Info<< "End\n" << endl;
184
185     return 0;
186 }
```

## ANSYS-Fluent mass-transfer model, “Hertz-Knudsen”

```

1 #include "udf.h"
2
3 DEFINE_MASS_TRANSFER(liq_gas_source, cell, thread,
4     from_index, from_species_index, to_index,
5     to_species_index)
6 {
7     real m_dot, dp;
8     real Rg = 8314/28.0134;
9     real lamda = 0.7; /* accommodation coefficient */
10    real surf = 4.0 * 3.14159 * pow(10.0, -12.0);
11    real c_evap = 1.0;
12    real c_cond = -1.0;
13    Thread *liq = THREAD_SUB_THREAD(thread, from_index);
14    Thread *vap = THREAD_SUB_THREAD(thread, to_index);
15    real p_op = RP_Get_Real("operating-pressure");
16    real press = C_P(cell, thread) + p_op;
17    real rho_l = C_R(cell, liq);
18    real rho_v = C_R(cell, vap);
19    real vof_l = C_VOF(cell, liq);
20    real vof_v = C_VOF(cell, vap);
21    real T_l = C_T(cell, liq);
22    real cst = pow(6.283185307 * Rg, 0.5);
23    real P_SAT = pow(10, (3.7362 - 264.651 / (T_l - 6.788)
24        )) * 100000;
25    real n0 = pow(10.0, 13.0);
26
27    m_dot = 0.0;
28    if (press <= P_SAT)
29    {
30        dp = P_SAT - press;
31        dp = MAX(dp, 1.0e-5);
32        m_dot = c_evap * n0 * surf * lamda / cst * dp /
33            sqrt(T_l) * vof_l;
34    }
35    else

```

```
32     {  
33         dp = press - P_SAT;  
34         dp = MAX(dp, 1e-5);  
35         m_dot = 0.0;  
36     }  
37     return (m_dot);  
38 }
```

Implementation process flow diagram of “tabFoam”

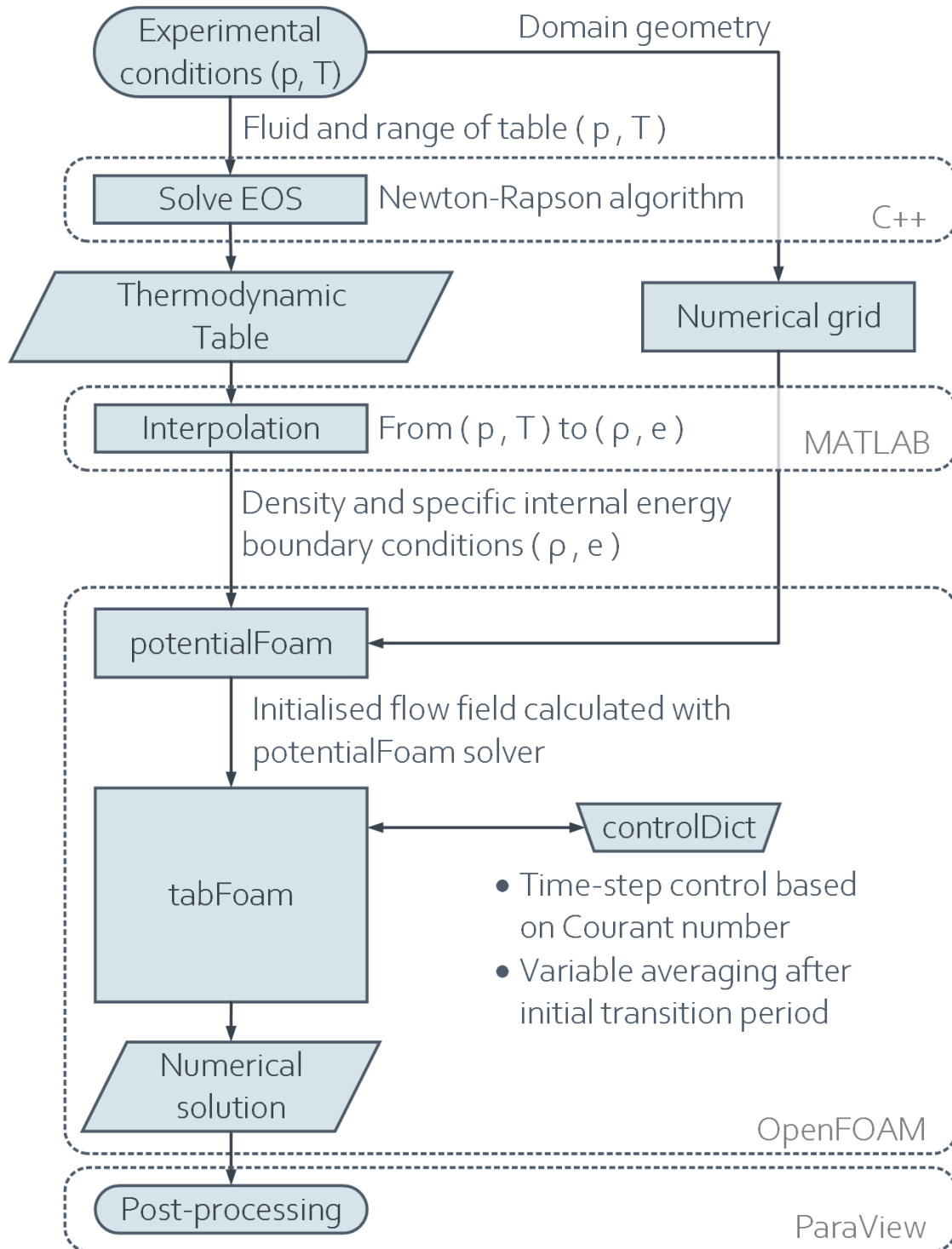


**Figure A.1:** Flow diagram of the implementation process of the compressible, two-phase solver “tabFoam”, for the purpose of examining the performance of HEM in the context of cryogenic flash boiling.



# List of Publications

## Peer-Reviewed Journal Publications

**T. Lyras**, I. Karathanassis, N. Kyriazis, P. Koukouvinis, and M. Gavaises, “Modelling of liquid oxygen and nitrogen injection under flashing conditions,” *Applied Thermal Engineering*, vol. 237, p. 121773, 2024. [doi:10.1016/j.applthermaleng.2023.121773](https://doi.org/10.1016/j.applthermaleng.2023.121773)

**T. Lyras**, I. Karathanassis, N. Kyriazis, P. Koukouvinis, and M. Gavaises, “Modelling of liquid oxygen nozzle flows under subcritical and supercritical pressure conditions,” *International Journal of Heat and Mass Transfer*, vol. 177, p. 121559, 2021. [doi:10.1016/j.ijheatmasstransfer.2021.121559](https://doi.org/10.1016/j.ijheatmasstransfer.2021.121559)

## Conference Publications

**T. Lyras**, I. K. Karathanassis, N. Kyriazis, P. Koukouvinis, and M. Gavaises, “Numerical modelling of cryogenic flows under near-vacuum pressure conditions,” *Proceedings of the 4th International Seminar on Non-Ideal Compressible Fluid Dynamics for Propulsion and Power*, pp. 114–124, Springer, 2022. [doi:10.1007/978-3-031-30936-6\\_12](https://doi.org/10.1007/978-3-031-30936-6_12)

**T. Lyras**, I. K. Karathanassis, P. Koukouvinis, and M. Gavaises, “Modelling of Liquid Oxygen Two-Phase Flow Expansion at Sub-and Supercritical Pressure Conditions,” *ILASS–Europe 2019, 29th Conference on Liquid Atomization and Spray Systems*, Paris, France, 2-4 September 2019.

## Workshop Participation

**T. Lyras**, I. K. Karathanassis, P. Koukouvinis, and M. Gavaises, “Numerical Modelling of Liquid Oxygen Two-Phase Flow Expansion At Sub- And Supercritical Pressure Conditions,” *6th Cavitation Workshop*, International Institute for Cavitation Research, CIHEAM, Greece, 2019. (poster and presentation participation)

## Bibliography

- [1] O. Miyatake, I. Tanaka, and N. Lior, “A simple universal equation for bubble growth in pure liquids and binary solutions with a nonvolatile solute,” *International journal of heat and mass transfer*, vol. 40, no. 7, pp. 1577–1584, 1997.
- [2] H. Witlox, M. Harper, P. Bowen, and V. Cleary, “Flashing liquid jets and two-phase droplet dispersion: Ii. comparison and validation of droplet size and rainout formulations,” *Journal of hazardous materials*, vol. 142, no. 3, pp. 797–809, 2007.
- [3] T. Bar-Kohany and M. Levy, “STATE OF THE ART REVIEW OF FLASH-BOILING ATOMIZATION,” *Atomization and Sprays*, vol. 26, no. 12, pp. 1259–1305, 2016.
- [4] I. Karathanassis, P. Koukouvinis, and M. Gavaises, “Comparative evaluation of phase-change mechanisms for the prediction of flashing flows,” *International Journal of Multiphase Flow*, vol. 95, pp. 257–270, 2017.
- [5] R. C. Hendricks, R. J. Simoneau, and R. F. Barrows, “Two-phase choked flow of subcooled oxygen and nitrogen,” *STIN 18376*, 1976.
- [6] W. Mayer, J. Telaar, R. Branam, G. Schneider, and J. Hussong, “Raman Measurements of Cryogenic Injection at Supercritical Pressure,” *Heat and Mass Transfer*, vol. 39, no. 8-9, pp. 709–719, 2003.
- [7] G. Lamanna, H. Kamoun, B. Weigand, C. Manfretti, A. Rees, J. Sender, M. Oschwald, and J. Steelant, “Flashing Behavior of Rocket Engine Propellants,” *Atomization and Sprays*, vol. 25, no. 10, pp. 837–856, 2015.
- [8] A. REES, H. SALZMANN, J. SENDER, and M. OSCHWALD, “Investigation of Flashing LN<sub>2</sub>-Jets in Terms of Spray Morphology, Droplet Size and Velocity Distributions,” p. 13 pages, 2019. Artwork Size: 13 pages Medium: PDF Publisher: Proceedings of the 8th European Conference for Aeronautics and Space Sciences. Madrid, Spain, 1-4 july 2019.
- [9] "National Institute of Standards and Technology (NIST)" official web-page. <https://www.nist.gov/> [Accessed: Dec. 2023].

- [10] "Engine Combustion Network (ECN)" official web-page. <https://ecn.sandia.gov/> [Accessed: Dec. 2023].
- [11] R. Payri, J. Gimeno, P. Marti-Aldaravi, and D. Vaquerizo, "Momentum flux measurements on an ecn gdi injector," tech. rep., SAE Technical Paper, 2015.
- [12] Z. Zhifu, W. Weitao, C. Bin, W. Guoxiang, and G. Liejin, "An experimental study on the spray and thermal characteristics of r134a two-phase flashing spray," *International Journal of Heat and Mass Transfer*, vol. 55, no. 15-16, pp. 4460–4468, 2012.
- [13] V. Cleary, P. Bowen, and H. Witlox, "Flashing liquid jets and two-phase droplet dispersion: I. experiments for derivation of droplet atomisation correlations," *Journal of Hazardous Materials*, vol. 142, no. 3, pp. 786–796, 2007.
- [14] J. C. Lin, "Insights from the risk analysis of a nearby propane tank farm," *Probabilistic Safety Assessment and Management PSAM*, vol. 12, 2014.
- [15] B. Avksentyuk and V. Ovchinnikov, "Dynamics of explosive boiling of drops at the superheat limit," *Journal of applied mechanics and technical physics*, vol. 40, no. 6, pp. 1070–1076, 1999.
- [16] T. Alghamdi, S. T. Thoroddsen, and J. F. Hernández-Sánchez, "Ultra-high speed visualization of a flash-boiling jet in a low-pressure environment," *International Journal of Multiphase Flow*, vol. 110, pp. 238–255, 2019.
- [17] J. Simões-Moreira and C. Bullard, "Pressure drop and flashing mechanisms in refrigerant expansion devices," *International Journal of Refrigeration*, vol. 26, no. 7, pp. 840–848, 2003.
- [18] Y. Liao and D. Lucas, "A review on numerical modelling of flashing flow with application to nuclear safety analysis," *Applied Thermal Engineering*, vol. 182, p. 116002, Jan. 2021.
- [19] E. Golliher, A. Licari, and T. Jin, "Testing of a compact flash evaporator system for exploration," tech. rep., SAE Technical Paper, 2008.
- [20] S. Zheng, X. Xie, and Y. Jiang, "Experimental study on the flash evaporation process of librh2o solution in an absorption heat pump," *International Journal of Refrigeration*, vol. 61, pp. 117–126, 2016.

- [21] C. Lv, Z. Zhang, Q. Zhao, T. Zhang, X. Guo, and J. Wang, “Numerical simulation of flash vaporisation in alumina production,” *Canadian Metallurgical Quarterly*, vol. 55, no. 4, pp. 463–469, 2016.
- [22] W. Zhao, J. Yan, S. Gao, T. H. Lee, and X. Li, “Effects of fuel properties and aerodynamic breakup on spray under flash boiling conditions,” *Applied Thermal Engineering*, vol. 200, p. 117646, 2022.
- [23] M. M. Khan, J. Hélie, M. Gorokhovski, and N. A. Sheikh, “Experimental and numerical study of flash boiling in gasoline direct injection sprays,” *Applied Thermal Engineering*, vol. 123, pp. 377–389, Aug. 2017.
- [24] A. Rees, H. Salzmann, J. Sender, and M. Oswald, “About the Morphology of Flash Boiling Liquid Nitrogen Sprays,” *Atomiz Spr*, vol. 30, no. 10, pp. 713–740, 2020.
- [25] A. Mansour and N. Müller, “A review of flash evaporation phenomena and resulting shock waves,” *Experimental Thermal and Fluid Science*, vol. 107, pp. 146–168, Oct. 2019.
- [26] N. Ashgriz, *Handbook of atomization and sprays: theory and applications*. Springer Science & Business Media, 2011.
- [27] S. M. Ghiaasiaan, *Two-phase flow, boiling, and condensation: in conventional and miniature systems*. Cambridge University Press, 2007.
- [28] B. Mikic, W. Rohsenow, and P. Griffith, “On bubble growth rates,” *International Journal of Heat and Mass Transfer*, vol. 13, no. 4, pp. 657–666, 1970.
- [29] M. Luo and O. J. Haidn, “Characterization of Flashing Phenomena with Cryogenic Fluid Under Vacuum Conditions,” *Journal of Propulsion and Power*, vol. 32, pp. 1253–1263, Sept. 2016.
- [30] G. Lamanna, H. Kamoun, B. Weigand, and J. Steelant, “Towards a unified treatment of fully flashing sprays,” *International Journal of Multiphase Flow*, vol. 58, pp. 168–184, 2014.
- [31] E. Sher, T. Bar-Kohany, and A. Rashkovan, “Flash-boiling atomization,” *Progress in Energy and Combustion Science*, vol. 34, no. 4, pp. 417–439, 2008.
- [32] L. Rayleigh, “Viii. on the pressure developed in a liquid during the collapse of a spherical cavity,” *The London, Edinburgh, and Dublin Philosophical Magazine and Journal of Science*, vol. 34, no. 200, pp. 94–98, 1917.

- [33] C. E. Brennen, *Cavitation and bubble dynamics*. New York: Cambridge University Press, 2014.
- [34] M. S. Plesset and A. Prosperetti, “Bubble dynamics and cavitation,” *Annual review of fluid mechanics*, vol. 9, no. 1, pp. 145–185, 1977.
- [35] M. S. Plesset and S. A. Zwick, “The growth of vapor bubbles in superheated liquids,” *Journal of applied physics*, vol. 25, no. 4, pp. 493–500, 1954.
- [36] H. Forster and N. Zuber, “Growth of a vapor bubble in a superheated liquid,” *Journal of Applied Physics*, vol. 25, no. 4, pp. 474–478, 1954.
- [37] G. Birkhoff, R. Margulies, and W. Horning, “Spherical bubble growth,” *The physics of fluids*, vol. 1, no. 3, pp. 201–204, 1958.
- [38] L. Scriven, “On the dynamics of phase growth,” *Chemical engineering science*, vol. 50, no. 24, pp. 3907–3917, 1995.
- [39] O. Miyatake and I. Tanaka, “Bubble growth in uniformly superheated water at reduced pressures, part 1: numerical analysis and derivation of a simplified expression,” *Transactions JSME, Series B*, vol. 48, pp. 355–363, 1982.
- [40] O. Miyatake and I. Tanaka, “Bubble growth in uniformly superheated water at reduced pressures, part 2: experimental results and comparison with numerical results and with the simplified expression,” *Transactions of the JSME, Series B*, vol. 48, pp. 364–372, 1982.
- [41] T. Theofanous and P. Patel, “Universal relations for bubble growth,” *International Journal of Heat and Mass Transfer*, vol. 19, no. 4, pp. 425–429, 1976.
- [42] H. Versteeg, G. Hargrave, and M. Kirby, “Internal flow and near-orifice spray visualisations of a model pharmaceutical pressurised metered dose inhaler,” in *Journal of Physics: Conference Series*, vol. 45, p. 207, IOP Publishing, 2006.
- [43] A. Lefebvre, “Atomization and sprays, vol. 1040,” 1988.
- [44] G. J. Smallwood and O. L. Gulder, “Views on the structure of transient diesel sprays,” *Atomization and sprays*, vol. 10, no. 3-5, 2000.
- [45] M. Elkotb, “Fuel atomization for spray modelling,” *Progress in Energy and Combustion Science*, vol. 8, no. 1, pp. 61–91, 1982.

- [46] G. Lamanna, “Cryogenic Flashing Jets: A Review (Invited Paper),” in *52nd AIAA/SAE/ASEE Joint Propulsion Conference*, (Salt Lake City, UT), American Institute of Aeronautics and Astronautics, July 2016.
- [47] W. Mayer and H. Tamura, “Propellant injection in a liquid oxygen/gaseous hydrogen rocket engine,” *Journal of Propulsion and Power*, vol. 12, no. 6, pp. 1137–1147, 1996.
- [48] W. O. H. Mayer, A. H. A. Schik, B. Vielle, C. Chauveau, I. Gokalp, D. G. Talley, and R. D. Woodward, “Atomization and Breakup of Cryogenic Propellants Under High-Pressure Subcritical and Supercritical Conditions,” *Journal of Propulsion and Power*, vol. 14, pp. 835–842, Sept. 1998.
- [49] M. Habiballah, M. Orain, F. Grisch, L. Vingert, and P. Gicquel, “Experimental Studies of High-Pressure Cryogenic Flames on the Mascotte Facility,” *Combustion Science and Technology*, vol. 178, no. 1-3, pp. 101–128, 2006.
- [50] L. Vingert, G. Ordonneau, N. Fdida, and P. Grenard, “A Rocket Engine under a Magnifying Glass,” *AerospaceLab Journal*, vol. Issue 11, p. 13 pages, 2016.
- [51] J. Leung, “A generalized correlation for one-component homogeneous equilibrium flashing choked flow,” *AIChE Journal*, vol. 32, no. 10, pp. 1743–1746, 1986.
- [52] H. K. Fauske, “Contribution to the theory of two-phase, one-component critical flow,” tech. rep., Argonne National Lab., Ill., 1962.
- [53] H. Isbin, J. Moy, and A. Da Cruz, “Two-phase, steam-water critical flow,” *AIChE Journal*, vol. 3, no. 3, pp. 361–365, 1957.
- [54] F. Zaloudek, “The low pressure critical discharge of steam-water mixtures from pipes,” tech. rep., General Electric Co. Hanford Atomic Products Operation, Richland, Wash., 1961.
- [55] D. W. Faletti and R. Moulton, “Two-phase critical flow of steam-water mixtures,” *AIChE Journal*, vol. 9, no. 2, pp. 247–253, 1963.
- [56] R. Hu, J. Zhao, S.-P. Kao, and M. S. Kazimi, “Thermal-hydraulic stability analysis of natural circulation bwr’s,” in *Proc. Int. Congress on Advances in Nuclear Power Plants (ICAPP 2007)*, pp. 13–18, 2007.
- [57] M. Podowski, “Modeling and analysis of two-phase flow instabilities,” *NURETH-10*, 2003.

- [58] H. Richter, "Separated two-phase flow model: application to critical two-phase flow," *International Journal of Multiphase Flow*, vol. 9, no. 5, pp. 511–530, 1983.
- [59] F. J. Moody, "Maximum flow rate of a single component, two-phase mixture," 1965.
- [60] R. E. Henry and H. K. Fauske, "The two-phase critical flow of one-component mixtures in nozzles, orifices, and short tubes," 1971.
- [61] S. Levy, "Prediction of two-phase critical flow rate," 1965.
- [62] A. Attou, M. Giot, and J.-M. Seynhaeve, "Modelling of steady-state two-phase bubbly flow through a sudden enlargement," *International journal of heat and mass transfer*, vol. 40, no. 14, pp. 3375–3385, 1997.
- [63] R. Hu and M. S. Kazimi, "Flashing-induced instability analysis and the start-up of natural circulation boiling water reactors," *Nuclear technology*, vol. 176, no. 1, pp. 57–71, 2011.
- [64] F. Inada, M. Furuya, and A. Yasuo, "Thermo-hydraulic instability of boiling natural circulation loop induced by flashing (analytical consideration)," *Nuclear Engineering and Design*, vol. 200, no. 1-2, pp. 187–199, 2000.
- [65] H. Simpson and R. Silver, "Theory of one-dimensional, two-phase homogeneous non-equilibrium flow," in *Proc. Inst. Mech. Eng. Symposium on Two-Phase Flow*, vol. 45, 1962.
- [66] A. Edward and T. O'Brien, "Studies of phenomena connected with the depressurization of water reactor," *J. Br. Nucl. Energy Soc*, vol. 9, pp. 125–135, 1970.
- [67] C. Lackme, "2.8 thermodynamics of critical two-phase discharge from long pipes of initially subcooled water," in *Advanced Course in Heat Transfer in Nuclear Reactor Safety*, Begel House Inc., 1980.
- [68] Z. Bilicki and J. Kestin, "Physical aspects of the relaxation model in two-phase flow," *Proceedings of the Royal Society of London. A. Mathematical and Physical Sciences*, vol. 428, no. 1875, pp. 379–397, 1990.
- [69] P. Downar-Zapolski, Z. Bilicki, L. Bolle, and J. Franco, "The non-equilibrium relaxation model for one-dimensional flashing liquid flow," *International Journal of Multiphase Flow*, vol. 22, no. 3, pp. 473–483, 1996.

- [70] M. Reocreux, *Contribution to the study of critical flow rates in two-phase water vapor flow*, vol. 3. US Nuclear Regulatory Commission, 1977.
- [71] S. Mohammadein, “The derivation of thermal relaxation time between two-phase bubbly flow,” *Heat and mass transfer*, vol. 42, pp. 364–369, 2006.
- [72] K. Saha, S. Som, and M. Battistoni, “Investigation of homogeneous relaxation model parameters and their implications for gasoline injectors,” *Atomization and Sprays*, vol. 27, no. 4, 2017.
- [73] C. Lackme, “Incompleteness of the flashing of a supersaturated liquid and sonic ejection of the produced phases,” *International Journal of Multiphase Flow*, vol. 5, no. 2, pp. 131–141, 1979.
- [74] M. De Lorenzo, P. Lafon, J.-M. Seynhaeve, and Y. Bartosiewicz, “Benchmark of delayed equilibrium model (dem) and classic two-phase critical flow models against experimental data,” *International Journal of Multiphase Flow*, vol. 92, pp. 112–130, 2017.
- [75] K. Ardron and R. Furness, “A study of the critical flow models used in reactor blowdown analysis,” *Nuclear Engineering and Design*, vol. 39, no. 2-3, pp. 257–266, 1976.
- [76] K. Wolfert, M. Burwell, and D. Enix, “Non-equilibrium mass transfer between liquid and vapour phases during depressurization processes,” in *Transient two-phase flow. Proceedings of the second CSNI specialists meeting, Paris, 12-14 June 1978*, 1981.
- [77] E. Ruckenstein, “On heat transfer between vapour bubbles in motion and the boiling liquid from which they are generated,” *Chemical Engineering Science*, vol. 10, no. 1-2, pp. 22–30, 1959.
- [78] P. Kroeger, “Application of a non-equilibrium drift flux model to two-phase blowdown experiments,” tech. rep., Brookhaven National Lab., Upton, NY (USA), 1976.
- [79] E. Elias, S. Levy, and P. Chambré, “A mechanistic non-equilibrium model for two-phase critical flow,” *International journal of multiphase flow*, vol. 10, no. 1, pp. 21–40, 1983.

- [80] P. Saha, N. Abuaf, and B. J. C. Wu, “A Nonequilibrium Vapor Generation Model for Flashing Flows,” *Journal of Heat Transfer*, vol. 106, no. 1, p. 198, 1984.
- [81] J. Riznic, M. Ishii, and N. Afgan, “Mechanistic model for void distribution in flashing flow,” tech. rep., Institut za Nuklearne Nauke Boris Kidric, 1987.
- [82] G. B. Wallis, “Critical two-phase flow,” *International Journal of Multiphase Flow*, vol. 6, no. 1-2, pp. 97–112, 1980.
- [83] J. Bouré, “Critical flow phenomenon with reference to two-phase flow and nuclear reactor systems,” in *Thermal and hydraulic aspects of nuclear reactor safety. Vol. I*, 1977.
- [84] W. Rivard and J. Travis, “A nonequilibrium vapor production model for critical flow,” *Nuclear Science and Engineering*, vol. 74, no. 1, pp. 40–48, 1980.
- [85] M. Wein, “Numerische simulation von kritischen und nahkritischen zweiphasenströmungen mit thermischen und fluiddynamischen nichtgleichgewichtseffekten,” 2001.
- [86] P. Wesseling, *Principles of computational fluid dynamics*, vol. 29. Springer Science & Business Media, 2009.
- [87] F. R. Menter, “Two-equation eddy-viscosity turbulence models for engineering applications,” *AIAA Journal*, vol. 32, no. 8, pp. 1598–1605, 1994.
- [88] J. W. Gärtner, A. Kronenburg, A. Rees, J. Sender, M. Oswald, and G. Lamanna, “Numerical and experimental analysis of flashing cryogenic nitrogen,” *International Journal of Multiphase Flow*, vol. 130, p. 103360, Sept. 2020.
- [89] S. V. Patankar and D. B. Spalding, “A calculation procedure for heat, mass and momentum transfer in three-dimensional parabolic flows,” in *Numerical prediction of flow, heat transfer, turbulence and combustion*, pp. 54–73, Elsevier, 1983.
- [90] H. Bijl and P. Wesseling, “A unified method for computing incompressible and compressible flows in boundary-fitted coordinates,” *Journal of Computational Physics*, vol. 141, no. 2, pp. 153–173, 1998.

- [91] G. W. Burgreen, *Studies of pressure-velocity coupling schemes for analysis of incompressible and compressible flows*. The University of Alabama in Huntsville, 1987.
- [92] R. I. Issa, A. Gosman, and A. Watkins, “The computation of compressible and incompressible recirculating flows by a non-iterative implicit scheme,” *Journal of Computational Physics*, vol. 62, no. 1, pp. 66–82, 1986.
- [93] F. Moukalled and M. Darwish, “A unified formulation of the segregated class of algorithms for fluid flow at all speeds,” *NUMERICAL HEAT TRANSFER PART B FUNDAMENTALS*, vol. 37, no. 1, pp. 103–139, 2000.
- [94] I. Demirdžić, Ž. Lilek, and M. Perić, “A collocated finite volume method for predicting flows at all speeds,” *International journal for numerical methods in fluids*, vol. 16, no. 12, pp. 1029–1050, 1993.
- [95] S. K. Godunov, “A difference scheme for numerical solution of discontinuous solution of hydrodynamic equations,” *Math. Sbornik*, vol. 47, pp. 271–306, 1959.
- [96] P. Lax and B. Wendroff, “Systems of conservation laws,” in *Selected Papers Volume I*, pp. 263–283, Springer, 2005.
- [97] C. Hung and R. MacCormack, “Numerical solutions of supersonic and hypersonic laminar compression corner flows,” *AIAA Journal*, vol. 14, no. 4, pp. 475–481, 1976.
- [98] R. W. MacCormack, “A numerical method for solving the equations of compressible viscous flow,” *AIAA journal*, vol. 20, no. 9, pp. 1275–1281, 1982.
- [99] Y.-H. Choi and C. L. Merkle, “The application of preconditioning in viscous flows,” *Journal of computational physics*, vol. 105, no. 2, pp. 207–223, 1993.
- [100] L. Mangani, W. Sanz, and M. Darwish, “Comparing the performance and accuracy of a pressure-based and a density-based coupled solver,” in *16th International Symposium on Transport Phenomena and Dynamics of Rotating Machinery*, 2016.
- [101] F. Moukalled and M. Darwish, “A high-resolution pressure-based algorithm for fluid flow at all speeds,” *Journal of Computational Physics*, vol. 168, no. 1, pp. 101–130, 2001.

- [102] C. Hirsch, “Numerical computation of internal and external flows,” *Computational methods for inviscid and viscous flows*, vol. 2, 1990.
- [103] F. Moukalled, L. Mangani, M. Darwish, F. Moukalled, L. Mangani, and M. Darwish, *The finite volume method*. Springer, 2016.
- [104] A. Miettinen and T. Siikonen, “Application of pressure-and density-based methods for different flow speeds,” *International Journal for Numerical Methods in Fluids*, vol. 79, no. 5, pp. 243–267, 2015.
- [105] N. Kyriazis, P. Koukouvinis, and M. Gavaises, “Numerical investigation of bubble dynamics using tabulated data,” *International Journal of Multiphase Flow*, vol. 93, pp. 158–177, 2017.
- [106] S. Schmidt, I. Sezal, G. Schnerr, and M. Talhamer, “Riemann Techniques for the Simulation of Compressible Liquid Flows with Phase-Transition at all Mach Numbers - Shock and Wave Dynamics in Cavitating 3-D Micro and Macro Systems,” in *46th AIAA Aerospace Sciences Meeting and Exhibit*, (Reno, Nevada), American Institute of Aeronautics and Astronautics, 2008.
- [107] M.-S. Liou, “A sequel to AUSM, Part II: AUSM+-up for all speeds,” *Journal of Computational Physics*, vol. 214, no. 1, pp. 137–170, 2006.
- [108] E. Toro, *Riemann Solvers and Numerical Methods for Fluid Dynamics: A Practical Introduction*. Springer Berlin Heidelberg, 2013.
- [109] U. Setzmann and W. Wagner, “A new equation of state and tables of thermodynamic properties for methane covering the range from the melting line to 625 k at pressures up to 1000 mpa,” *Journal of Physical and Chemical reference data*, vol. 20, no. 6, pp. 1061–1155, 1991.
- [110] E. W. Lemmon and R. Tillner-Roth, “A Helmholtz energy equation of state for calculating the thermodynamic properties of fluid mixtures,” *Fluid Phase Equilibria*, vol. 165, no. 1, pp. 1–21, 1999.
- [111] B. M. Devassy, D. Benković, Z. Petranovic, W. Edelbauer, and M. Vujanovic, “Numerical Simulation of Internal Flashing in a GDI Injector Nozzle,” in *29th Conference on Liquid Atomization and Spray Systems*, (Paris, France), 2019.
- [112] P. Yi, H. Zhang, and S. Yang, “Evaluation of a non-equilibrium multi-component evaporation model for blended diesel/alcohol droplets,” in *AIAA Scitech 2020 Forum*, p. 2049, 2020.

- [113] K. Harstad and J. Bellan, “Interactions of fluid oxygen drops in fluid hydrogen at rocket chamber pressures,” *International Journal of Heat and Mass Transfer*, vol. 41, no. 22, pp. 3551–3558, 1998.
- [114] V. Yang, “Liquid-Propellant Rocket Engine Injector Dynamics and Combustion Processes at Supercritical Conditions:,” tech. rep., Defense Technical Information Center, Fort Belvoir, VA, 2004.
- [115] D. Coulon, “Vulcain-2 Cryogenic Engine Passes First Test with New Nozzle Extension,” *ESA Bouletin*, vol. 102, pp. 123–124, 2000.
- [116] S. Shine, S. S. Kumar, and B. Suresh, “A new generalised model for liquid film cooling in rocket combustion chambers,” *International Journal of Heat and Mass Transfer*, vol. 55, no. 19-20, pp. 5065–5075, 2012.
- [117] H. Meng and V. Yang, “Vaporization of two liquid oxygen (LOX) droplets in tandem in convective hydrogen streams at supercritical pressures,” *International Journal of Heat and Mass Transfer*, vol. 68, pp. 500–508, 2014.
- [118] R. Ingebo, “Cryogenic spray vaporization in high-velocity helium, argon and nitrogen gasflows,” in *32nd Aerospace Sciences Meeting and Exhibit*, p. 687, 1994.
- [119] H. Guo, B. Wang, Y. Li, H. Xu, and Z. Wu, “Characterizing external flashing jet from single-hole GDI injector,” *International Journal of Heat and Mass Transfer*, vol. 121, pp. 924–932, 2018.
- [120] B. Chehroudi, D. Talley, and E. Coy, “Visual characteristics and initial growth rates of round cryogenic jets at subcritical and supercritical pressures,” *Physics of Fluids*, vol. 14, no. 2, pp. 850–861, 2002.
- [121] S. Yamamoto and T. Furusawa, “Thermophysical flow simulations of rapid expansion of supercritical solutions (RESS),” *The Journal of Supercritical Fluids*, vol. 97, pp. 192–201, 2015.
- [122] Z. Yuan, W. Yangle, C. Jingtian, X. Zhaoyang, and W. Junfeng, “Numerical Simulation of Supercritical Carbon Dioxide Critical Flow in the Nozzle Tube,” *Journal of Nuclear Engineering and Radiation Science*, vol. 4, no. 1, p. 011018, 2018.

- [123] Z. Zhou, Y. Lu, J. Tang, X. Zhang, and Q. Li, “Numerical simulation of supercritical carbon dioxide jet at well bottom,” *Applied Thermal Engineering*, vol. 121, pp. 210–217, 2017.
- [124] K. Chen, R.-N. Xu, and P.-X. Jiang, “Numerical investigation of jet impingement cooling of a low thermal conductivity plate by supercritical pressure carbon dioxide,” *International Journal of Heat and Mass Transfer*, vol. 124, pp. 1003–1010, 2018.
- [125] S. Raman and H. Kim, “Solutions of supercritical CO<sub>2</sub> flow through a convergent-divergent nozzle with real gas effects,” *International Journal of Heat and Mass Transfer*, vol. 116, pp. 127–135, 2018.
- [126] H. Müller, C. A. Niedermeier, J. Matheis, M. Pfitzner, and S. Hickel, “Large-eddy simulation of nitrogen injection at trans- and supercritical conditions,” *Physics of Fluids*, vol. 28, no. 1, p. 015102, 2016.
- [127] A. Poormahmood, M. Shahsavari, and M. Farshchi, “Numerical Study of Cryogenic Swirl Injection Under Supercritical Conditions,” *Journal of Propulsion and Power*, vol. 34, no. 2, pp. 428–437, 2018.
- [128] J. Kang, J. Heo, H.-G. Sung, and Y. Yoon, “Dynamic characteristics of a cryogenic nitrogen swirl injector under supercritical conditions,” *Aerospace Science and Technology*, vol. 67, pp. 398–411, 2017.
- [129] N. Zong and V. Yang, “Cryogenic fluid dynamics of pressure swirl injectors at supercritical conditions,” *Physics of Fluids*, vol. 20, no. 5, p. 056103, 2008.
- [130] X. Wang, H. Huo, Y. Wang, L. Zhang, and V. Yang, “A Three-Dimensional Analysis of Swirl Injector Flow Dynamics at Supercritical Conditions,” in *53rd AIAA Aerospace Sciences Meeting*, (Kissimmee, Florida), American Institute of Aeronautics and Astronautics, 2015.
- [131] X. Wang, H. Huo, Y. Wang, and V. Yang, “Comprehensive Study of Cryogenic Fluid Dynamics of Swirl Injectors at Supercritical Conditions,” *AIAA Journal*, vol. 55, no. 9, pp. 3109–3119, 2017.
- [132] J. Travis, D. Piccioni Koch, and W. Breitung, “A homogeneous non-equilibrium two-phase critical flow model,” *International Journal of Hydrogen Energy*, vol. 37, no. 22, pp. 17373–17379, 2012.

- [133] K. Lyras, S. Dembele, D. P. Schmidt, and J. X. Wen, “Numerical simulation of subcooled and superheated jets under thermodynamic non-equilibrium,” *International Journal of Multiphase Flow*, vol. 102, pp. 16–28, 2018.
- [134] R. Schmehl and J. Steelant, “Computational Analysis of the Oxidizer Preflow in an Upper-Stage Rocket Engine,” *Journal of Propulsion and Power*, vol. 25, no. 3, pp. 771–782, 2009.
- [135] T. Ramcke, A. Lampmann, and M. Pfitzner, “Simulations of Injection of Liquid Oxygen/Gaseous Methane Under Flashing Conditions,” *Journal of Propulsion and Power*, vol. 34, no. 2, pp. 395–407, 2018.
- [136] P. Gaillard, C. L. Touze, L. Matuszewski, and A. Murrone, “Numerical Simulation of Cryogenic Injection in Rocket Engine Combustion Chambers,” no. 11, p. 15, 2016.
- [137] B. Abramzon and W. Sirignano, “Droplet vaporization model for spray combustion calculations,” *International Journal of Heat and Mass Transfer*, vol. 32, no. 9, pp. 1605–1618, 1989.
- [138] P. Koukouvinis, A. Vidal-Roncero, C. Rodriguez, M. Gavaises, and L. Pickett, “High pressure/high temperature multiphase simulations of dodecane injection to nitrogen: Application on ECN Spray-A,” *Fuel*, vol. 275, p. 117871, 2020.
- [139] A. Vidal, K. Kolovos, M. R. Gold, R. J. Pearson, P. Koukouvinis, and M. Gavaises, “Preferential cavitation and friction-induced heating of multi-component Diesel fuel surrogates up to 450MPa,” *International Journal of Heat and Mass Transfer*, vol. 166, p. 120744, 2021.
- [140] N. Kyriazis, P. Koukouvinis, I. Karathanassis, and M. Gavaises, “A Tabulated Data Technique For Cryogenic Two-Phase Flows,” in *6th European Conference on Computational Mechanics (ECCM 6)*, *7th European Conference on Computational Fluid Dynamics (ECFD 7)*, (Glasgow, UK), 2018.
- [141] D. Fuster, G. Hauke, and C. Dopazo, “Influence of the accommodation coefficient on nonlinear bubble oscillations,” *The Journal of the Acoustical Society of America*, vol. 128, no. 1, pp. 5–10, 2010.
- [142] R. Schmidt and W. Wagner, “A new form of the equation of state for pure substances and its application to oxygen,” *Fluid Phase Equilibria*, vol. 19, no. 3, pp. 175–200, 1985.

- [143] R. B. Stewart, R. T. Jacobsen, and W. Wagner, “Thermodynamic Properties of Oxygen from the Triple Point to 300 K with Pressures to 80 MPa,” *Journal of Physical and Chemical Reference Data*, vol. 20, no. 5, pp. 917–1021, 1991.
- [144] E. W. Lemmon and R. T. Jacobsen, “Viscosity and Thermal Conductivity Equations for Nitrogen, Oxygen, Argon, and Air,” *International Journal of Thermophysics*, vol. 25, no. 1, pp. 21–69, 2004.
- [145] M. Dumbser, U. Iben, and C.-D. Munz, “Efficient implementation of high order unstructured WENO schemes for cavitating flows,” *Computers & Fluids*, vol. 86, pp. 141–168, 2013.
- [146] M. L. Shur, P. R. Spalart, M. K. Strelets, and A. K. Travin, “A hybrid RANS-LES approach with delayed-DES and wall-modelled LES capabilities,” *International Journal of Heat and Fluid Flow*, vol. 29, no. 6, pp. 1638–1649, 2008.
- [147] F. R. Menter and M. Kuntz, “Adaptation of Eddy-Viscosity Turbulence Models to Unsteady Separated Flow Behind Vehicles,” in *The Aerodynamics of Heavy Vehicles: Trucks, Buses, and Trains* (F. Pfeiffer, P. Wriggers, R. McCallen, F. Browand, and J. Ross, eds.), vol. 19, pp. 339–352, Berlin, Heidelberg: Springer Berlin Heidelberg, 2004. Series Title: Lecture Notes in Applied and Computational Mechanics.
- [148] S. J. Sherwin and H. M. Blackburn, “Three-dimensional instabilities and transition of steady and pulsatile axisymmetric stenotic flows,” *J. Fluid Mech.*, vol. 533, 2005.
- [149] P. Brossel, S. Eury, P. Signol, H. Laporte-Weywada, and J. Micewicz, “Development status of the Vulcain engine,” in *31st Joint Propulsion Conference and Exhibit*, (San Diego, CA, U.S.A.), American Institute of Aeronautics and Astronautics, 1995.
- [150] A. Arnone, P. Boncinelli, A. Munari, and E. Spano, “Application of CFD techniques to the design of the Ariane 5 turbopump,” in *14th Computational Fluid Dynamics Conference*, (Norfolk, VA, U.S.A.), American Institute of Aeronautics and Astronautics, 1999.
- [151] N. Kyriazis, P. Koukouvinis, and M. Gavaises, “Modelling cavitation during drop impact on solid surfaces,” *Advances in Colloid and Interface Science*, vol. 260, pp. 46–64, 2018.

- [152] M. Alamgir and J. H. Lienhard, “Correlation of Pressure Undershoot During Hot-Water Depressurization,” *Journal of Heat Transfer*, vol. 103, no. 1, pp. 52–55, 1981.
- [153] V. Blinkov, O. Jones, and B. Nigmatulin, “Nucleation and flashing in nozzles—2. Comparison with experiments using a five-equation model for vapor void development,” *International Journal of Multiphase Flow*, vol. 19, no. 6, pp. 965–986, 1993.
- [154] A. Hamzehloo and P. G. Aleiferis, “LES and RANS modelling of under-expanded jets with application to gaseous fuel direct injection for advanced propulsion systems,” *International Journal of Heat and Fluid Flow*, vol. 76, pp. 309–334, 2019.
- [155] T. C. Adamson and J. A. Nicholls, “On the Structure of Jets from Highly Underexpanded Nozzles Into Still Air,” *Journal of the Aerospace Sciences*, vol. 26, no. 1, pp. 16–24, 1959.
- [156] S. Crist, D. R. Glass, and P. M. Sherman, “Study of the highly underexpanded sonic jet.,” *AIAA Journal*, vol. 4, no. 1, pp. 68–71, 1966.
- [157] V. Vuorinen, J. Yu, S. Tirunagari, O. Kaario, and M. Larmi, “Large-eddy simulation of highly underexpanded transient gas jets,” *Physics of Fluids*, vol. 25, p. 23, 2013.
- [158] E. Franquet, V. Perrier, S. Gibout, and P. Bruel, “Free underexpanded jets in a quiescent medium\_ A review,” *Progress in Aerospace Sciences*, p. 29, 2015.
- [159] D. Edgington-Mitchell, D. R. Honnery, and J. Soria, “The underexpanded jet Mach disk and its associated shear layer,” *Physics of Fluids*, vol. 26, no. 9, p. 096101, 2014.
- [160] T. Lyras, I. Karathanassis, N. Kyriazis, P. Koukouvinis, and M. Gavaises, “Modelling of liquid oxygen nozzle flows under subcritical and supercritical pressure conditions,” *International Journal of Heat and Mass Transfer*, vol. 177, p. 121559, 2021.
- [161] D. Bradley and K. Van Hooser, “Space Shuttle Main Engine - The Relentless Pursuit of Improvement,” in *AIAA SPACE 2011 Conference & Exposition*, (Long Beach, California), American Institute of Aeronautics and Astronautics, Sept. 2011.

- [162] D. Davis and J. McArthur, "NASA Ares I Crew Launch Vehicle Upper Stage Overview," in *44th AIAA/ASME/SAE/ASEE Joint Propulsion Conference & Exhibit*, (Hartford, CT), American Institute of Aeronautics and Astronautics, July 2008.
- [163] L. Dreyer, "Latest developments on SpaceX's Falcon 1 and Falcon 9 launch vehicles and Dragon spacecraft," in *2009 IEEE Aerospace conference*, (Big Sky, MT, USA), pp. 1–15, IEEE, Mar. 2009.
- [164] "Blue Origin LLC" official web-page. <https://www.blueorigin.com/engines/be-4> [Accessed: Dec. 2023].
- [165] G. P. Sutton, "History of Liquid Propellant Rocket Engines in the United States," *Journal of Propulsion and Power*, vol. 19, pp. 978–1007, Nov. 2003.
- [166] G. P. Sutton, "History of Liquid-Propellant Rocket Engines in Russia, Formerly the Soviet Union," *Journal of Propulsion and Power*, vol. 19, pp. 1008–1037, Nov. 2003.
- [167] F. A. Boorady and D. A. Douglass, "Solution of the high-vacuum hard-start problem of the IRFNA-UDMH rocket for Gemini Agena.," *Journal of Spacecraft and Rockets*, vol. 5, pp. 22–30, Jan. 1968.
- [168] B. Chehroudi, "Recent Experimental Efforts on High-Pressure Supercritical Injection for Liquid Rockets and Their Implications," *International Journal of Aerospace Engineering*, vol. 2012, pp. 1–31, 2012.
- [169] C. Wang, Y. Song, and P. Jiang, "Modelling of liquid nitrogen spray cooling in an electronic equipment cabin under low pressure," *Applied Thermal Engineering*, vol. 136, pp. 319–326, 2018.
- [170] X. Zhu, X. Pan, Y. Mei, J. Ma, H. Tang, Y. Zhu, L. X. Liu, J. Jiang, and T. Chen, "Thermal nonequilibrium and mechanical forces induced breakup and droplet formation of superheated liquid jets under depressurized release," *Applied thermal engineering*, vol. 221, p. 119826, 2023.
- [171] M. S. Khan, I. Karimi, and D. A. Wood, "Retrospective and future perspective of natural gas liquefaction and optimization technologies contributing to efficient lng supply: A review," *Journal of Natural Gas Science and Engineering*, vol. 45, pp. 165–188, 2017.

- [172] L. Wang, X. Ma, H. Kong, R. Jin, and H. Zheng, “Investigation of a low-pressure flash evaporation desalination system powered by ocean thermal energy,” *Applied Thermal Engineering*, vol. 212, p. 118523, 2022.
- [173] P. Srivastava and A. Kumar, “Characterization of performance of multihole nozzle in cryospray,” *Cryobiology*, vol. 96, pp. 197–206, 2020.
- [174] M. Foerster, T. Gengenbach, M. W. Woo, and C. Selomulya, “The impact of atomization on the surface composition of spray-dried milk droplets,” *Colloids and Surfaces B: Biointerfaces*, vol. 140, pp. 460–471, 2016.
- [175] Y. Liao and D. Lucas, “Computational modelling of flash boiling flows: A literature survey,” *International Journal of Heat and Mass Transfer*, vol. 111, pp. 246–265, Aug. 2017.
- [176] J. Chen, X. Gao, S. Bao, L. Hu, and J. Xie, “Numerical analysis of spray characteristics with liquid nitrogen,” *Cryogenics*, vol. 109, p. 103113, July 2020.
- [177] D. Loureiro, J. Reutzsch, A. Kronenburg, B. Weigand, and K. Vogiatzaki, “Primary breakup regimes for cryogenic flash atomization,” *International Journal of Multiphase Flow*, vol. 132, p. 103405, 2020.
- [178] D. Loureiro, A. Kronenburg, J. Reutzsch, B. Weigand, and K. Vogiatzaki, “Droplet size distributions in cryogenic flash atomization,” *International Journal of Multiphase Flow*, vol. 142, p. 103705, 2021.
- [179] T. Lyras, I. Karathanassis, N. Kyriazis, P. Koukouvinis, and M. Gavaises, “Modelling of liquid oxygen and nitrogen injection under flashing conditions,” *Applied Thermal Engineering*, vol. 237, p. 121773, 2024.
- [180] K. Saha, S. Som, M. Battistoni, Y. Li, E. Pomraning, and P. K. Senecal, “Numerical investigation of two-phase flow evolution of in-and near-nozzle regions of a gasoline direct injection engine during needle transients,” *SAE International Journal of Engines*, vol. 9, no. 2, pp. 1230–1240, 2016.
- [181] Z. Lee, T. Kim, S. Park, and S. Park, “Review on spray, combustion, and emission characteristics of recent developed direct-injection spark ignition (disi) engine system with multi-hole type injector,” *Fuel*, vol. 259, p. 116209, 2020.
- [182] X. Li, S. Wang, S. Yang, S. Qiu, Z. Sun, D. L. Hung, and M. Xu, “A review on the recent advances of flash boiling atomization and combustion applications,” *Progress in Energy and Combustion Science*, vol. 100, p. 101119, 2024.

- [183] M. Chang, Z. Lee, S. Park, and S. Park, “Characteristics of flash boiling and its effects on spray behavior in gasoline direct injection injectors: A review,” *Fuel*, vol. 271, p. 117600, 2020.
- [184] H. Guo, H. Ding, Y. Li, X. Ma, Z. Wang, H. Xu, and J. Wang, “Comparison of spray collapses at elevated ambient pressure and flash boiling conditions using multi-hole gasoline direct injector,” *Fuel*, vol. 199, pp. 125–134, 2017.
- [185] R. Payri, F. J. Salvador, P. Martí-Aldaraví, and D. Vaquerizo, “Ecn spray g external spray visualization and spray collapse description through penetration and morphology analysis,” *Applied Thermal Engineering*, vol. 112, pp. 304–316, 2017.
- [186] P. Sphicas, L. M. Pickett, S. A. Skeen, and J. H. Frank, “Inter-plume aerodynamics for gasoline spray collapse,” *International Journal of Engine Research*, vol. 19, no. 10, pp. 1048–1067, 2018.
- [187] G. Zhang, M. Xu, Y. Zhang, and W. Zeng, “Quantitative measurements of liquid and vapor distributions in flash boiling fuel sprays using planar laser induced exciplex technique,” tech. rep., SAE Technical Paper, 2011.
- [188] G. Zhang, M. Xu, Y. Zhang, M. Zhang, and D. J. Cleary, “Macroscopic characterization of flash-boiling multi-hole sprays using planar laser induced exciplex fluorescence technique. part i. on-axis spray structure,” *Atomization and Sprays*, vol. 22, no. 10, 2012.
- [189] C. K. Mohapatra, D. P. Schmidt, B. A. Sforzo, K. E. Matusik, Z. Yue, C. F. Powell, S. Som, B. Mohan, H. G. Im, J. Badra, *et al.*, “Collaborative investigation of the internal flow and near-nozzle flow of an eight-hole gasoline injector (engine combustion network spray g),” *International Journal of Engine Research*, vol. 24, no. 6, pp. 2297–2314, 2023.
- [190] M. Moulai, R. Grover, S. Parrish, and D. Schmidt, “Internal and near-nozzle flow in a multi-hole gasoline injector under flashing and non-flashing conditions,” tech. rep., SAE Technical Paper, 2015.
- [191] K. Saha, S. Som, M. Battistoni, Y. Li, S. Quan, and P. Kelly Senecal, “Modeling of internal and near-nozzle flow for a gasoline direct injection fuel injector,” *Journal of Energy Resources Technology*, vol. 138, no. 5, p. 052208, 2016.

- [192] E. T. Baldwin, R. O. Grover Jr, S. E. Parrish, D. J. Duke, K. E. Matusik, C. F. Powell, A. L. Kastengren, and D. P. Schmidt, “String flash-boiling in gasoline direct injection simulations with transient needle motion,” *International Journal of Multiphase Flow*, vol. 87, pp. 90–101, 2016.
- [193] J. W. Gärtner, Y. Feng, A. Kronenburg, and O. T. Stein, “Numerical investigation of spray collapse in gdi with openfoam,” *Fluids*, vol. 6, no. 3, p. 104, 2021.
- [194] B. Mohan, J. Badra, J. Sim, and H. G. Im, “Coupled in-nozzle flow and spray simulation of engine combustion network spray-g injector,” *International Journal of Engine Research*, vol. 22, no. 9, pp. 2982–2996, 2021.
- [195] F. Duronio, S. Ranieri, A. Montanaro, L. Allocca, and A. De Vita, “Ecn spray g injector: Numerical modelling of flash-boiling breakup and spray collapse,” *International Journal of Multiphase Flow*, vol. 145, p. 103817, 2021.
- [196] F. Nicoud and F. Ducros, “Subgrid-scale stress modelling based on the square of the velocity gradient tensor,” *Flow, turbulence and Combustion*, vol. 62, no. 3, pp. 183–200, 1999.
- [197] D. J. Duke, A. L. Kastengren, K. E. Matusik, A. B. Swantek, C. F. Powell, R. Payri, D. Vaquerizo, L. Itani, G. Bruneaux, R. O. Grover Jr, *et al.*, “Internal and near nozzle measurements of engine combustion network “spray g” gasoline direct injectors,” *Experimental Thermal and Fluid Science*, vol. 88, pp. 608–621, 2017.